March 2016

Theoretical Studies of Atomic Transport in Ternary Semiconductor Quantum Dots and Charge Transport in Organic Photovoltaic Active Layers

Xu Han
University of Massachusetts Amherst

Theoretical Studies of Atomic Transport in Ternary Semiconductor Quantum Dots and Charge Transport in Organic Photovoltaic Active Layers

A Dissertation Presented

by

XU HAN

Submitted to the Graduate School of the
University of Massachusetts Amherst in partial fulfillment
of the requirements for the degree of

DOCTOR OF PHILOSOPHY

February 2016

Department of Chemical Engineering

Theoretic Studies of Atomic Transport in Ternary Semiconductor Quantum Dots and Charge Transport in Organic Photovoltaic Active Layers

A Dissertation Presented

by

XU HAN

Approved as to style and content by:

_____
Dimitrios Maroudas, Chair

_____
Triantafillos J. Mountziaris, Member

_____
Ashwin Ramasubramaniam, Member

_____
Dhandapani Venkataraman, Member

_____
John Collura, Interim Department Head
Department of Chemical Engineering

DEDICATION

To my Mother, Father, and Sister

ACKNOWLEDGMENTS

I would like to thank my advisor Prof. Dimitrios Maroudas for his guidance throughout my graduate research. I could not resolve all the challenging problems without his patience, encouragement, and insightful advice.

I would also like to thank my committee members Prof. Mountziaris, Prof. Ramasubramaniam, and Prof. Venkataraman. Their suggestions during my proposal defense were very useful for the improvement of my final thesis.

I also thank all my friends in Amherst. They are always there to share my happiness and difficulties.

Finally, I would like to thank my family. My mother, father, and sister are always there to support me.

ABSTRACT

THEORETICAL STUDIES OF ATOMIC TRANSPORT IN

TERNARY SEMICONDUCTOR QUANTUM DOTS AND

CHARGE TRANSPORT IN ORGANIC PHOTOVOLTAIC ACTIVE LAYERS

FEBRUARY 2016

XU HAN, B.S., DALIAN UNIVERSITY OF TECHNOLOGY

Ph.D., UNIVERSITY OF MASSACHUSETTS AMHERST

Directed by: Professor Dimitrios Maroudas

Ternary semiconductor quantum dots with thermodynamically stable structures are particularly important for achieving optimal performance in optoelectronic and photovoltaic applications. Ternary quantum dots (TQDs) are typically synthesized in the form of core/shell structures. However, misfit strain induced by the abrupt core/shell interface can change the nature of the TQDs dramatically, leading to unstable optoelectronic function. In this thesis, a transient species transport model is developed to predict species distributions in TQDs during their thermal annealing. Specifically, the interdiffusion kinetics is analyzed of group-VI species in $ZnSe_{1-x}S_x$ and $ZnSe_{1-x}Te_x$ TQDs and of group-III species in $In_xGa_{1-x}As$ TQDs. The modeling results are used to interpret the evolution of near-surface species concentration during thermal annealing and predict the equilibrium species distribution as a function of TQD size and composition. A database of constituent species transport properties is generated for further design of post-growth processes that enables the development of thermodynamically stable TQD structures with optimal optoelectronic function grown through simple one-step colloidal synthesis techniques.

Nanoparticle assemblies of organic semiconducting materials are particularly appealing for next-generation organic photovoltaic (OPV) devices because their low-cost aqueous synthesis reduces the usage of chlorinated solvents. Another class of novel semiconducting materials, organometallic halide perovskites, have emerged as promising materials for solar cells because of their high photo-absorption coefficient and high power conversion efficiency (PCE). Based on deterministic charge carrier transport models, this thesis presents a computational analysis of charge transport in photovoltaic devices with active layers of the above two types of materials and develops design protocols for improving photovoltaic device efficiency.

Our results demonstrate that charge transport efficiencies in centrifuged organic nanoparticle assemblies are comparable with those in drop cast thin films. The effects on charge transport of excess stabilizing surfactant molecules and dispersion of insulating nanoparticles in the assemblies have been analyzed. The simulation results accurately reproduce experimental data and provide interpretations for the observed effects of the active layer nanostructure, i.e., nanoparticle size, ratio, and internal morphology, on charge transport and device PCE. Furthermore, the charge generation rate in the active layer is maximized and the device's photovoltaic performance is optimized with respect to the OPV device parameters. For photovoltaic devices based on organometallic halide perovskites, the modeling results demonstrate quantitatively that incorporation of multi-walled carbon nanotubes (MWCNTs) into the perovksite layer reduces bimolecular recombination, thus increasing the device's PCE. In addition, we find that electronic band offsets play an important role in determining the effects on device performance of the charge carrier mobilities and of majority doping in the electron and hole transporting

layers (ETLs and HTLs). The modeling results provide guidelines for designing hybrid perovskite photovoltaic devices with enhanced photovoltaic performance.

TABLE OF CONTENTS

Page

LIST OF TABLES

Table Page

LIST OF FIGURES

Figure Page

CHAPTER 1

INTRODUCTION

1.1 Background and Motivation

Quantum dots (QDs) of inorganic semiconductors are widely utilized in current research in light emitting diodes (LEDs), solar cells, lasers, and biomedical applications [1-5]. Their size and composition have a strong influence on their electronic band structure and their band gap. Thus, they can be used as nanomaterials with tunable electronic and optical properties. However, the surface trap state of QDs is a major source of efficiency loss. In order to passivate the trap states and enhance the QDs' photoluminescence (PL) quantum yield, another layer of semiconductor material is used as a coating layer (as a shell coating the QD core in a core/shell structure) to form type-I core/shell QDs, where the shell material has a wider band gap than that of the core. In reverse type-I or type-II core/shell QDs, the shell material has a narrower or staggered band gap, respectively, compared to that of the core. In these two types of QDs, the shell thickness is a key parameter for tuning optoelectronic properties [6,7].

In experiments, a two-step overcoating method for core/shell QD synthesis causes lattice mismatch between the core and shell materials. The resulting misfit strain leads to defects at the core/shell interface, PL blinking, and band offset realignments. This lattice mismatch strain can result in energy level transition to change core/shell QDs from type-I to type-II [8]. To relieve this strain, radially graded alloys with softer confinement potential were synthesized for continuous nonblinking PL emission [9]. In multicomponent QDs, the nature of the interaction between constituent atomic species

and the QD surface may attract/repel these constituent atoms to/from the surface. Depending on the strength of the interaction, an atomic species concentration boundary layer may form near the QD surface, resulting in formation of so-called core/shell-like QDs. Such core/shell-like structures ensure the thermodynamic stability and reliability of the QD devices under high operating temperature. Earlier studies focused on the tendency of species surface segregation in ternary QDs of the semiconductor compounds $ZnSe_{1-x}Te_x$, $In_{1-x}Ga_xAs$, and $ZnSe_{1-x}S_x$ [10-13]. It was found that precise band gap engineering is possible in QDs with thermodynamically stable compositional distributions. In experiments, this stable compositional distribution can be achieved through a thermal annealing process after initial core/shell QD synthesis. To this end, in this thesis, by applying species surface segregation theory, we develop a model for simulating atomic interdiffusion kinetics during the thermal annealing process of ternary QDs with an initial core/shell structure to obtain QDs with thermodynamically stable distributions of their constituent species. We then employ our model to optimize the design of core/shell-like ternary QDs by controlling their composition, nanoparticle size, and the annealing temperature.

In addition to inorganic semiconductor nanostructures, organic polymer semiconductors have drawn significant research interest in the fabrication of organic LEDs and organic photovoltaic devices. These polymer semiconductors have many advantages as organic photovoltaic (OPV) active layers when compared to conventional inorganic photovoltaic materials. First, organic polymers are of lower cost and the active-layer synthesis processes require much lower energy input as compared to the high-temperature and vacuum requirements for the fabrication of silicon wafers,

amorphous silicon films, CdTe layers, and Copper Indium Gallium Selenide (CIGS) thin films. Second, because of the flexibility of the polymers, they can be deposited on flexible substrates such as plastics and metal foils. This feature enables large-scale industrial fabrication using roll-to-roll printing technology [14,15], as shown in Fig. 1.1. Finally, the exclusion of heavy metals and toxic elements, such as Ga, As, and Cd, makes the use of organic polymers in OPV manufacturing environmentally friendly. Extensive research on OPV devices has recently enabled the fabrication of devices with power conversion efficiency (PCE) over 10% [16]. However, a lot of progress is required in the engineering of OPV devices until they reach PCEs of 20-30% that are typical of inorganic photovoltaic devices.

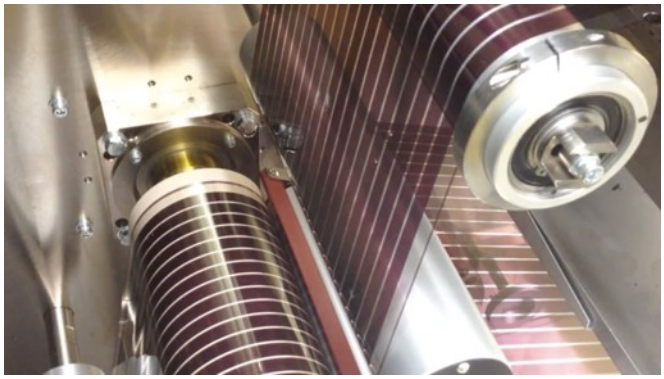

Figure 1.1. Manufacturing of organic solar cells using roll-to-roll printing technology.

A typical OPV device architecture is shown in Fig. 1.2. The organic active layer is sandwiched between two electrodes. Charge pairs (electron-hole pairs) known as excitons are generated in this layer. They are later separated, transported to the corresponding electrodes, and extracted to convert solar energy to electric energy. As for the organic active layer morphology, pristine films are commonly synthesized for maximizing the mobility of the free charge carriers (electrons and holes). However,

using conjugated nanoparticle assemblies has the advantages of flexibility in tuning nanoparticle size, internal structure, and ordering [17,18]. Large-area active layer manufacturing is possible through ink-jet printing or spray coating of stable nanoparticle dispersions. Nevertheless, the synthesis of nanoparticle assemblies requires the use of surfactants as nanoparticle dispersion stabilizers. These surfactant molecules are expected to impede charge transport. To ensure OPV device performance, it is important to achieve charge transport efficiency of conjugated nanoparticle assemblies comparable to that of pristine films. To this end, this thesis focuses on a fundamental understanding of active layer nanostructure effects on charge transport and OPV device efficiency by modeling charge transport and charge carrier kinetics in photovoltaic active layers.

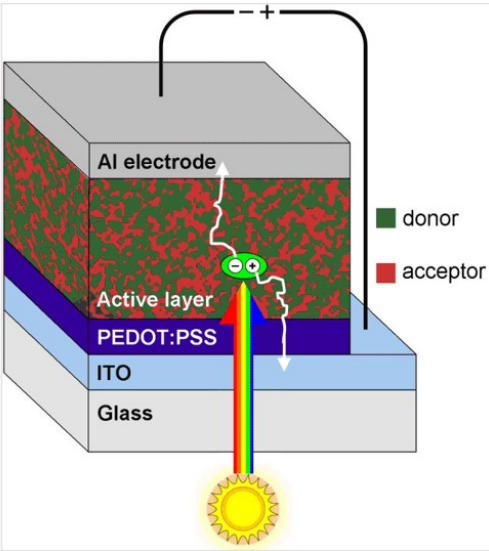

Figure 1.2. Typical OPV device architecture.

One of the problems associated with OPV materials is their poor mechanical properties. This can be improved by synthesizing a binary blend of an organic conjugated polymer with a rigid insulating polymer [19]. These insulating polymers are required to have optical transparency as well as stable chemical and thermal properties.

Among various insulating polymers, polymethylmethacrylate (PMMA) and polystyrene (PS) meet the above requirements. To understand the photovoltaic performance of such blends, we analyze the effects of insulating nanoparticle size and conducting-to-insulating nanoparticle ratio on charge transport in binary assemblies of conducting and insulating nanoparticles.

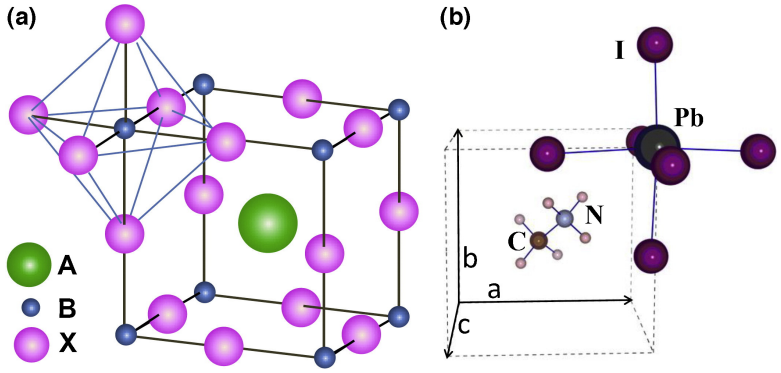

Figure 1.3. (a) Hybrid perovskite structure with the general chemical formula of ABX_3. (b) Unit cell of cubic $CH_3NH_3PbI_3$ hybrid perovskites.

Organometallic halide perovskite has emerged as a new type of photovoltaic material and has potential to be developed for commercial applications. The structure of such hybrid perovskites is shown in Fig. 1.3 [20]. The organometallic halide perovskite has the structure of ABX_3, where A refers to an organic cation, B refers to a divalent metal cation, and X represents halogen anions. On the cubo-octahedral site, $CH_3NH_3^+$ is the most common organic cation. Pb^{2+} and Sn^{2+} are generally used as the metal cation, occupying the octahedral site. X can be Cl^-, Br^-, or I^- only or a mix of these atoms for tuning the electronic properties and the stability of the hybrid perovskite.

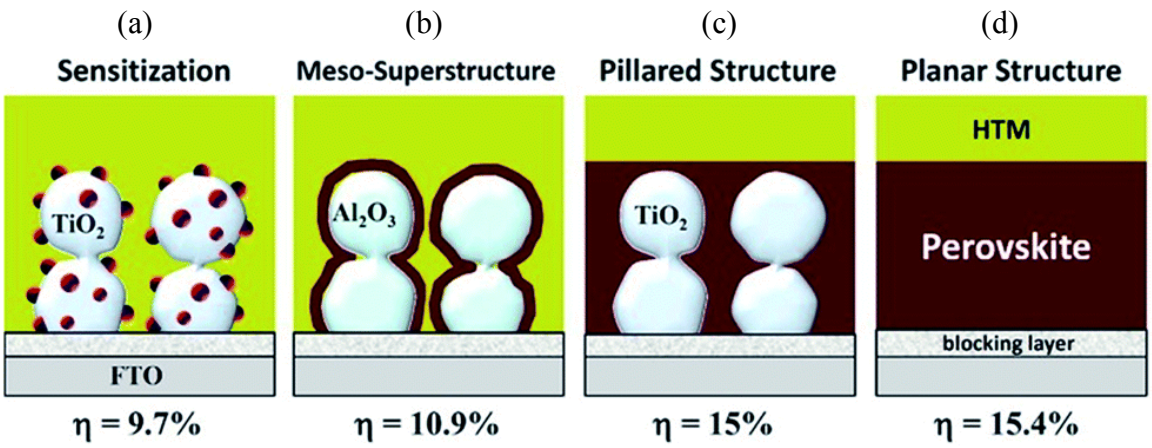

Figure 1.4. Development of hybrid perovskite structures with solid hole transport medium.

For the past 5 years, the power conversion efficiency of hybrid perovskite solar cells has increased from an initial 3.8% to around 19.3% [21,22]. At first, hybrid perovskite is incorporated as the sensitizer in the liquid electrolyte-based sensitized solar cells. Due to the solvation of perovskite in polar solvent in these systems, the perovskite sensitized solar cells degrade within tens of minutes under continuous light exposure [23]. In order to address the instability concerns, a solid hole transport medium is implemented to substitute the liquid electrolyte. A subsequent development of hybrid perovskite-based solar cell structure is shown in Fig. 1.4 [24]. In Fig. 1.4(a), hybrid perovskite quantum dots are attached to the surface of a TiO_2 mesoporous scaffold. A hole transport medium based on small molecules is infiltrated inside the TiO_2 porous to form heterojunctions. In this structure, hybrid perovskites are designed as the absorber. Electrons and holes are transported to the respective electrodes through the TiO_2 and the hole transport medium. In a similar structure in Fig. 1.4(b), Al_2O_3 replaces TiO_2 as the scaffold and hybrid perovskite is coated onto the Al_2O_3 surface. Due to the higher conduction band energy level of Al_2O_3, electron injection from the perovskite to Al_2O_3 is

impossible, thus electron transport is not expected in this system. However, a higher efficiency is obtained, which indicates the good electron transport properties of hybrid perovskite and a higher electron mobility in hybrid perovskite than in TiO_2. The subsequent studies demonstrate the ambipolar charge transport properties of hybrid perovskites. A pillared structure improves the device efficiency up to 15% as shown in Fig. 1.4(c). Furthermore, a planar structure that excludes electron transport in the oxide is designed as shown in Fig. 1.4(d), with a high device efficiency of over 15%. Because of the hole transport in the perovskite material, a hole-transport-medium-free structure has also been applied and is able to achieve an efficiency around 11%. According to recent progress, an efficiency of over 20% is predicted to be achievable [25]. It has been estimated that the efficiency of hybrid perovskite solar cells will approach those of solar cells based on GaAs. This is attributed to a much better optical absorption and a higher intrinsic carrier density in hybrid perovskite materials than in GaAs thin films [26].

1.2 Thesis Objectives and Outline

The goal of this thesis is to contribute to the improved performance of optoelectronic and photovoltaic devices by understanding and predicting atomic transport in inorganic ternary QDs and charge transport in active layers of OPV and hybrid perovskite devices. The predictions of our transport models are validated through comparisons with experimental data and are used to design materials and processes for optimal optoelectronic and photovoltaic performance. Toward this goal, the specific objectives of this thesis include:

(1) Analysis of atomic species interdiffusion kinetics in ternary semiconductor QDs during thermal annealing processes and design of thermodynamically stable

core/shell like QDs by tuning overall QD composition, size, and annealing temperature;

(2) Identification of the differences in charge transport efficiency in OPV active layers composed of pristine thin films and self-assembled nanoparticles;

(3) Fundamental understanding of individual nanoparticle morphology effects on charge transport kinetics and investigation of the effects of nanoparticle morphology, size, and ratio on OPV device performance;

(4) Optimization of OPV device performance through both optical and electrical modeling;

(5) Analysis of charge transport in hybrid perovskite planar heterojunction devices and identification of key parameters to boost device performance.

The remaining of the thesis achieves the above objectives as follows:

In Chapter 2, a one-dimensional transient model based on species surface segregation theory is developed and used to simulate species interdiffusion in spherical TQDs. The model is implemented to study the interdiffusion of group-VI atoms in $ZnSe_{1-x}S_x$ quantum dots. The modeling results reproduce experimental data from X-ray photoelectron spectroscopy (XPS) for Se and S near-surface concentration evolution during thermal annealing with a ZnSe/ZnS core/shell initial configuration. Transport coefficients and thermal activation barriers for interdiffusion are derived and found to be well bounded by values from the literature. In $In_xGa_{1-x}As$ and $ZnSe_{1-x}Te_x$ QDs, the model predicts the formation of core/shell-like structures with shell regions rich in the surface segregating species In and Te, respectively. Shell thickness is controllable by tuning composition *x*, QD diameter, and thermal annealing temperature. A systematic

parametric analysis generates a database of transport properties, which can be used to design post-growth thermal annealing processes that enable the development of thermodynamically stable QDs with optimal electronic properties grown through simple one-step colloidal synthesis techniques. The work in this chapter has been published in two journal articles, one in *Applied Physics Letters* and another one in *AIChE Journal*.

In Chapter 3, a single-type charge carrier transport model is developed to analyze hole transport in layers of the organic polymer poly(3-hexylthiophene) (P3HT) of different nanostructures. The model is used to characterize various P3HT layers examined in terms of their hole transport dispersivity. The model reproduces experimental data of photocurrent evolution in P3HT samples ranging from drop cast thin films to surfactant-stabilized nanoparticle assemblies, explains the role of excess surfactant molecules in hole trapping for assemblies of P3HT nanoparticles, and demonstrates quantitatively the potential of using nanoparticle assemblies in organic photovoltaic devices. This work has been published in *Chemical Physics Letters*. The model also is applied to analyze the effects of insulating nanoparticles in binary nanoparticle assemblies of P3HT/PMMA and P3HT/PS. The trapping energy levels are found to be deeper when the insulating nanoparticle concentration increases. Furthermore, a comprehensive model is developed for the simulation of both electron and hole transport in OPV devices with active layers consisting of P3HT:phenyl-C61-butyric acid methyl ester (PCBM) spherical nanoparticle assemblies. The models reproduce both transient photocurrents from time-of-flight (TOF) experiments and steady-state photocurrent density-voltage (J-V) device characteristics from experimental measurements under steady illumination. The simulation results provide quantitative

interpretations to the effects of individual nanoparticle morphology, as well as nanoparticle size and ratio on charge transport and device power conversion efficiency. The models also predict improved device PCE by introducing proper interlayers between the active layer and the electrodes and controlling the thickness of the active layer. This work has been published in the *Journal of Physical Chemistry C*.

In Chapter 4, a comprehensive model is developed for the analysis of electron and hole transport in photovoltaic devices based on hybrid perovskite planar heterojunctions. The model is applied to characterize the effects of incorporating multi-walled carbon nanotubes (MWCNTs) into the perovskite layer. An optimum concentration of MWCNTs is found to maximize the photovoltaic device performance due to the reduction of the bulk recombination rate as well as by maintaining a balanced charge mobility and a low level of trap density. The effects of charge mobilities and majority doping in the electron and hole transporting layers of the device are investigated considering different electronic band offsets in the planar perovskite heterojunctions. A strategy for achieving improved device performance is developed based on the charge transport models.

In Chapter 5, the most important results in the thesis are summarized and the most important conclusions reached are outlined. Finally, some future directions are discussed for research on photovoltaic devices based on hybrid perovksite planar heterojunctions.

CHAPTER 2

KINETIC MODELING OF SPECIES INTERDIFFUSION IN SEMICONDUCTOR TERNARY QUANTUM DOTS

2.1 Introduction

Modulating the composition of ternary quantum dots enables the precise tuning of their optoelectronic properties in addition to the tunability provided by the QD size modulation. Such strategies have led to substantial improvements in the function of QDs in optoelectronic and photovoltaic devices, ranging from increased stability against photo-degradation and enhanced quantum yields [27] to continuous nonblinking photoluminescence emission [9]. These advances emphasize the importance of controlling the chemical composition of the QDs and the distribution of the corresponding chemical species in the QDs.

Recent first-principles calculations have demonstrated the effects of compositional distribution on the electronic structure and properties of ternary QDs, such as the compositional dependence of the band gap in $ZnSe_{1-x}S_x$ and $ZnSe_{1-x}Te_x$ nanocrystals with compositional distributions ranging from randomly alloyed configurations to configurations with sharp core/shell interfaces [28,29]. These findings highlight the importance of thermodynamic stability of alloyed and heterogeneous QDs, meaning that a certain QD growth strategy may lead to configurations with compositional distributions away from equilibrium; these configurations will evolve to their equilibrium states during processing or device service, which may impact their electronic properties significantly with respect to those of the as grown configurations. Such a thermodynamic

instability of a core/shell interface was demonstrated recently in thermal annealing experiments of colloidally synthesized ZnSe/ZnS core/shell QDs and emphasized the importance of interdiffusion of Se and S atoms that leads to alloying of the pure ZnSe core and ZnS shell [13].

Motivated by the above studies, the purpose of this chapter is to develop a continuum model of atomic species transport in ternary QDs, validate it properly, and use it as a predictive tool for designing growth and post-growth processes toward developing QDs with the properties required to guarantee their optimal function in optoelectronic and photovoltaic devices. An important phenomenon underlying species transport in QDs and other nanostructures is drift due to the tendency of certain species to segregate on the nanostructure surfaces; this is properly taken into account in the continuum transport model. The model's validation involves comparison of its predictions with experimental data and results of first-principles-based atomistic simulations; fitting the model to the data and simulation predictions constitutes the model's parameterization. The findings of the analysis contribute to our fundamental understanding of the thermodynamic stability of ternary nanocrystals and the self-assembly of core/shell-like structures in ternary QDs; this self-assembly process is equivalent to the formation of a boundary layer near the QD surface in the concentration of a surface segregating species in the QD.

In Section 2.2, the continuum transport model is developed for the distribution of species in ternary QDs accounting for surface segregation in addition to Fickian diffusion. The steady-state and equilibrium species concentration profiles in ternary QDs are calculated according to the continuum transport model. In Section 2.3, the model is first validated by comparisons of its predictions with first-principles-based predictions of

equilibrium compositional distributions in $ZnSe_{1-x}Te_x$ and $In_xGa_{1-x}As$ QDs over a range of composition *x* and QD diameter according to a hierarchical computational approach combining density functional theory (DFT) calculations and Monte Carlo (MC) simulations. The transient version of the properly parameterized continuum model is then used to compute how the compositional distribution of the group-VI species in the nanocrystal changes during the annealing of $ZnSe_{1-x}S_x$ QDs prepared in ZnSe/ZnS core/shell configurations. The model gives an excellent interpretation to experimental data [13] for the evolution of the near-surface concentration of Se and S atoms in the QDs and provides a means to determine all the relevant kinetic parameters, such as diffusion coefficients and the associated thermal activation barriers. In Section 2.4, the most important conclusions are summarized.

2.2 Model Description of Species Transport in Ternary Semiconductor Nanocrystals

The 1-D transient species transport model is based on the phenomenological theory of Ref. 12. It is employed to analyze compositional distributions in ternary nanocrystals of compound semiconductors. These materials include III–V compounds of the type $A_xB_{1-x}Y$, such as $In_xGa_{1-x}As$, and II–VI compounds of the type $ZA_{1-x}B_x$, such as $ZnSe_{1-x}S_x$ and $ZnSe_{1-x}Te_x$; in this notation, A, B, Y, and Z denote atomic species from certain groups of the periodic table. The crystalline semiconductors of interest are characterized by a zinc-blende lattice structure. The zinc-blende lattice consists of two face-centered cubic (fcc) sublattices. In the cases of interest, species Z (i.e., the group-II atomic species in the II–VI compounds under consideration) or Y (i.e., the group-V atomic species in the III–V compounds under consideration) occupy the sites of one of

the two fcc sublattices, while species A and B occupy the sites of the other sublattice; therefore, in each nanocrystal, the sites of each sublattice are occupied by atoms of the same group of the periodic table. The statement of the problem under study is to determine the compositional distribution of species A and B in their sublattice throughout the nanocrystal for given temperature T, overall composition expressed by the compositional parameter x, and nanocrystal diameter d.

According to the model, atomic species interdiffusional transport is governed by the continuity equation

$$\frac{\partial C}{\partial t} = -\nabla \cdot \boldsymbol{J} = \nabla \cdot \left[-\boldsymbol{u}_d C + D \nabla C \right], \tag{2.1}$$

where $C = C_i(r,t)$ is the species concentration field for species i = A or B, $\boldsymbol{J} = \boldsymbol{J}_i(r,t)$ is the flux of species i, t is time and r is the radial coordinate of the spherical nanocrystal with radius R ($0 \le r \le R$), ∇ is the gradient operator, D is the corresponding species diffusion coefficient, and $\boldsymbol{u}_d$ is the species drift velocity. The source for this drift in the nanocrystal is the thermodynamic driving force, $\boldsymbol{F}$, for surface segregation of species A and B and is expressed as $\boldsymbol{F} = -\nabla U$, where $U = U(r)$ is the interaction potential of the diffusing species (A and B) with the nanocrystal surface. The drift velocity $\boldsymbol{u}_d$ is given by the Nernst-Einstein equation

$$\boldsymbol{u}_d = \frac{D\boldsymbol{F}}{k_B T} = -\frac{D \nabla U}{k_B T}, \tag{2.2}$$

where k_B is the Boltzmann constant. The species-surface interaction potential can be expressed as

$$U = \pm \frac{A_s}{(R-r)^3}, \tag{2.3}$$

where A_s is a metric of the strength of the driving force for surface segregation, and the sign in the right-hand side of the expression for U may be positive or negative for repulsive or attractive interaction, respectively. The form of the interaction potential U in Eq. (2.3) is based on elasticity theory [12]. R - r is the distance of the diffusing species from the nanocrystal surface; we use $R = d/2 + r_0$, where r_0 is a characteristic length introduced because Eq. (2.3) does not attempt to capture the limit $d/2 - r = 0$ and is valid only for $R - r \geq r_0$. The introduction of r_0 prevents a singularity in the interaction potential at $r = d/2$. We take r_0 to be comparable to the interplanar distance in the nanocrystal lattice, r_0 = 0.2 nm. We make the simplifying assumptions that the diffusivities of the atomic species A and B in the nanocrystal are practically equal, i.e., we use a common diffusivity D for diffusion of atoms from the same group in the zinc-blende lattice of the ternary QD. We also take the surface-segregation strength parameters, A_s, of species A and B in Eq. (2.3) to be equal, but the interaction with the nanocrystal surface is attractive for A and repulsive for B. A symmetry condition is applied at the spherical nanocrystal center and, as there is no escape of species from the nanocrystal surface during annealing, a boundary condition of zero radial flux at the nanocrystal surface

$$\left.\frac{\partial C}{\partial r}\right|_{r=0} = 0 \quad \text{and} \quad \left. \boldsymbol{J} \cdot \hat{\mathbf{r}} \right|_{r=R} = [\boldsymbol{u}_d(R) \cdot \hat{\mathbf{r}}] C(R) - D \left.\frac{\partial C}{\partial r}\right|_{r=R} = 0, \tag{2.4}$$

where $\hat{\mathbf{r}}$ is the unit vector in the radial direction. The proper initial condition should be specified for each annealing experiment. For example, for an initial core/shell configuration

$$C_{\mathrm{A}}(r,0) = \begin{cases} C_0, & r \in [0, R_c] \\ 0, & r \in (R_c, R] \end{cases} \quad \text{and} \quad C_{\mathrm{B}}(r,0) = \begin{cases} 0, & r \in [0, R_c] \\ C_0, & r \in (R_c, R] \end{cases}, \tag{2.5}$$

which corresponds to a A/B core/shell configuration (i.e., an AY/BY or a ZA/ZB core/shell configuration of the ternary nanocrystal composition) with R_c being the radius of the core. Equations (2.1)-(2.5) formulate a well-posed boundary-value problem (BVP) for the concentration fields of A and B in the nanocrystal. The 1-D nature of the model, that is, the assumption that there is only radial dependence of C, stems from the driving force for species transport in the nanocrystal, which exists in the radial direction only; this also is evident from the initial and boundary conditions, Eqs. (2.4) and (2.5), of the BVP.

Next, we express the differential operators of Eqs. (2.1) and (2.2) in spherical coordinates and introduce the dimensionless variables $\eta \equiv r/R$ with $0 \le \eta < 1$, $\Theta \equiv C/C_0$, and $\tau \equiv Dt/R^2$ into the BVP of Eqs. (2.1)-(2.5) to derive the dimensionless form of the BVP. To express this dimensionless form, we also define the drift Peclét number, Pe, as

$$Pe \equiv \frac{u_{d,\max} R}{D}, \tag{2.6}$$

where $u_{d,\max}$ is the velocity scale taken to be equal to the maximum drift velocity; Pe has its usual meaning [30] with drift being used instead of convection. From Eqs. (2.2) and (2.3), the drift velocity can be expressed as $\boldsymbol{u}_d = u_{d,r}\hat{\mathrm{r}}$ with

$$u_{d,r} = \frac{3A_s D}{k_B T (R-r)^4} = \frac{3A_s D}{k_B T R^4} \frac{1}{(1-\eta)^4}. \tag{2.7}$$

The drift velocity of Eq. (2.7) is a monotonically increasing function of η, reaching its maximum value, $u_{d,\max}$, at the nanocrystal surface, $\eta = \kappa = (d/2)/R$. Equation (2.7) can then be rewritten as

$$u_{d,r} = u_{d,\max} \frac{(1-\kappa)^4}{(1-\eta)^4} \text{ with } u_{d,\max} = \frac{3A_s D}{k_B T R^4} \frac{1}{(1-\kappa)^4}. \tag{2.8}$$

Combining Eqs. (2.6) and (2.8) gives

$$Pe = \frac{3A_s}{k_B T R^3} \frac{1}{(1-\kappa)^4}. \tag{2.9}$$

Introducing the above dimensionless variables and parameter into Eqs. (2.1)-(2.3) gives the dimensionless governing equation for the concentration field, $\Theta = \Theta_A(\eta,\tau)$ or $\Theta = \Theta_B(\eta,\tau)$

$$\frac{\partial \Theta}{\partial \tau} = \frac{\partial^2 \Theta}{\partial \eta^2} + \frac{2}{\eta}\frac{\partial \Theta}{\partial \eta} - Pe\frac{(1-\kappa)^4}{(1-\eta)^4}\frac{\partial \Theta}{\partial \eta} - 2Pe\frac{(1-\kappa)^4(1+\eta)}{\eta(1-\eta)^5}\Theta. \tag{2.10}$$

Similarly, Eq. (2.4) gives the dimensionless boundary conditions

$$\left.\frac{\partial \Theta}{\partial \eta}\right|_{\eta=0} = 0 \quad \text{and} \quad \left.\frac{\partial \Theta}{\partial \eta}\right|_{\eta=\kappa} - Pe\Theta(\kappa,\tau) = 0 \tag{2.11}$$

and Eq. (2.5) yields the dimensionless initial condition

$$\Theta_A(\eta,0) = \begin{cases} 1, & \eta \in [0,\kappa_1] \\ 0, & \eta \in (\kappa_1,\kappa] \end{cases} \quad \text{and} \quad \Theta_B(\eta,0) = \begin{cases} 0, & \eta \in [0,\kappa_1] \\ 1, & \eta \in (\kappa_1,\kappa] \end{cases}. \tag{2.12}$$

In Eqs. (2.11) and (2.12), the surface location is at $\eta = \kappa$ and the location of the initial core/shell interface is at $\eta = \kappa_1 \equiv R_c/R$.

In the subsequent section, the transient model described in Eqs. (2.10)-(2.12) is validated by comparison with results of first-principles-based atomistic simulations of equilibrium compositional distributions and experimental measurements of near-surface species concentrations.

2.3 Results and Discussion

2.3.1 Self-Assembly of Core/Shell-like Structures in Ternary Quantum Dots

The steady-state form of the BVP of Eqs. (2.1)-(2.4) is solved analytically. We employ perturbation theory, which gives a good characterization of the solution structure in limiting values of *Pe*; these details are not given here, because it is easy to obtain an exact closed-form solution to the problem. According to Eq. (2.1), the governing equation at steady state is $\nabla \cdot \boldsymbol{J} = 0$. Satisfying the no-flux boundary condition of Eq. (2.4) implies that the steady-state solution is equivalent to the equilibrium solution, that is, the solution to the equation $\boldsymbol{J} = \boldsymbol{0}$. Using the flux expression of Eqs. (2.1)-(2.3) gives the equilibrium solution

$$C_i(r) = B_i \exp\left[-\frac{U(r)}{k_B T}\right], \tag{2.13}$$

where the constant B_i is determined by satisfying the overall mass balance $N_i = \int_0^R C_i(r) 4\pi r^2 dr$ for the atomic species *i* in the nanocrystal. Equation (2.13) is the well-known Maxwellian atmosphere of "impurities" forming around larger-scale defects, such as dislocations in the crystalline lattice [31]; here, the "impurities" are the diffusing species and the large-scale defect is the surface. Following the dimensionless notation of Eqs. (2.10)-(2.12), Eq. (2.13) can be rewritten as

$$\Theta_i(\eta) \propto \exp\left[\frac{Pe(1-\kappa)^4}{3(1-\eta)^3}\right] = \exp\left[\frac{A_s}{k_B T(R-r)^3}\right] \tag{2.14}$$

for a species that is attracted by and segregates on the nanocrystal surface. It should be noted that the results of the perturbation analysis also give the solution of Eq. (2.14). For $Pe \ll 1$, the regular-perturbation solution in the form of a power-series expansion in powers of Pe is equal to the Taylor-series expansion of the Maxwellian atmosphere of Eq. (2.14). For $Pe \gg 1$, the singular-perturbation solution in the form of two matched asymptotic expansions also matches exactly the Maxwellian atmosphere of Eq. (2.14).

The equilibrium solution of Eq. (2.14) is plotted in Fig. 2.1 for a ternary QD of d = 3.8 nm. In the absence of surface segregation, $A_s = 0$ and Eq. (2.9) gives $Pe = 0$, which results in a uniform species distribution throughout the nanocrystal. When the species tendency for surface segregation is weak, Eq. (2.9) gives $Pe \ll 1$ for a low segregation strength A_s, resulting in a species distribution that is just a perturbation from the uniform distribution characterized by an increased species concentration in the near-surface region of the nanocrystal. For a strong tendency for species segregation on the nanocrystal surface, however, the higher segregation strength A_s gives $Pe \gg 1$ and causes the

formation of a concentration boundary layer near the nanocrystal surface. This boundary layer formation has important implications for the design and synthesis of ternary QDs for optoelectronics and photovoltaics. It means that surface segregation drives the assembly of core/shell-like nanocrystals, that is, equilibrium configurations with a core region that is deficient in the segregating species and a shell region near the surface that is rich in the segregating species. Therefore, for ternary QDs with strongly segregating species, *Pe* can be tailored to determine the shell thickness of the core/shell-like QD. The core and shell regions are separated by a graded "interface" expressed by the smooth and continuous concentration increase near the edge of the boundary layer.

For $Pe >> 1$, scaling analysis within the boundary layer [30] gives for the boundary-layer thickness δ

$$\frac{\delta}{R} \sim Pe^{-1} \text{ or } \delta \sim \frac{R}{Pe}. \tag{2.15}$$

Combining Eqs. (2.15) and (2.9) gives

$$\delta \sim \frac{k_B T (1-\kappa)^4 R^4}{3A_s} = \frac{k_B T r_0^4}{3A_s}. \tag{2.16}$$

Equation (2.16) implies that, for a ternary QD with a strongly segregating species ($Pe >> 1$) at given T, increasing the segregation-strength parameter A_s leads to formation of core/shell-like structures with thinner shell regions; A_s is a thermodynamic property of the ternary system and, therefore, $A_s = A_s(x, T)$ in the notation used for the cases examined here. This capability to control the shell thickness of the QD through control of the

concentration boundary-layer thickness by tailoring *Pe* in the *Pe* >> 1 regime is highlighted in Fig. 2.2.

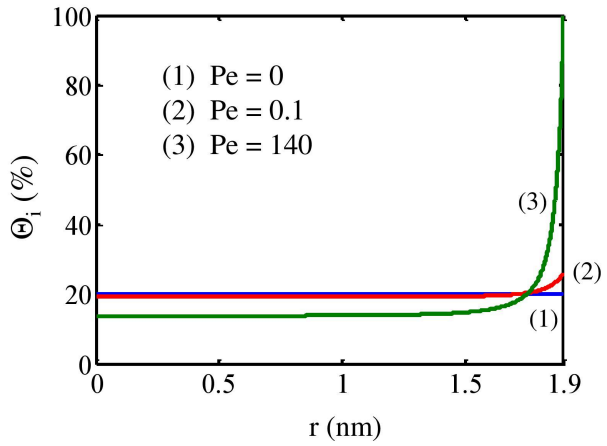

Figure 2.1. Equilibrium concentration profiles in ternary QDs of d = 3.8 nm for Pe = 0, Pe = 0.1, and Pe = 140 according to the Maxwellian-atmosphere solution of Eq. (2.14). The profiles range from uniform throughout the nanocrystal at Pe = 0 to the formation of a boundary layer near the nanocrystal surface at Pe = 140.

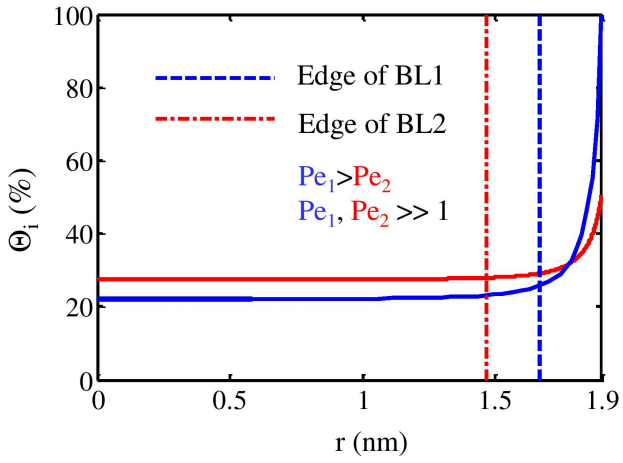

Figure 2.2. Comparison of concentration boundary-layer (BL) thicknesses in the equilibrium concentration profiles in ternary QDs of d = 3.8 nm for Pe_1 = 80 (forming BL1) and Pe_2 = 30 (forming BL2).

The predictions of the continuum transport model at steady state and at equilibrium, Eqs. (2.13) and (2.14), were validated by comparisons with results from a systematic protocol of first-principles-based atomistic simulations in several cases of relaxed $ZnSe_{1-x}Te_x$ and $In_xGa_{1-x}As$ QD configurations. Fitting the Maxwellian atmosphere of Eq. (2.14) to the equilibrium concentration profiles computed by Monte Carlo simulations [12] is then used to determine the values of the segregation-strength parameter A_s for various QD sizes and compositions.

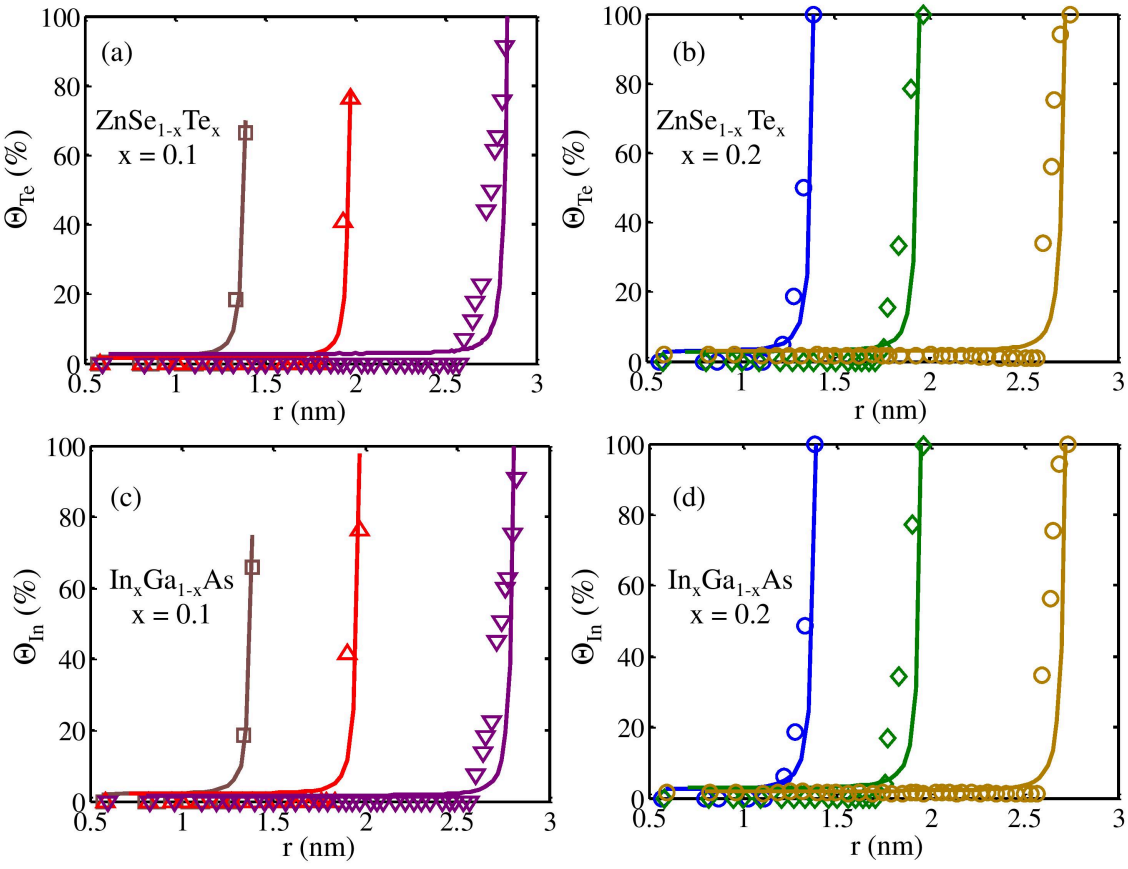

Figure 2.3. Equilibrium concentration profiles of Te in (a) $ZnSe_{0.90}Te_{0.10}$ and (b) $ZnSe_{0.80}Te_{0.20}$ and In in (c) $In_{0.10}Ga_{0.90}As$ and (d) $In_{0.20}Ga_{0.80}As$ with $d \sim 2.8$ nm, 3.8 nm, and 5.7 nm obtained by MC compositional relaxation (open symbols) and fitting of the MC results according to the Maxwellian-atmosphere solution of Eq. (2.14) (solid lines).

Table 2.1. Values of *Pe* and the segregation-strength parameter, A_s, from fitting the Maxwellian-atmosphere solution of Eq. (2.14) to the MC simulation results (compositional relaxation only) of Fig. 2.3 for $ZnSe_{0.90}Te_{0.10}$, $ZnSe_{0.80}Te_{0.20}$, $In_{0.10}Ga_{0.90}As$, and $In_{0.20}Ga_{0.80}As$ quantum dots with diameters d = 2.8, 3.8, and 5.7 nm, i.e., a total of twelve data sets (MC profiles). For all the simulations analyzed, the temperature is T = 300 K.

d (nm)	$ZnSe_{1-x}Te_x$	*Pe*	$A_s\times10^{45}$ (m^5 kg s^{-2})	$In_xGa_{1-x}As$	*Pe*	$A_s\times10^{45}$ (m^5 kg s^{-2})
2.8	x = 0.1	102	1.73	x = 0.1	104	1.76
3.8		139	5.33		149	5.71
5.7		205	24.1		350	41.1
2.8	x = 0.2	106	1.80	x = 0.2	123	2.09
3.8		140	5.37		164	6.29
5.7		212	24.9		363	42.6

Figures 2.3(a) and (b) show results for spherical nanocrystals of $ZnSe_{1-x}Te_x$ with x = 0.1 and 0.2, respectively, over the diameter range 2.8 nm $\leq d \leq$ 5.7 nm, while results for $In_xGa_{1-x}As$ spherical nanocrystals over the same range of diameters with x = 0.1 and 0.2 are shown in Figs. 2.3(c) and (d), respectively. In this fitting procedure, there is only one fitting parameter, as is evident from Eq. (2.14): the segregation strength A_s that determines *Pe*. The fitting is better for lower values of the overall constituent content, x, simply because both the species transport model, as formulated by Eqs. (2.1)-(2.3), and the elastic analysis, on which Eq. (2.3) is based, are rigorously valid in the dilute limit. The results of the fitting procedure for all 12 of the datasets (MC profiles) of Fig. 2.3 are listed in Table 2.1. The derived *Pe* values exhibit an almost linear dependence on the QD diameter. This can be understood from the definition of *Pe*, Eq. (2.9), which implies that, at constant T, $Pe \propto (A_s / r_0^4)R$. The variation of A_s with the QD diameter is attributed to the changes in the QD surface composition with increasing R and the resulting changes in the elastic parameters that determine A_s [32-34]. Aided by interpolation and extrapolation, these results for A_s can be used for kinetic analyses of drift and diffusion in

these ternary systems over a broad range of temperatures, as well as compositions and diameters for the ternary QDs.

2.3.2 Interdiffusion Kinetics in Ternary Quantum Dots

Having examined the equilibrium compositional distributions in ternary QDs, we now focus on the kinetics that governs the establishment of such compositional distributions, characteristic of self-assembled thermodynamically stable ternary QD configurations; in the QDs considered, this is the kinetics of diffusion of two different species from the same group of the periodic table in the same sublattice of the zinc-blende lattice. The transient BVP of Eqs. (2.9)-(2.12) can be used to interpret experimental measurements of concentration evolution during thermal annealing of ternary QDs and to determine diffusion coefficients and activation barriers, while segregation-strength parameters can be determined also by analysis of atomistic simulation results of equilibrium concentration as was done in the previous section. More importantly, the transient model can be used to make predictions of concentration profile evolution that are important to designing thermal annealing experiments of as grown ternary QDs to aid the self-assembly of thermodynamically stable ternary QDs.

Understanding the thermodynamic stability of alloyed and core/shell (or, in general, heterogeneous) QDs is particularly important, as a certain QD growth strategy may lead to configurations with compositional distributions away from equilibrium. During QD thermal processing or during the service of a device containing such QDs, these as grown configurations will evolve to their equilibrium states, given by the Maxwellian atmospheres as shown in the previous section. The evolution in their

compositional distribution may impact the electronic properties of the QDs significantly with respect to those of the as grown configurations. Recent thermal annealing experiments of colloidally synthesized ZnSe/ZnS core/shell QDs have demonstrated such a thermodynamic instability of a core/shell interface [13]. Specifically, ZnSe/ZnS core/shell QDs were synthesized and PL spectroscopy and X-ray photoelectron spectroscopy (XPS) were used on both the as synthesized and the annealed QDs to determine their properties and near-surface composition as a function of annealing time and temperature. These experimental results emphasized the importance of interdiffusion of Se and S atoms that facilitates the thermodynamic instability and leads to alloying of the initially pure ZnSe core and ZnS shell [13].

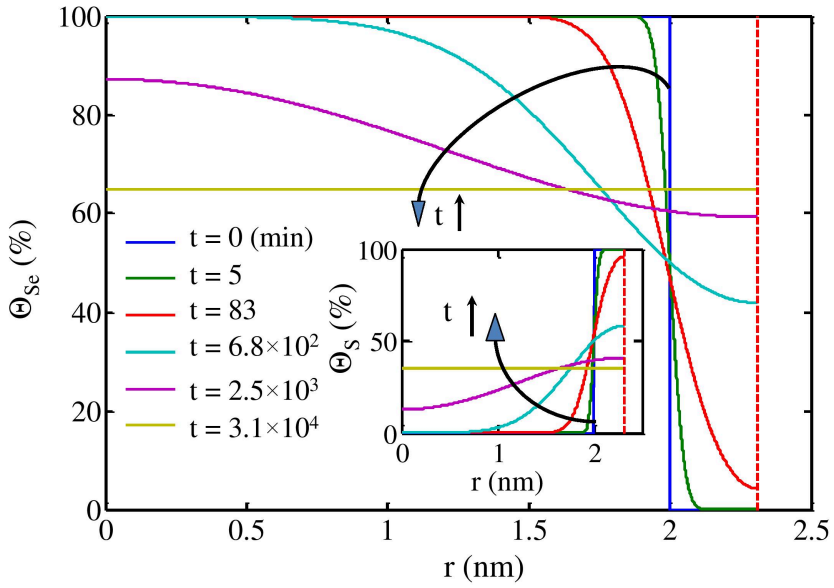

Figure 2.4. Computed evolution of the Se concentration profile in a ternary $ZnSe_{1-x}S_x$ QD from an initial compositional distribution that corresponds to a core/shell ZnSe/ZnS configuration due to interdiffusion during the thermal annealing of the QD. The corresponding evolution of the S concentration profile is shown in the inset. In both cases, the dashed vertical line marks the location of the ternary nanocrystal surface.

We applied Eqs. (2.1)-(2.5) to model the annealing of ZnSe/ZnS core/shell QDs that was studied experimentally in Ref. 13. Specifically, we simulated the annealing at 90 ^{o}C of ZnSe/ZnS core/shell QDs with diameter d = 4.62 nm, core radius R_c = 2.0 nm, and shell thickness of one monolayer, or 0.31 nm [2, 35]. We did not model the annealing of the QDs at the higher temperature (235 ^{o}C) in the experiments, due to a number of kinetic phenomena (such as partial desorption of the surfactant passivation layer from the QD surface) that may be activated at this higher temperature and are not accounted for by the model. In the numerical simulations, we use an Adams-Bashforth algorithm with adaptive time step for the time integration and a centered finite-difference scheme for the spatial discretization of the concentration field with a fine-resolution finite difference grid.

Representative results from our time-dependent numerical simulations are shown in Fig. 2.4 for the evolution of the Se concentration profile in the ternary QD. The initial ZnSe/ZnS core/shell configuration of Eq. (2.12), is the Heaviside step function shown at t = 0 that marks the initial location of the core/shell interface. The inset in Fig. 2.4 depicts the corresponding evolution of the S concentration profile, starting from the core/shell distribution with a ZnS shell. For both the Se and S profiles, the species concentration Θ is expressed in terms of the atomic fraction of the group-VI element (i.e., the percentage of group-VI species that is Se or S). Consistently with the experimental findings of Ref. 13, the simulation results demonstrate that the core/shell interface is not stable and that the original core/shell configuration changes due to interdiffusional transport: Se/S is transferred from/to the core to/from the original shell region; consequently, over time, the group-VI elements of the ternary QD are distributed increasingly more evenly throughout

the nanocrystal. The evolution of the concentration profiles is followed for over 500 hours, a long time period that is sufficient for the compositional distributions in the nanocrystal to reach their steady states at the temperature of 90 ^{o}C. The long-time profiles (> 500 h) of Fig. 2.4 indicate that the steady-state concentration distributions of Se and S are uniform, which corresponds to a randomly alloyed configuration of the ternary $ZnSe_{1-x}S_x$ nanocrystal. Finally, in order to fully quantify the species concentrations, we have satisfied the overall mass balance in the $ZnSe_{1-x}S_x$ nanocrystal, i.e., the total numbers of S and Se atoms in the nanocrystal, N_S and N_{Se}, respectively, are conserved throughout the duration of the annealing simulation. This overall balance also sets the value of the compositional parameter, x, i.e., $x = N_S/(N_{Se} + N_S)$ with N_S and N_{Se} being equal to the integrals over the QD volume of the corresponding concentration fields.

Before using these dynamical simulation results in the analysis of the XPS data of Ref. 13, we confirmed their validity by comparing the long-time-limit results with the exact solution to the steady-state model. These comparisons for the Se concentration profiles are shown in Fig. 2.5 and demonstrate excellent agreement between the numerical predictions and the exact analytical solutions. The accuracy of the numerical simulations is demonstrated in inset (a) in Fig. 2.5, where the numerical error, $\Delta\Theta_{Se}$, is plotted as a function of the finite-difference grid spacing, h. The straight line in this log-log plot corresponds to the least-squares fit of the results and has a slope of $1.96 \approx 2$, which confirms the $O(h^2)$ accuracy of the implemented centered finite-difference scheme [36]. Inset (b) shows a steady-state Se concentration profile that has been magnified in the nanocrystal surface region to highlight the weak surface segregation of Se atoms on

the nanocrystal surface; therefore, strictly speaking, the steady-state profile is not exactly uniform but exhibits a small deviation from uniformity in the surface region due to drift from the very weak segregation force that drives Se to the nanocrystal surface.

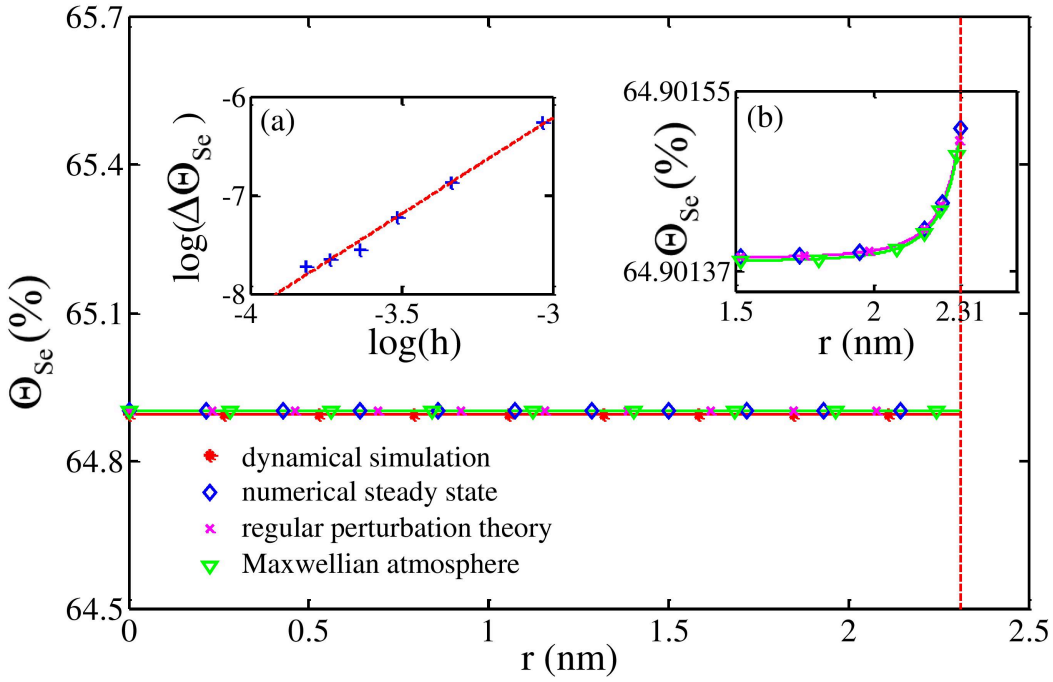

Figure 2.5. Steady-state Se concentration profile in a ternary $ZnSe_{1-x}S_x$ QD reached due to interdiffusional transport during the thermal annealing of the QD. The dashed vertical line marks the location of the ternary nanocrystal surface. The long-time-limit profile according to dynamical simulation, the numerical solution of the BVP at steady state, the steady-state solution of the BVP according to regular perturbation theory, and the Maxwellian atmosphere at equilibrium are compared and shown to be in excellent agreement with each other. Inset (a) depicts the convergence of the numerical solutions with the resolution of the employed finite-difference grid in a log-log plot of numerical error as a function of the grid spacing, h; the straight line corresponds to a least-squares fit to the results. The magnified profile in the nanocrystal surface region in inset (b) highlights the weak surface segregation of Se atoms.

Figure 2.6 shows the optimal fitting of the XPS data of Ref. 13 by the results of the model. The open symbols are the experimental data for the near-surface concentration evolution of Se and S atoms, $\Theta_{Se,ns}(t)$ and $\Theta_{S,ns}(t)$, respectively, over an XPS depth d_{XPS} = 0.55 nm from the nanocrystal surface. The solid lines are the

corresponding results from the numerical solution of the 1-D transient BVP of Eqs. (2.10)-(2.12) for the parameter values that provide the best least-squares fit to the data. The near-surface concentrations are expressed as atomic fractions

$$\Theta_{i,ns} \equiv \frac{N_{i,ns}}{N_{\mathrm{Se},ns} + N_{\mathrm{S},ns}}; i = \text{Se or S and } N_{i,ns}(\tau) = \int_{\kappa-\kappa_{\mathrm{XPS}}}^{\kappa} \Theta_i(\eta,\tau)\, \mathrm{e}^{-(\kappa-\eta)/\lambda} 4\pi\eta^2 d\eta, \quad (2.17)$$

where $\kappa_{\mathrm{XPS}} \equiv d_{\mathrm{XPS}}/R$ and the exponential decay in the integrant of the expression for $N_{i,ns}$ accounts for the XPS signal intensity decay with an inelastic mean free path λ, where $\lambda = \Lambda/R$ and Λ is taken to be equal to 2.1 nm. In our numerical procedure, the experimentally known materials and process parameters are kept fixed. However, we have explored how the numerical solutions vary with variation of these experimental parameters; e.g., the error bars in Fig. 2.6 indicate the range of the numerical solutions with varying the shell thickness of the initial ZnSe/ZnS core/shell configuration from 0.26 to 0.36 nm for an experimental shell thickness of 0.31 nm that gives the results represented by the solid lines.

From the results of Fig. 2.6, it is evident that the 1-D transient species transport model provides an excellent fitting of the experimental data. In our fitting procedure, there are two fitting parameters involved: the diffusion coefficient D through the definition of the dimensionless time τ appearing in Eq. (2.10) and parameter A_s that expresses the strength of the driving force for surface segregation of Se on the QD surface through the definition of Pe, Eq. (2.6). The derived parameter values that result in the best fit of the XPS data are $D = 2.52\times10^{-24}$ m^2/s and $A_s = 8.0\times10^{-56}$ m^{5}kgs^{-2}. These derived values have been used in the calculations that yielded the results of Figs. 2.4 and 2.5. The segregation strength A_s in this case is seen to be 10 orders of magnitude lower

than the derived values of A_s from fitting of MC equilibrium profiles (Table 2.1) in $ZnSe_{1-x}Te_x$ and $In_xGa_{1-x}As$ QDs with species that exhibit strong tendencies for surface segregation. This very low A_s value explains the formation of randomly alloyed configurations during the annealing of $ZnSe_{1-x}S_x$ QDs and the thermodynamic instability of ZnSe/ZnS core/shell QDs [13].

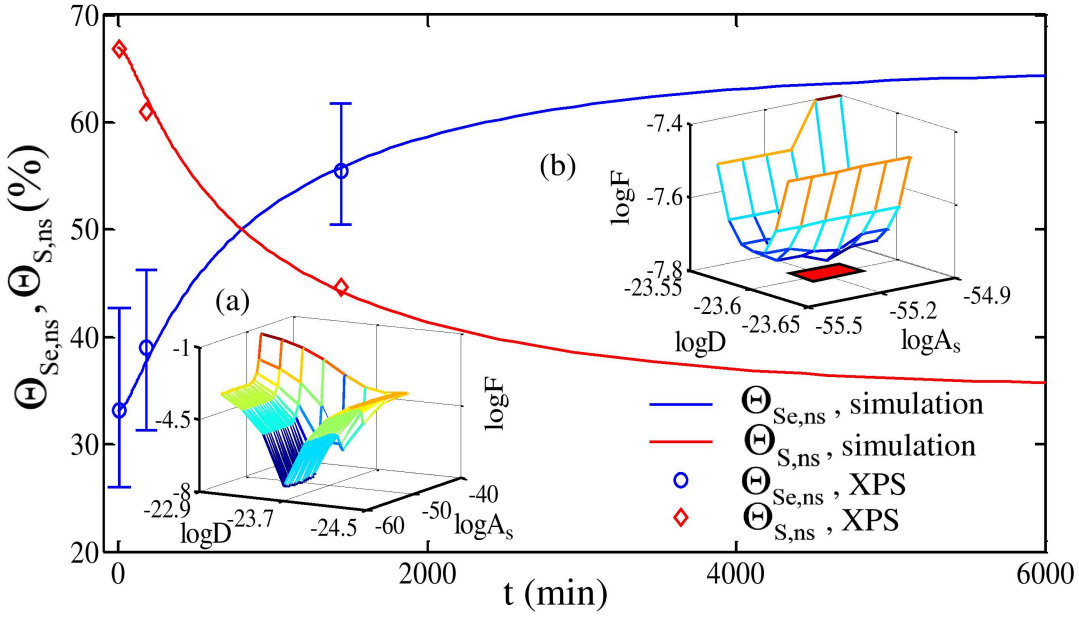

Figure 2.6. Optimal fitting of XPS data from Ref. 13 (open symbols) for the evolution of the near-surface concentration of Se and S atoms, $\Theta_{Se,ns}$ and $\Theta_{S,ns}$, respectively, during annealing of ZnSe/ZnS core/shell QDs at 90 ^{o}C over an XPS depth of 0.55 nm from the nanocrystal surface according to numerical solutions (solid lines) of the BVP of Eqs. (2.10)-(2.12). The error bars indicate the range of the numerical solutions with varying the shell thickness over a range of 0.1 nm about the experimental shell thickness. Inset (a) gives a logarithmic surface plot of the objective function F in the fitting procedure as a function of the fitting parameters D and A_s. Inset (b) gives a magnification of this surface plot in the vicinity of the optimum.

The derived diffusion coefficient D has a low value that is typical of solid-state diffusion. This diffusivity value was used to estimate the thermal activation energy for diffusion of Se and S in the ternary QDs. Specifically, we used for D the atomic-level kinetic expression for three-dimensional diffusion [30], i.e., $D = \Gamma a_h^2/6$, where Γ is the

atomic jump frequency and a_h is the atomic hop distance. Using for a_h the nearest-neighbor distance between group-VI atoms in the zinc-blende lattice, i.e., $a_h = a_0\sqrt{2}/2$ with a_0 being the equilibrium lattice parameter, and an Arrhenius-type expression for Γ yields

$$D = \frac{1}{6}\left(a_0 \frac{\sqrt{2}}{2}\right)^2 \nu_0 \exp\left(-\frac{E_a}{k_B T}\right). \tag{2.18}$$

In Eq. (2.18), ν_0 is the attempt frequency, T = 363 K, and E_a is the thermal activation energy for diffusion of Se or S in the zinc-blende lattice. Using a_0 = 5.41 Å for ZnS and an estimated attempt frequency of 11.6 THz [37], Eq. (2.18) yields an activation barrier for diffusion E_a = 1.23 eV. Experimental data are available in the literature for the diffusion of S and Se in ZnS, ZnSe, and $ZnSe_{1-x}S_x$ layers [38-40], including $ZnSe_{1-x}S_x$ films on ZnS and ZnSe substrates [38] and $ZnSe_{1-x}S_x$/ZnSe quantum wells [40]. From the data of Table 10 in Ref. 39 for S diffusion in ZnSe and using an Arrhenius expression for the T dependence of the diffusivity, we derive an activation barrier of 0.84 eV, while the data of Ref. 40 for S diffusion in $ZnSe_{1-x}S_x$ layers give a barrier of 1.7 eV. Clearly, our best estimate (of 1.23 eV) for E_a lies well within the activation-barrier range derived from experimentally reported diffusivity data.

Having established the capabilities of the transport model of Eqs. (2.1)-(2.5) for QD annealing simulations, we use the model to predict the near-surface concentration evolution in QDs that exhibit a much stronger tendency than $ZnSe_{1-x}S_x$ for species surface segregation. Such QDs include $ZnSe_{1-x}Te_x$ and $In_xGa_{1-x}As$, as established in the previous section. Here, we study the annealing of $ZnSe_{1-x}Te_x$ QDs prepared in various (as grown) initial configurations: these include randomly alloyed QDs, ZnSe/ZnTe

core/shell configurations, and ZnTe/ZnSe reverse core/shell configurations. We solve the transient BVP of Eqs. (2.10)-(2.12) numerically. In the numerical simulations, we use proper upwinding at the high *Pe* under consideration [36]. Specifically, we simulated the annealing at 235 ^{o}C of $ZnSe_{0.80}Te_{0.20}$ QDs with diameter d = 3.80 nm; the parameters have been chosen for consistency with preliminary experimental studies in such ternary QDs.

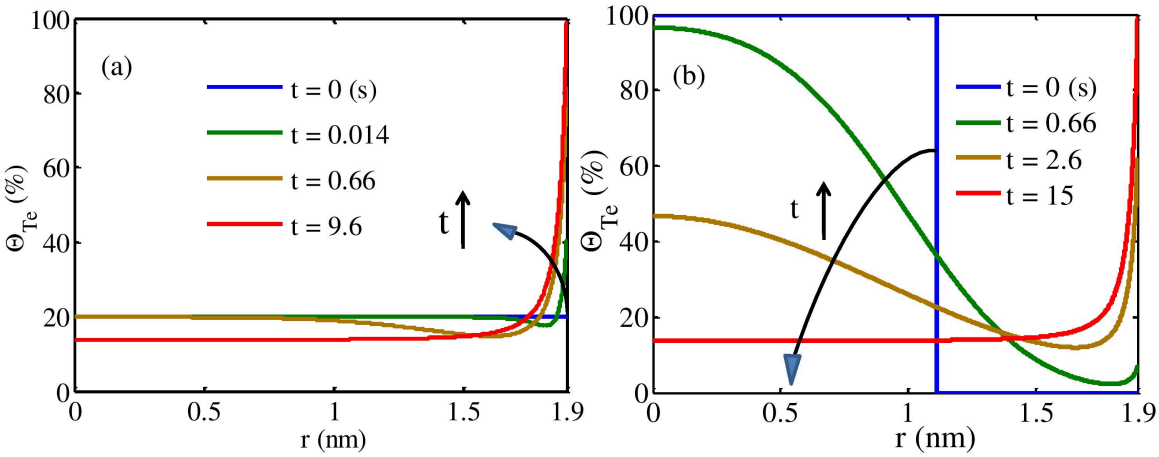

Figure 2.7. Computed evolution of the Te concentration profile in a ternary $ZnSe_{0.80}Te_{0.20}$ QD from an initial compositional distribution that corresponds to (a) a randomly alloyed configuration and (b) a ZnTe/ZnSe reverse core/shell configuration due to interdiffusion during the thermal annealing of the QD.

Results from our time-dependent numerical simulations are shown in Fig. 2.7 for the evolution of the Te concentration profile in the ternary QD. The profile evolution for a randomly alloyed $ZnSe_{0.80}Te_{0.20}$ and a ZnTe/ZnSe reverse core/shell configuration is shown in Figs. 2.7(a) and (b), respectively. These initial conditions correspond to the uniform distribution at t = 0 in Fig. 2.7(a) and the Heaviside step function at t = 0 in Fig. 2.7(b) that marks the location of the initially abrupt reverse core/shell interface. The Te concentration Θ_{Te} is expressed in terms of the atomic fraction of Te among group-VI

species in the nanocrystal. The value of *Pe* used in these simulations, *Pe* = 140, was taken from Table 2.1. Consistently with the atomistic simulation results in Refs. 12 and 10, these dynamical simulation results demonstrate that the randomly alloyed and reverse core/shell configurations are not stable and that Te and Se interdiffusion leads to the formation of a Te-deficient core region and a Te-rich shell region. We have also shown that ZnSe/ZnTe core/shell configurations with abrupt core/shell interfaces are not stable either, in the sense that the group-VI species interdiffusion generates a graded interface, that is, a core/shell-like structure with a diffuse boundary between the core and the shell regions instead of a sharp interface. In all cases, the evolution of the concentration profiles is followed for over 10 s at the annealing temperature of 235 ^{o}C, which is a sufficiently long time period for the compositional distributions in the nanocrystal to reach their steady states. All of the long-time profiles (>5 s) of Fig. 2.7 depict the formation of a Te concentration boundary layer at steady state that resembles very closely the Maxwellian atmosphere of Eq. (2.14). In order to fully quantify the concentrations of Te and Se, we have satisfied the overall mass balance in the $ZnSe_{1-x}Te_x$ nanocrystal, that is, the total numbers of Te and Se atoms in the nanocrystal, N_{Te} and N_{Se}, respectively, are conserved throughout the duration of the annealing. This overall atomic species balance also sets the value of the compositional parameter, x, that is, $x = N_{Te}/(N_{Se} + N_{Te})$; N_{Te} and N_{Se} are equal to the integrals over the spherical nanocrystal volume of the corresponding concentration fields. The tracking of dimensional time in the dynamical simulations requires knowledge of the diffusion coefficient and is discussed below. Finally, the two cases of profile evolution examined in Fig. 2.7 show that the time to steady state is longest for a ZnTe/ZnSe reverse core/shell initial configuration due to the longer

diffusional length scales involved in this case: all of the Te is initially in the core and diffuses from the core to the shell region, while all of the Se is initially in the shell and diffuses from the shell to the core region.

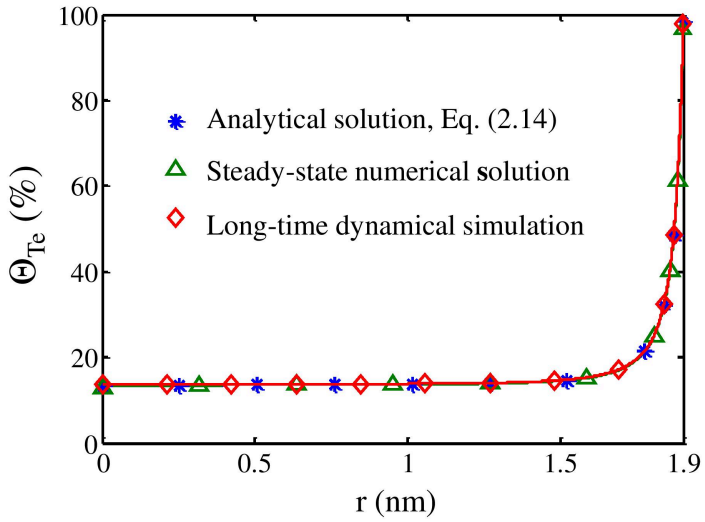

Figure 2.8. Steady-state Te concentration profile in a ternary $ZnSe_{0.80}Te_{0.20}$ QD reached due to interdiffusional transport during the thermal annealing of the QD from an initial ZnTe/ZnSe reverse core/shell configuration. The long-time-limit profile according to dynamical simulation, the numerical solution of the steady-state BVP, and the exact analytical solution of the steady-state BVP, Eq. (2.14), are compared and shown to be in excellent agreement with each other.

Before using these dynamical simulation results in the analysis of the near-surface concentration evolution based on Eq. (2.17), the validity of the 1-D transient model was confirmed further by comparing its long-time-limit results with the exact solution to the steady-state model that is given by the Maxwellian atmosphere of Eq. (2.14). These comparisons are shown in Fig. 2.8 for the Te concentration profile in the ternary $ZnSe_{1-x}Te_x$ QD and demonstrate excellent agreement between the numerical predictions, both the long-time-limit transient BVP solution and the steady-state BVP solution, and the exact analytical solution; this confirms the observation made in Fig. 2.7 on the relation of

the long-time-limit concentration profiles with the Maxwellian atmosphere: they are exactly equal. Moreover, the long-time-limit dynamical simulation results for the concentration profiles are found to be identical regardless of the initial configuration used in the simulation.

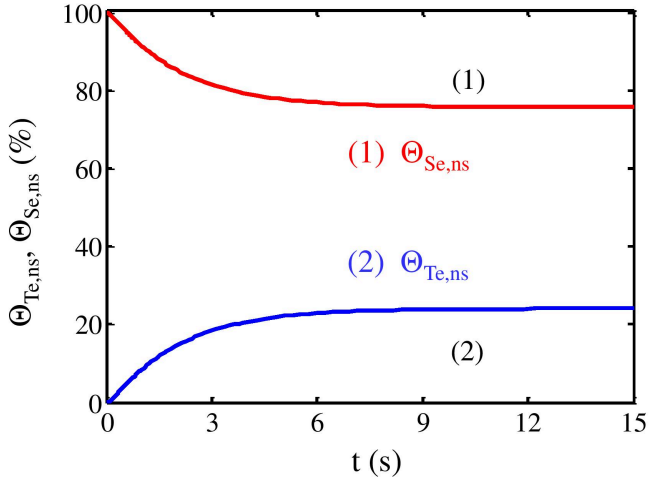

Figure 2.9. Computed evolution of the near-surface concentration of Se and Te atoms, $\Theta_{Se,ns}$ and $\Theta_{Te,ns}$, respectively, during annealing of ZnTe/ZnSe reverse core/shell QDs at 235 ^{o}C over an XPS depth of 0.65 nm from the nanocrystal surface.

The model predictions for the evolution of the near-surface concentration of the group-VI species, Te and Se, in the ternary QD are shown in Fig. 2.9 for an initial configuration of a reverse core/shell ZnTe/ZnSe QD; the profile evolution, $\Theta_i(\eta,\tau)$ for i = Te, for this initial configuration is given in Fig. 2.7(b). In addition to the integration of Eq. (2.17) with Λ = 1.9 nm in this case, reporting the evolution of $\Theta_{Te,ns}$ and $\Theta_{Se,ns}$ over dimensional time requires information for the diffusion coefficient D. This information cannot be provided by the equilibrium atomistic simulations. However, reasonable estimates of D are possible according to Eq. (2.18). ν_0 is around 10^{13} s^{-1} for most crystalline lattices. Using in Eq. (2.18), a_0 = 5.67 Å for ZnSe, T = 508 K for the

annealing process, and an estimated activation barrier for diffusion of Se or Te in the zinc-blende lattice E_a = 1.25 eV gives $D = 1.06 \times 10^{-19}$ m^2/s.

This value of D was used in the simulations that yielded the results of Fig. 2.7 and to make dimensional the $\Theta_{i,ns}$ evolution in Fig. 2.9. The results of Fig. 2.9 are valuable in designing annealing experiments to aid thermally the self-assembly of the equilibrium core/shell-like structures of the $ZnSe_{1-x}Te_x$ QDs. For the annealing temperature of 235 ^oC used here, the time to steady state is found to be only a few seconds and the plateau level of the near-surface concentration provides complementary information to the Maxwellian atmosphere for determining the Te-rich shell thickness and the graded interface region of the equilibrium, thermodynamically stable configuration. The very short time to steady state is due to the high annealing temperature and the small diffusional length scale (the QD radius) and should be contrasted with the time to steady state in the annealing experiment of Fig. 2.6 (> 100 h) at the low temperature of 90 ^oC. This very short equilibration time emphasizes the point made above about laboratory time scales sufficient to destabilize QD heterostructures that are not thermodynamically stable, such as the ZnTe/ZnSe reverse core/shell initial configuration here.

2.4 Summary and Conclusions

In summary, we analyzed the diffusional transport of atomic species in semiconductor ternary QDs driven by the tendency of certain species to segregate on the semiconductor nanocrystal surface. We developed a continuum transport model for such driven diffusional transport, validated it by comparisons of its predictions with those of first-principles based atomic-scale simulations, and used it to fit experimental data and atomistic simulation results to develop a database of transport properties in ternary QDs.

This database and the continuum model provide a valuable design tool for the development of thermal annealing processes that drive the assembly of core/shell-like structures from as grown QD configurations that may be kinetically locked at the low temperature of QD growth (by, e.g., colloidal synthesis techniques).

Our findings have various important implications for the development of ternary QDs with optimal function in optoelectronic and photovoltaic devices. A critical implication is for the stability of QDs grown as core/shell heterostructures through a two-step growth process, where a QD core is grown and then coated by a shell of different composition from that of the core. Although such a heterostructure may have very promising optoelectronic properties, afforded due to the presence of the core/shell interface, it may be thermodynamically unstable. During further thermal processing of the QD or during its service in a high-temperature environment, species diffusion in the QD, driven by the tendency of certain QD constituents for surface segregation, will destabilize the original core/shell interface with dramatic consequences for the QD's electronic properties. Given the small diffusional length scales in the QDs ($d \sim 5$ nm) and any high temperatures that enhance significantly the rates of diffusional processes in crystalline lattices, such QD instabilities may be realized over short laboratory time scales (from a few seconds to many hours) and have severe effects on the QD-based devices.

CHAPTER 3

CHARGE TRANSPORT IN ORGANIC PHOTOVOLTAIC ACTIVE LAYERS

3.1 Introduction

Organic polymer semiconductors and fullerene derivatives are widely researched as active layer materials for organic field effect transistors (OFETs), organic light emitting diodes (OLEDs), and solar cells [41-45]. Such organic materials are particularly attractive for these applications due to their room-temperature processing and their potential for large-scale manufacturing [46,47]. For organic photovoltaic applications, the device active layers can either be composed entirely of the organic polymers or the organic fullerene derivatives to form single-junction and tandem solar cells [48-50], or be incorporated into other inorganic materials to form hybrid tandem structures [51,52]. As OPV device efficiencies become more competitive, improving materials processing conditions for safety reasons becomes more important. Commonly used processing techniques involve organic film casting from chloroarene solvents that are volatile and cause risks of nephrotoxicity and hepatotoxicity [53-55], and should, therefore, be excluded in future processing strategies.

Toward this end, the use of nanoparticle assemblies as active layers is particularly appealing because their synthesis in aqueous solutions can reduce the usage of chlorinated solvents [56-58]. Moreover, the use of nanoparticle (NP) assemblies enables precise nanoscale control over the nanoparticle size, ratio, and internal structure [59-61]. An important feature of conjugated polymer nanoparticles is that they are stabilized by surfactants, which are expected to introduce trapping sites for electrons and holes and

impede charge transport. Yet, the observed hole mobility in surfactant-stabilized conjugated nanoparticle assemblies is comparable to that of pristine films [62]. In addition to charge mobility, charge trapping and detrapping also play an important role in the overall performance of these films as photovoltaic active layers. Even with comparable charge mobilities, the efficiency of OPV devices based on these nanoparticle assemblies is generally lower than those based on drop cast thin films. Processing conditions, surface contact layers, and individual nanoparticle structural designs have been employed to improve the efficiency of these OPV devices [63-65]. However, the relations between the active layer morphology and functional layers in the device with the charge transport properties of the active layers and the device power conversion efficiency are neither quantitatively determined nor well understood. The purpose of this chapter is to demonstrate quantitatively the comparable charge transport efficiency in conjugated nanoparticle assemblies and pristine films, investigate the effects of stabilizing surfactants, and simulate charge transport in such OPV devices based on self-assembled nanoparticles to set the stage for designing OPV devices with optimal performance and functionality.

First-principles density functional theory calculations relate atomic-scale and nanoscale structure with charge carrier transport properties but cannot provide a direct link between OPV device performance and active layer morphology and device layout [66-68]. Kinetic Monte Carlo and molecular-dynamics simulations can relate the active layer morphology with the device efficiency but require as input the active layer morphology [69,70], which can be generated by various direct or indirect methods [69,71,72]. These approaches may lead to unrealistic predictions of the active layer

morphology, especially for the nanoparticle assembly systems of interest to this study, since, e.g., the properties of surfactants surrounding the nanoparticles and the possible formation of jammed coassemblies [73] of nanospheres are fairly complicated to capture by these methods. Deterministic charge carrier transport models, i.e., drift-diffusion-reaction models for the charge carrier density fields in the active layer, have been applied successfully to simulating electron and hole transport in organic photovoltaic devices with active layer morphologies of bulk heterojunctions (BHJs) and planar heterojunctions, but not of nanoparticle assemblies [74-76]. Such coarse-grained homogenized models, when properly parameterized through experimental measurements of transient and steady photocurrents, relate directly the multi-physical processes in the active layer with the device efficiency without the requirement to reproduce the detailed active layer morphology.

In our study, we apply this transport modeling approach to derive nanostructure-property-function relations in OPV devices with active layers of nanoparticle assemblies with the individual nanoparticles consisting of the electron donor or/and the electron acceptor materials. In Section 3.2, detailed charge transport models are developed. In Section 3.3.1, we examine hole transport dispersivity in thin films and nanoparticle assemblies of P3HT and explore the effects of surfactant on hole trapping. In the experiments we simulate, the procedures followed for sample preparation and characterization and for the measurement of transient photocurrents were presented in Ref. 62. P3HT thin films were drop cast on indium tin oxide (ITO) substrates. Some of the nanoparticle assemblies were prepared after centrifugal filtration of the dispersion in order to remove excess surfactant molecules. Both non-centrifuged and centrifuged

nanoparticle assemblies were spray coated on the ITO substrates. A thin aluminum (Al) film was then thermally deposited on the P3HT layers. The Al electrode was positively biased with respect to the ITO electrode. 355-nm pulsed laser illumination was applied near the Al electrode. The time of flight method was used to determine hole mobilities [62]. Systematic experiments on various samples under different applied biases demonstrated hole mobility in assemblies of surfactant-surrounded nanoparticles comparable with those of drop cast P3HT thin films. It was also found that the presence of excess surfactant in P3HT nanoparticle assemblies increased their hole transport dispersivity [62]. The deterministic, phenomenological drift-diffusion-reaction model is validated for hole transport in P3HT thin films and nanoparticle assemblies, which can reproduce experimental data for photocurrent evolution measured by TOF experiments in samples of these materials with different nanostructures and over a range of applied voltages. The model accounts for the kinetics of hole trapping and detrapping in the various P3HT films and is used to characterize the corresponding nanostructures in terms of their hole transport dispersivity, to explain the role of excess surfactant molecules in hole trapping for assemblies of P3HT nanoparticles, and to explore the potential of using nanoparticle assemblies as active layers in OPV devices. The effects of incorporating PMMA and PS nanoparticles to P3HT nanoparticle assemblies are studied in Section 3.3.2.

A strategy has been developed to fabricate through aqueous solution processing and control over multiple length scales the morphology of active layers consisting of nanoparticle assemblies for efficient OPV devices [61,65]. These active layers consist of P3HT:PCBM blend or separate self-assembled spherical nanoparticles. In blend NP

assemblies, individual nanoparticles contain both electron donor and electron acceptor materials (i.e., both P3HT and PCBM), while in separate NP assemblies, individual nanoparticles contain either the donor or the acceptor material only (i.e., only P3HT or only PCBM). In the experimental studies [61], nanoparticle dispersions were spin coated onto PEDOT:PSS-coated ITO substrates. The PEDOT:PSS layer was treated in UV-O_3 for improved surface wettability [65]. A thin PCBM layer was then spin coated onto the active layer as a buffer layer. Finally, a Ca/Al cathode electrode was placed on top of the PCBM/P3HT:PCBM/PEDOT:PSS/ITO layered structure through vapor deposition. Systematic electrical measurements and structural characterization demonstrated that continuous pathways for both electron and hole transport were formed throughout the nanoparticle assemblies and that the OPV device performance was tunable by controlling nanoparticle size and ratio. In Section 3.3.3, our charge transport modeling reproduces the experimental measurements of transient and steady-state photocurrents in OPV devices with active layers of P3HT:PCBM NP assemblies and elucidates quantitatively the differences in charge transport properties between the two types of nanoparticle morphology (blend and separate NP assemblies) and the effects on charge transport and device performance of nanoparticle size and ratio. More importantly, we explain the effects of the device layout design on the device J-V characteristics and predict the device performance as a function of the active layer thickness. In Section 3.4, the most important conclusions are summarized.

3.2 Charge Transport Model Description

3.2.1 Development of Hole Transport Model

For a quantitative analysis of hole transport in the above three types of P3HT thin films and nanoparticle assemblies, we have developed a comprehensive one-dimensional (1-D) transient drift-diffusion-reaction model. The model accounts for hole trapping and detrapping in addition to hole diffusion and drift and consists of coupled boundary-value problems (BVPs) for the evolution of the free and trapped hole density fields in the polymer layer and for the electrostatic potential distribution in the material, governed by the following equations:

$$\frac{\partial p_f}{\partial t} = \frac{1}{e}\frac{\partial}{\partial x}(\mu_p k_B T \frac{\partial p_f}{\partial x} - \mu_p p_f eE) - \frac{\partial p_t}{\partial t}, \tag{3.1}$$

$$\frac{\partial p_t}{\partial t} = C_t(P_t - p_t)p_f - C_{dt}p_t, \tag{3.2}$$

and $$\frac{\partial^2 \Phi}{\partial x^2} = -\frac{e(p_f + p_t)}{\varepsilon_0 \varepsilon}. \tag{3.3}$$

Equation (3.1) describes the evolution of the free hole density $p_f(x,t)$, where $p_t(x,t)$ is the trapped hole density. In Eq. (3.1), t, e, and x denote time, elementary charge, and the coordinate along the film thickness direction and perpendicular to the electrodes, respectively, k_B is Boltzmann's constant, T is temperature, and E is the magnitude of the electric field, $\mathbf{E} = E\,\mathbf{e}_x$, directed along x. The hole mobility, μ_p, is taken to follow the Poole-Frenkel relation [77], $\mu_p = \mu_0 \exp(\gamma |E|^{1/2})$, with μ_0 and γ being the zero-field mobility and the field dependence coefficient, respectively. For the free holes, boundary

conditions of thermionic injection with image charge effects [78] were applied for the hole fluxes at the polymer/electrode interfaces, $x = 0$ and $x = L$. Equation (3.2) expresses the kinetics of hole trapping and detrapping with the initial condition that no generated charges are trapped, $p_t(x, t = 0) = 0$; C_t and C_{dt} are the trapping and detrapping kinetic rate coefficients, respectively, and P_t is the density of trapping sites in the polymeric material. Trapping-detrapping kinetics according to Eq. (3.2) assumes a single trapping energy level. Equation (3.3) is Poisson's equation for the electrostatic potential Φ, $E = -\partial\Phi / \partial x$, ε_0 is the vacuum permittivity and ε is the relative permittivity of the material; $p \equiv p_f + p_t$ is the total density of holes. Dirichlet boundary conditions for Φ were applied at $x = 0$ and $x = L$, as determined by the applied potentials at the two electrodes. As initial condition for the free hole density, we use an exponentially decaying (from $x = 0$) distribution, $p_f(x, 0) = P_0 \exp(-x/\lambda)$ [79], where λ is on the order of the penetration depth of the exciting light.

We solved the coupled BVPs governed by Eqs. (3.1)-(3.3) numerically using the finite-difference method for domain discretization. To avoid numerical instabilities in steep propagating charge fronts caused by strong electric fields, we employed upwinding [36] for the computation of the drift flux in Eq. (3.1). The convergence of the numerical results with refining the finite-difference grid resolution was ensured by using fine grids in the numerical simulations (with as many as $n = 6000$ grid points). We implemented the implicit Euler method for time stepping Eqs. (3.1) and (3.2) and calculated the transient photocurrent $I(t)$, by integrating the local free hole flux (current density) over the domain and averaging, according to the equation

$$I(t) = A\frac{1}{n}\sum_{i=1}^{i=n} j_i = \frac{1}{n} A\mu_0 \sum_{i=1}^{i=n} \exp(\gamma\sqrt{|E_i|})(-k_B T \frac{\partial p_{fi}}{\partial x} + p_{fi} e E_i), \quad (3.4)$$

where A is the film cross-sectional area (contact area with the electrodes) and j is the current density. For simplicity, Eq. (3.4) assumes a uniform grid of n points (nodes "i"); the subscripts i in the quantities of the right-hand sides of Eq. (3.4) denote the nodal values of the quantities.

3.2.2 Development of Charge Transport Model for Electrons and Holes

The transient model for the description of electron and hole transport in P3HT:PCBM blend and separate nanoparticle assemblies is extended beyond that for hole transport in P3HT nanoparticle assemblies that we developed above. These models are based on drift-diffusion-reaction equations for the charge carrier densities coupled with equations for the description of charge pair kinetics and the distribution of the electric field in the active layer subject to the proper boundary conditions. The complete set of these governing equations is

$$\frac{\partial n_f}{\partial t} = \frac{\partial}{\partial x}\left(D_n \frac{\partial n_f}{\partial x} + \mu_n n_f E\right) + k_{diss} X - C_{bi}\gamma n_f p_f - \frac{\partial n_t}{\partial t} + I_L G_0, \quad (3.5)$$

$$\frac{\partial n_t}{\partial t} = C_{t,n}(N_t - n_t) n_f - C_{dt,n} n_t, \quad (3.6)$$

$$\frac{\partial p_f}{\partial t} = \frac{\partial}{\partial x}\left(D_p \frac{\partial p_f}{\partial x} - \mu_p p_f E\right) + k_{diss} X - C_{bi}\gamma n_f p_f - \frac{\partial p_t}{\partial t} + I_L G_0, \quad (3.7)$$

$$\frac{\partial p_t}{\partial t} = C_{t,p}(P_t - p_t) p_f - C_{dt,p} p_t, \quad (3.8)$$

$$\frac{\partial X}{\partial t} = -k_{rec}X - k_{diss}X + C_{bi}\gamma n_f p_f, \tag{3.9}$$

and

$$\frac{\partial^2 U}{\partial x^2} = -\frac{e\left(p_f + p_t - n_f - n_t\right)}{\varepsilon_0 \varepsilon_r}. \tag{3.10}$$

Equations (3.5)-(3.8) govern the dynamics of the density fields of free electrons (n_f), trapped electrons (n_t), free holes (p_f), and trapped holes (p_t), respectively, while Eq. (3.9) governs the dynamics of the density field of bound electron-hole pairs (X). The above equations, subject to their initial and boundary conditions (discussed below), constitute a one-dimensional (1-D) continuum-medium model with field variables expressed as (spatial) functions of x only; this is because both the driving force for free charge carrier diffusion and the applied electric field are directed along x (the direction normal to the electrode planes) and any small local variations along the y and z directions can be averaged out effectively. Moreover, the random packing of the NP assemblies under consideration here implies that carrier diffusion in the active layer is isotropic and justifies the use of isotropic transport properties in the model. It should be mentioned that similar 1-D continuum-medium models have been applied successfully for simulating charge transport in BHJ and bilayer solar cells [74,75,80]. It has also been demonstrated that the results of such 1-D continuum models agree very well with those of fully three-dimensional (3-D) models [81]. These species balance (continuity) equations are coupled self-consistently with Eq. (3.10), i.e., Poisson's equation for the electrostatic potential (U) in the active layer. All of the above quantities (dynamical field variables) are functions of x, the direction normal to the planes of the electrodes that confine the

active layer with any dependences on the lateral directions y and z neglected or averaged out, and time t. In Eqs. (3.5)-(3.10), e, k_B, T, ε_0, and ε_r denote the elementary charge, Boltzmann constant, absolute temperature, vacuum permittivity, and relative permittivity of the active layer material, respectively. A typical value, $\varepsilon_r = 3.5$, is chosen for the relative permittivity of organic semiconducting polymers [82]. The diffusion coefficients, D_i ($i = n$ or p referring to electrons and holes, respectively), are related to the respective charge carrier mobilities, μ_i, through the Einstein relation, $D_i = \mu_i k_B T/e$. The electric field is given by the gradient of the electrostatic potential as $\mathbf{E} = -\partial U/\partial \mathbf{x} = E\mathbf{e}_x$ in our one-dimensional representation with $\mathbf{e}_x$ being the unit vector along x and $E = -\partial U/\partial x$, and is perpendicular to the electrodes. It should be mentioned that μ_i and E are related through the Poole-Frenkel relation for the field dependence of the charge carrier mobility, $\mu_i = \mu_{i0} \exp(\beta_i |E|^{1/2})$, where μ_{i0} is the zero-field mobility and β_i is the corresponding field dependence coefficient. Equations (3.6) and (3.8) govern the charge carrier trapping and detrapping kinetics; in Eqs. (3.6) and (3.8), N_t and P_t denote electron and hole trap densities, respectively, and $C_{t,i}$ and $C_{dt,i}$ denote the trapping and detrapping rate coefficients, respectively. Trapping-detrapping kinetics according to Eqs. (3.6) and (3.8) assumes a single trapping energy level for each of the charge carriers, i.e., electron and hole, respectively. Although Gaussian or exponential distributions of trapping energies in the active layers of interest are more realistic [83,84], they introduce multiple sets of trapping and detrapping rate coefficients in the model, which complicates needlessly the fitting procedures in the fitting of modeling predictions to experimental data and is beyond the scope of this thesis. In Eqs. (3.5) and (3.7), I_L is the relative light intensity and G_0 is the free electron and hole generation rate at unit light intensity. $I_L = 1.0$ is used

for the simulation of transient photocurrents in TOF experiments and $I_L = 2.08$ is used for the simulation of steady-state J-V characteristics under an incident light intensity of 100 mW/cm^2 [42,65]. For simulations of both types of experiment (TOF and steady light exposure), we have found that the models provide better reproduction of the experimental data if an effective free charge carrier generation rate G_0 is considered explicitly in Eqs. (3.5) and (3.7) instead of using only a bound electron-hole pair generation rate in Eq. (3.9), which is typically done for charge transport modeling in bulk-heterojunction photovoltaic devices [74,75,80]. In fact, multiple exciton dissociation pathways are possible [85,86]. Further theoretical investigation of the dynamics of charge pair separation, including hot exciton dissociation, requires accurate quantum chemical calculations of the energy levels of singlet exciton states and charge transfer states [85,87,88], in conjunction with experimental probing of the ultrafast dynamics of photoinduced absorption, which is beyond the scope of this thesis because it does not affect directly the charge carrier transport boundary-value problem (BVP) within the theory level required to solve this BVP. However, understanding the time scales that govern the kinetics of exciton dissociation is important for making the BVP under consideration well-posed. The reason for this is because, no matter which dissociation pathway the charge pairs go through, the characteristic time scales are all on the order of femtosceonds [85,89,90], i.e., orders of magnitude faster than the characteristic time scales for charge carrier transport probed by our model; this clear separation of time scales also justifies the use of non-zero initial conditions for electrons and holes (carrier densities in the $t \rightarrow 0$ limit that is reached mathematically before the time scale for exciton dissociation is approached), which is implemented in our model. In fact, adopting the

typical initial condition for a non-zero initial density of charge pairs yields (upon fitting experimental data) an initial charge separation distance of ~2 nm, which is a rather high value, generally consistent with that predicted in Ref. 80 where the traditional initial condition was implemented. Such a high value of a_0 implies an extremely weak electron-hole binding energy, outside (i.e., much lower) than the typical exciton binding energy range [91], which essentially would contradict the initial condition for exciton generation with the excitons being so weakly bound. The bimolecular recombination rate coefficient γ follows Langevin theory [92], according to which $\gamma = e(\mu_n + \mu_p)/(\varepsilon_0\varepsilon_r)$. However, the actual recombination rates have been found to be lower than those predicted by Langevin theory [93-95], which is accounted for in our model by using a prefactor, C_{bi}, in the expression for bimolecular recombination kinetics in the last term of the right-hand side of Eq. (3.9). Finally, in Eq. (3.9), k_{rec} and k_{diss} denote the geminate recombination and the bound electron-hole pair dissociation rate coefficients. The latter rate coefficient is expressed according to Onsager-Braun theory [96-98] as

$$k_{diss} = \frac{3\gamma}{4\pi a_0^3} \exp\left(-\frac{E_B}{k_B T}\right) \frac{J_1\left(2\sqrt{-2b}\right)}{\sqrt{-2b}}, \tag{3.11}$$

where a_0 is the bound charge pair separation distance, $E_B = e^2/(4\pi\varepsilon_0\varepsilon_r a_0)$ is the binding energy of a bound electron-hole pair, $b = e^3E/(8\pi\varepsilon_0\varepsilon_r k_B{}^2T^2)$, and J_1 is the first-order Bessel function of the first kind.

The boundary-value problems for the field variables n_f, n_t, p_f, p_t, X, and U of Eqs. (3.5)-(3.10) are solved subject to a complete set of boundary and initial conditions to make these problems well-posed. Thermionic injection in the presence of an image potential and surface recombination were applied for the free electron and hole fluxes at

the metal/organic interfaces between the active layer and the electrodes [78]. Dirichlet boundary conditions for the electrostatic potential U were applied by specifying the applied biases at the two electrodes used in the experiments. In the TOF experiments we have simulated, the active layer thicknesses were 1.6 μm and 2.3 μm for blend and separate NP assemblies, respectively, and are used to determine the domain boundaries ($x = L$). Free charge carriers were generated near the Al electrode by a 355-nm laser pulse. For simulation of TOF experiments, we used exponentially decaying distributions of free electrons and holes as the initial conditions [79]. For simulating the steady continuous illumination experiments that yielded J-V curve measurements, the active layer thicknesses (for setting domain boundaries) were around 200 nm as determined by profilometry. For solving the corresponding problems, we applied uniform distributions of photogenerated free charge carriers, i.e., G_0 was treated as a parameter and not as a field variable. Finally, for the initial conditions for the trapped densities of Eqs. (3.6) and (3.8), trapped electron and hole densities were taken to be equal to zero before light exposure.

We solved the coupled boundary-value problems governed by Eqs. (3.5)-(3.10) numerically using the finite difference method for domain discretization. To avoid numerical instabilities associated with the formation of steep propagating charge fronts caused by strong electric fields, we employed an upwinding scheme for the computation of the drift fluxes in Eqs. (3.5) and (3.7) in a similar manner with the implementation of Ref. 76. For integrating Eqs. (3.5)-(3.9) in time for the solution of the transient problems (simulation of TOF experiments), we implemented the implicit Euler method for time

stepping with adaptive time steps. At each recorded time step, the transient photocurrent $I(t)$ is averaged throughout the active layer according to the equation

$$I(t) = A\frac{1}{N}\sum_{k=1}^{k=N}(j_{n,k} + j_{p,k})$$

$$= \frac{1}{N} A \sum_{k=1}^{k=N}\left[\mu_{n0}\exp\left(\beta_n\sqrt{E_k}\right)\left(k_B T\frac{\partial n_{f,k}}{\partial x} + n_{f,k}eE_k\right) + \mu_{p0}\exp\left(\beta_p\sqrt{E_k}\right)\left(-k_B T\frac{\partial p_{f,k}}{\partial x} + p_{f,k}eE_k\right)\right],$$

where A = 6 mm^2 is the cross-sectional area of the film that constitutes the active layer, $j_{i,k}$ is the local current density at each node (grid point) k, and N is the number of grid points in the finite-difference grid used in the numerical simulations.

3.3 Results and Discussion

3.3.1 Analysis of Hole Transport in Pristine Thin Film and Nanoparticle Assemblies of Poly(3-hexylthiophene)

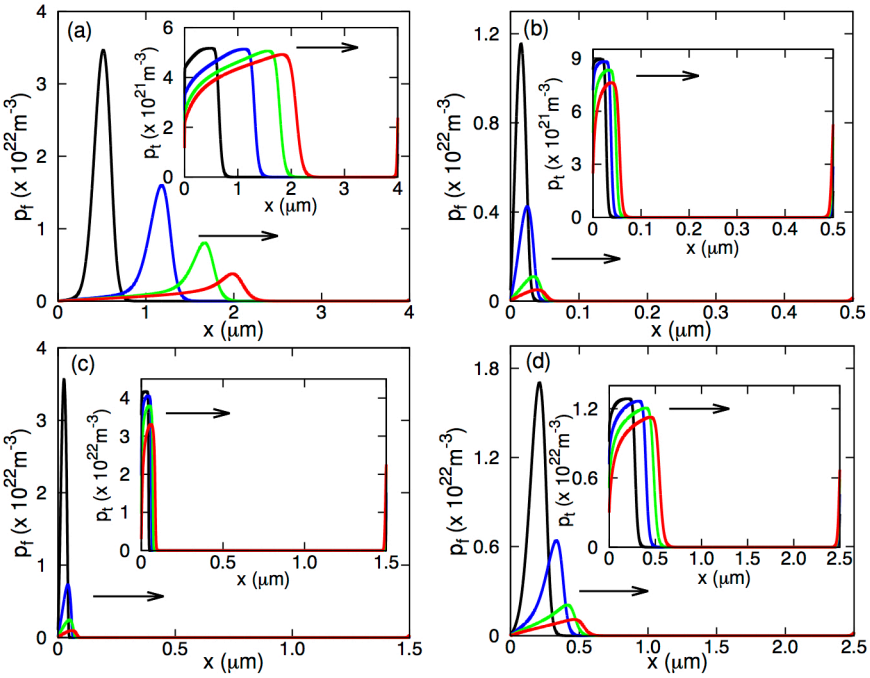

Figure 3.1. Simulated evolution (with time as indicated by the arrows) of free and trapped (insets) hole density profiles in P3HT sample (a) P1 under bias of 9 V, (b) P2 under 2 V, (c) P3 under 4 V, and (d) P4 under 4 V. The corresponding time instants for the profiles shown are (a) 19, 47, 71, and 90 μs; (b) 1.6, 3.7, 9.0, and 19 μs; (c) 4.8, 14, 31, and 96 μs; and (d) 23, 45, 78, and 129 μs. For the simulations, the values for the transport coefficients, kinetic parameters, and material properties used are within the range of the fitting parameter values reported in Table 3.1.

Before comparing the predictions of our model with the experimentally measured transient photocurrents in our P3HT samples, we validated the model by fitting its predictions to the experimental $I(t)$ data from the TOF measurements of Ref. 77 for nondispersive hole transport in the polyfluorene copolymer poly[(9,9-dioctylfluorenyl1-2,7-diyl)-co-(4,4'-(N-(4-sec-butylphenyl))diphenylamine)]. The model reproduced the data successfully throughout the duration of the TOF experiment, including the initial

increase, plateau region, and tail region of the transient photocurrent [77]. Having validated the model, we solved the coupled BVPs governed by Eqs. (3.1)-(3.3) and fitted our experimental $I(t)$ measurements for our P3HT samples, thus obtaining as fitting parameters hole transport properties, kinetic coefficients, and material properties for the different nanostructured P3HT films used in the TOF experiments.

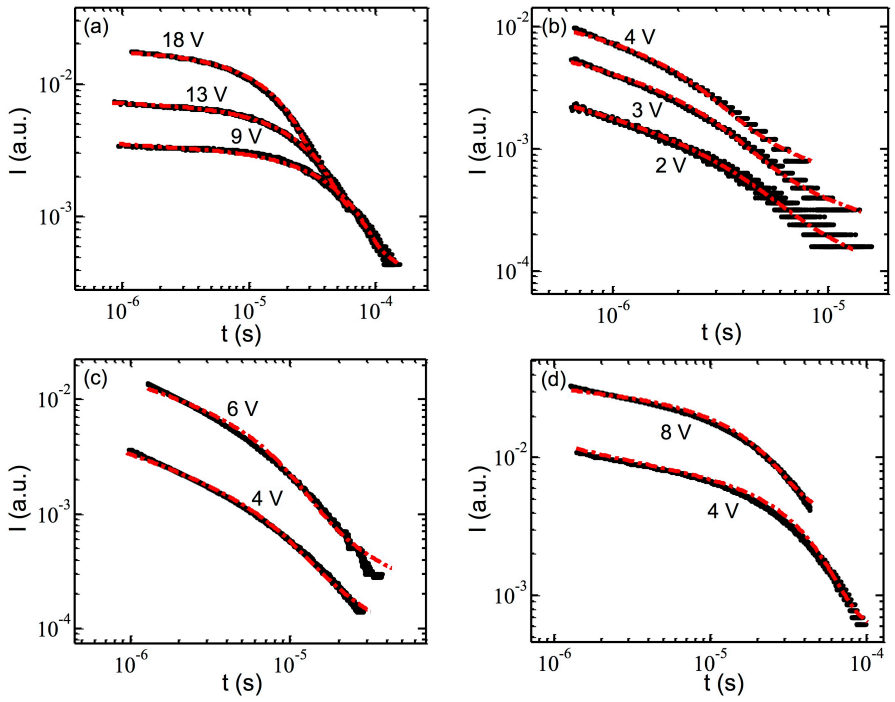

Figure 3.2. Best fits of simulation predictions (red dot-dashed lines) to experimental data (black solid circles) for photocurrent evolution I(t) under various applied biases in P3HT samples (a) P1, (b) P2, (c) P3, and (d) P4. For every film, the contact area with the electrodes is A = 6 mm^2.

We modeled hole transport under various applied biases in a 4-μm-thick P3HT drop cast thin film (sample P1), thin films of non-centrifuged nanoparticle assemblies with excess surfactant molecules of thickness equal to 0.5 μm (sample P2) and 1.5 μm (sample P3), and a 2.5-μm-thick film of centrifuged nanoparticle assemblies with the

excess surfactant molecules removed (sample P4). We found that hole transport dynamics is significantly different in these films of different nanostructures. Figures 3.1(a)-(d) show the evolution of the free hole density profiles in these four samples under certain applied biases; in each figure, the inset depicts the evolution of the corresponding trapped hole density profile. It is evident that trapping and detrapping of charge carriers due to structural defects in the amorphous layer distort the charge density profile from a Gaussian distribution [99]. The peak locations of the free and trapped hole packets propagate in the polymeric materials of our samples at speeds determined by the hole mobility and the electric field strength. In P1, Fig. 3.1(a), the overall hole distribution is skewed and tail regions are formed on its back since trapped holes cannot escape from their trap states fast enough to catch up with the free carriers; once these holes are released (detrapped), they contribute to the free hole density. However, in P2 and P3, Figs. 3.1(b) and 3.1(c), respectively, the distortion of the free and trapped hole density distributions from Gaussians is much less pronounced than that in P1, which indicates that these two samples are characterized by a much faster hole detrapping rate. In addition, the peaks of these hole packets move slower than that in P1, suggesting lower hole mobilities for these two samples. Moreover, the peaks of the hole distributions in P2 and P3 are lowered much faster than that of P1, which is expected to result in a faster decrease in the generated transient photocurrent. Finally, in P4, Fig. 3.1(d), the hole distributions are skewed Gaussians with fronts for both free and trapped holes propagating and exhibiting subtle tails for the free holes and almost rectangular-shaped tails for the trapped holes, similar to those of P1, implying a slow detrapping rate for this sample too.

We have fitted the predictions of numerical simulations according to the hole transport model governed by Eqs. (3.1)-(3.3) to the experimental measurements of transient photocurrent $I(t)$ in the four samples P1, P2, P3, and P4 with the zero-field mobility μ_0, kinetic parameters C_t and C_{dt}, and material properties P_0 and P_t treated as fitting parameters. The field-dependence coefficient γ was determined by fitting simulation predictions to experimental data under different applied voltages. Figure 3.2 compares simulation results with experimental data for photocurrent evolution, $I(t)$, presented in log-log plots by showing best fits of simulation predictions (red dot-dashed lines) to the experimental data (black solid circles) for the four P3HT samples, P1, P2, P3, and P4, under various applied biases. The comparison focuses on the time period after ~0.5 μs from the initiation of the experiment, since this initial transient stage is dominated by the discharge current at the polymer-electrode interface as opposed to charge carrier transport in the P3HT layer. In each case, the simulation results reproduce successfully the measured transit time, which is a metric of the characteristic time for the majority of the holes to reach the anode and is determined experimentally as the time corresponding to the intersection of the two linear regions in the logarithmic (log-log) plot of photocurrent evolution. Moreover, the simulation results capture successfully the entire dynamical behavior of the charge carriers in the examined P3HT materials of different nanostructure and reproduce the experimental transient photocurrent data very well for all samples and applied voltages, which validates further our model based on Eqs. (3.1)-(3.3). It is evident from Fig. 3.2 that the slopes of the first linear regions of their photocurrent transients in P2 and P3, Figs. 3.2(b) and 3.2(c), are much steeper than those for P1 and P4 that are much closer to zero, Figs. 3.2(a) and 3.2(d). These

differences in the $I(t)$ slopes in the first linear regions of the corresponding log-log plots reflect the faster rates of decrease in the hole densities over a short time period for samples P2 and P3 exhibited in Figs. 3.1(b) and 3.1(c), respectively, compared to those for P1 and P4 in Figs. 3.1(a) and 3.1(d), respectively. In brief, the results of Figs. 3.1 and 3.2 indicate clearly that hole transport is much more dispersive in samples P2 and P3 than in samples P1 and P4.

Table 3.1. Hole transport coefficients, kinetic parameters, and material properties derived from fitting modeling predictions to experimental data for transient photocurrent $I(t)$ in the P3HT layer samples P1, P2, P3, and P4.

Sample	P1	P2	P3	P4
P_0 ($\times 10^{25}$ m^{-3})	2.4-3.65	1.6-2.6	3.6-8.0	2.6-2.8
P_t ($\times 10^{22}$ m^{-3})	0.52-1.0	1.0-1.8	4.2-9.6	1.24-1.3
C_t ($\times 10^{-16}$ $m^3 s^{-1}$)	0.55-0.6	8-10	7.5	0.6
$P_t C_t$ ($\times 10^{6}$ s^{-1})	0.29-0.6	10-18	31.5-72	0.74-0.78
μ_0 ($\times 10^{-5}$ $cm^2 V^{-1} s^{-1}$)	6.5	0.9	0.9	3.7
γ ($\times 10^{-4}$ $(V/m)^{-1/2}$)	3.9-4.6	3.0-3.2	3.2-3.7	3.2-3.6
C_{dt} ($\times 10^{4}$ s^{-1})	1.0-2.2	10-19	20-42	1.1 -1.7
dp_t/dt ($\times 10^{25}$ m^{-3} s^{-1})	2.36-5.23	9.25-40.4	8.1-30.1	3.1-6.0

The computed fitting parameters and derived trapping rate metrics based on these parameters are listed in Table 3.1 for all four samples. The detailed determination of these parameters follows the procedure of Ref. 80. In all cases, the parameters vary over narrow ranges under different applied biases, but the trends are very clear in comparing

the various samples with respect to their hole transport dispersivity. Parameter variations with different applied bias are expected [100-102]; this is because the applied bias affects the initial free charge carrier generation from exciton dissociation and, therefore, the occupation of trap states, the trapping and detrapping rates, and the field dependence of carrier mobility. It is evident that the abilities of the different nanostructured P3HT films to generate free charges, as expressed by parameter P_0, are comparable. On the other hand, the density of trapping sites P_t varies with varying nanostructure. Sample P4 has a slightly increased value of P_t than that in P1; this value is further increased in P2 and is much higher for the thicker film P3. Comparing the P_t values of samples P2, P3, and P4, we conclude that the excess surfactant molecules surrounding P3HT nanoparticles introduce additional hole trapping sites in the organic layers, which is enhanced with increasing film thickness, and reduce the corresponding packing density. The trapping rate coefficient C_t is found to be higher by more than one order of magnitude in non-centrifuged nanoparticle assemblies (samples P2 and P3) than in the other two nanostructured films (samples P1 and P4). The resulting values of the trapping rate metric given by the product P_tC_t imply that the charge trapping effect is much (up to two orders of magnitude) stronger in non-centrifuged nanoparticle assemblies (samples P2 and P3) than in drop cast thin films and centrifuged nanoparticle assemblies (samples P1 and P4, respectively). These findings explain the similar hole transport dispersivity in samples P1 and P4 and the much more dispersive hole transport in samples P2 and P3, as observed in the results of Figs. 3.1 and 3.2. The zero-field hole mobilities are within a factor 2 in the drop cast thin film (P1) and the centrifuged nanoparticle assembly (P4). These mobility values are substantially lower in the non-centrifuged samples (P2 and P3).

The field dependence of the hole mobility, expressed by γ, is roughly the same for all the P3HT samples studied; this implies that the balancing effects between energetic and spatial disorder [103,104] do not change substantially in the different samples that we examined. However, the detrapping rate coefficient C_{dt} varies widely (over one order of magnitude) over different nanostructures; it is of comparable value in the drop cast thin film (P1) and the centrifuged nanoparticle assemblies (P4), but it is substantially higher in the non-centrifuged nanoparticle assembly samples (P2 and P3).

It is known that the stabilizing surfactants that surround the nanoparticles introduce barriers for charges to tunnel through and hop to charge transport sites in neighboring nanoparticles [105]. From the results of Table 3.1, we conclude that the presence of excess surfactant molecules in nanoparticle assemblies has led to the introduction of more defects and an increased interparticle spacing, which result in higher trapping rates and lower hole mobilities. However, these trap states are characterized by shallow trapping energy levels and low activation energy barriers so that the trapped charge carriers can be detrapped easily to contribute to free charge carriers. Upon removal of the excess surfactants in centrifuged nanoparticle assemblies, the gaps between nanoparticles in the assemblies are reduced resulting in a highly improved hole mobility. Finally, for all samples, we computed the net trapping rate dp_t/dt, defined as the difference between the trapping and detrapping rates according to Eq. (3.2) at the transit time, integrated and averaged over the layer thickness. According to this metric, it is evident that the overall hole transport dispersivities in drop cast thin films (P1) are comparable with those in centrifuged nanoparticle assemblies (P4), while they are almost one order of magnitude stronger in non-centrifuged nanoparticle assemblies (P2 and P3).

3.3.2 Analysis of Charge Transport in Semiconducting-Insulating Binary Nanoparticle Assemblies

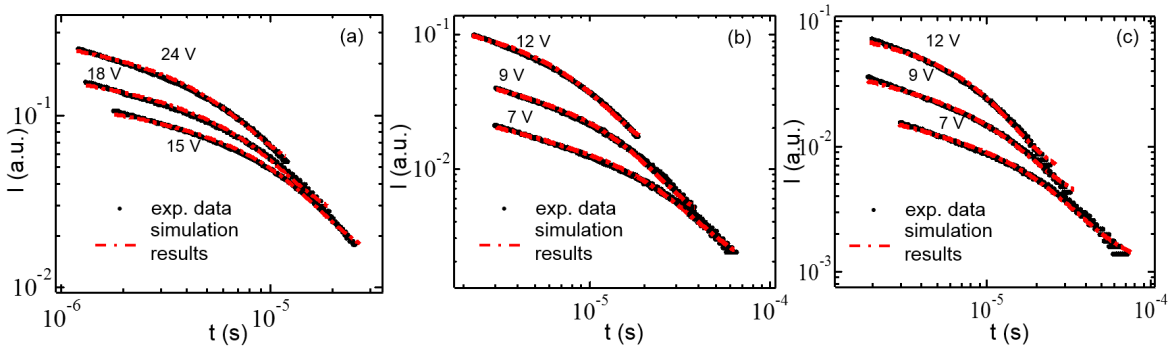

Figure 3.3. Numerical predictions of photocurrent evolution from fitting TOF experimental data in (a) P3HT centrifuged NP assemblies and binary blends of P3HT/PMMA NPs with PMMA NP diameter (b) d = 20 nm and (c) d = 80 nm.

Table 3.2. Numerical results from fitting to measured photocurrent evolution from TOF experiments on P3HT/PMMA nanoparticle assemblies. The abbreviation "Centr." is used to denote centrifuged NPs with excess surfactant molecules removed.

P3HT:PMMA	Centr. P3HT NPs	Centr. P3HT NPs + PMMA (20 nm)	Centr. P3HT NPs + PMMA (80 nm)
Free hole generation ($\times 10^{27}$ m^{-3})	1.7-1.9	1.15-2.2	1.6-2.0
Hole trapping rate ($\times 10^{6}$ s^{-1})	6.0-8.0	5.2-13.2	14.0-21.0
Hole detrapping rate ($\times 10^{5}$ s^{-1})	2.5-3.0	1.2-1.65	2.5-3
Zero-field mobility ($\times 10^{-5}$ $cm^{2}V^{-1}s^{-1}$)	2.0	0.8	0.85
Poole-Frenkel coefficient ($\times 10^{-4}$ $(V/m)^{-1/2}$)	1.0-1.7	1.1-1.3	1.2-1.5

The model of Section 3.2.1 also was used to characterize the insulating PMMA nanoparticle size effect on charge transport. We found that the variation of insulating nanoparticle size does not have major effects on hole mobility, the balance of energetic and positional disorder, or free hole generation. It mainly affects hole trapping and

detrapping kinetics. Numerical predictions of photocurrent evolution from fitting to data of TOF experiments on P3HT/PMMA NP assemblies are shown in Fig. 3.3. The numerical results for the fitting parameters are listed in Table 3.2.

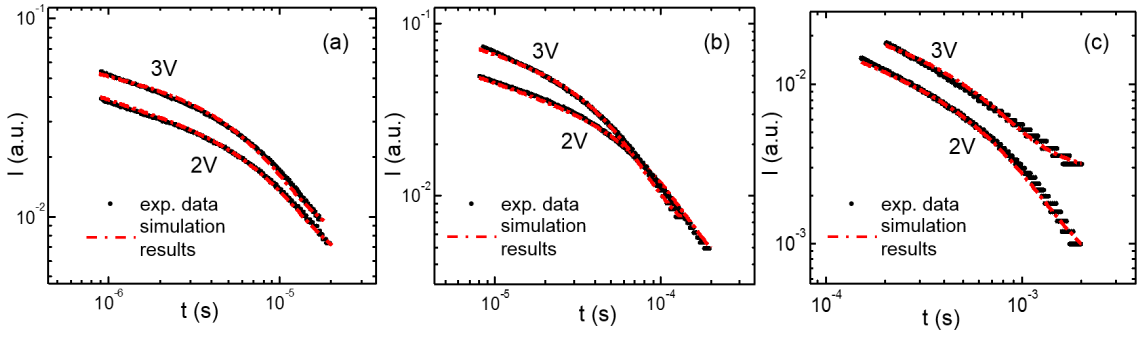

Figure 3.4. Numerical predictions of photocurrent evolution from fitting TOF experimental data in binary blends of P3HT/PS NPs with P3HT:PS NP number ratios of (a) 80:20, (b) 60:40, and (c) 40:60.

Table 3.3. Numerical results from fitting to measured photocurrent evolution from TOF experiments on P3HT/PS nanoparticle assemblies.

P3HT:PS	80:20	60:40	40:60
Charge generation ($\times 10^{26}$ m^{-3})	6-7.3	7.5-8.0	5.5-6.0
Trapping rate ($\times 10^{5}$ s^{-1})	2.75	8.4-10.5	19.5-21.5
Detrapping rate ($\times 10^{4}$ s^{-1})	3	1.5	1.0
Zero-field mobility ($\times 10^{-5}$ cm^{2} V^{-1} s^{-1})	9	1.3	0.05
Poole-Frenkel coefficient ($\times 10^{-4}$ $(V/m)^{-1/2}$)	-1.0	-1.4	-1.4

Moreover, we analyzed the effects of conducting-to-insulating nanoparticle number ratio in binary blends of P3HT/PS conducting/insulating nanoparticles. The PS nanoparticle percentage was found to affect significantly the hole mobility, as well as the hole trapping and detrapping kinetics. Numerical predictions of photocurrent evolution

from fitting TOF experimental data are shown in Fig. 3.4 with the numerical results for the fitting parameters summarized in Table 3.3.

3.3.3 Analysis of Charge Transport and Device Performance in Organic Photovoltaic Devices with Active Layers of Self-Assembled Nanospheres

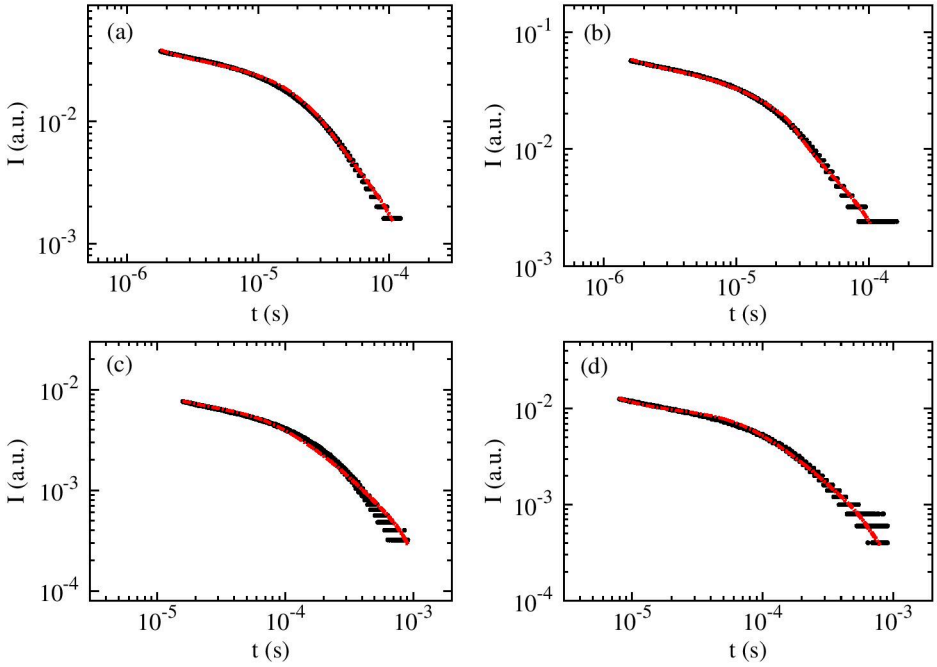

Figure 3.5. Comparison of simulation predictions (red dot-dashed lines) with experimental data (black solid circles) for photocurrent evolution $I(t)$ in devices with active layers of P3HT:PCBM blend nanoparticle assemblies under applied biases of (a) 9 V and (b) 12 V and of P3HT:PCBM separate nanoparticle assemblies under applied biases of (c) 4 V and (d) 6 V.

First, we used the transient version of our charge transport model developed in Section 3.2.2 to simulate TOF experiments and reproduce the experimental measurements. Specifically, we have fitted the predictions of our numerical simulations to the TOF experimental measurements of transient photocurrent $I(t)$ in blend and separate P3HT:PCBM nanoparticle assemblies. TOF experiments are designed to

measure charge carrier mobility by extracting the corresponding transit time and to assess charge transport dispersivity by the form of the photocurrent evolution curve. It is important to quantify this behavior and the charge carrier transport properties from the models for the two types of samples of P3HT:PCBM nanoparticle assemblies used as active layers. Figure 3.5 compares the best fits of our simulation predictions (red dot-dashed lines) with the experimental data (black solid circles) of transient photocurrents from the TOF experiments at different applied biases in log-log plots of photocurrent evolution. It is evident from the quality of the fits that the model of Eqs. (3.5)-(3.10) is very successful in reproducing the experimental data.

Table 3.4. Parameters derived from fitting modeling predictions to time-of-flight experimental measurements of transient photocurrents $I(t)$ in devices with active layers consisting of P3HT:PCBM blend and separate nanoparticle assemblies.

Sample	Blend	Separate
G_0 ($\times 10^{25}$ $m^{-3}s^{-1}$)	1.25	0.7
a_0 (nm)	1.0	1.0
k_{rec} ($\times 10^{6}$ s^{-1})	1.0	1.0
C_{bi}	0.4	0.2
μ_{n0} ($\times 10^{-7}$ $m^2V^{-1}s^{-1}$)	1.4	0.4
β_n ($\times 10^{-4}$ $(V/m)^{-1/2}$)	0.15	-1.0
μ_{p0} ($\times 10^{-8}$ $m^2V^{-1}s^{-1}$)	1.1	0.8
β_p ($\times 10^{-4}$ $(V/m)^{-1/2}$)	-5.0	-2.5
N_t ($\times 10^{21}$ m^{-3})	1.0	12
$C_{t,n}$ ($\times 10^{-17}$ m^3s^{-1})	1.0	3.4
$C_{dt,n}$ ($\times 10^{5}$ s^{-1})	1.5	0.8
P_t ($\times 10^{21}$ m^{-3})	4.0	12
$C_{t,p}$ ($\times 10^{-17}$ m^3s^{-1})	2.0	3.2
$C_{dt,p}$ ($\times 10^{5}$ s^{-1})	1.2	1.6

The resulting fitting parameters are listed in Table 3.4. The detailed determination of these fitting parameters follows the procedures outlined in Ref. 80. In both types of NP assemblies, electron and hole zero-field mobilities are comparable to those in BHJs, respectively [74,80]. Charge transport between NPs does not actually constitute a limiting factor for charge transport in the active layer when excess NP stabilizing surfactant molecules are removed as done in centrifuged NP assemblies [61]. Moreover, strong van der Waals interactions between NPs dislodge the remaining stabilizing surfactant molecules, which are weakly bound to the organic nanoparticles, leading to direct particle-particle contact and efficient charge transport [61,62]. Both electron and hole zero-field mobilities are higher in blend NP assemblies than in separate NP assemblies. We attribute this to that in blend NP assemblies, it is likely that the hopping distances for electron and hole transport are shorter and the corresponding barriers are lower due to the existence of both electron and hole transport materials in the individual nanoparticles of the assembly. In both samples, the field dependence coefficients of electron and hole mobilities are weak or negative, in good agreement with the experimental measurements [61]. The field dependence can be expressed mathematically by the Poole-Frenkel relation proposed by Bässler [106],

$$\mu(T,E) = \mu_0 \exp\left(-\frac{2}{3}\hat{\sigma}\right) \exp\left(C\left(\hat{\sigma}^2 - \Sigma^2\right)E^{1/2}\right), \tag{3.13}$$

where $\hat{\sigma} = \sigma/(k_B T)$ and Σ are parameters that characterize the energetic and positional disorder, respectively, and $C > 0$ is a fitting parameter. In the blend and separate NP assemblies examined here, positional disorder is comparable with, or higher than, the energetic disorder, which leads to the observed weak or negative field dependence coefficients. Electron and hole trap densities, as well as trapping and detrapping rate

coefficients for each charge carrier are comparable within each sample. However, it is evident that layers consisting of separate NP assemblies have higher trap densities than those consisting of blend NP assemblies. The differences in charge carrier trap densities of blend and separate NP assemblies result from their respective charge transport pathway lengths. The existence of both electron and hole transporting materials in the individual nanoparticles of blend NP assemblies facilitates continuous charge transport pathways with shorter charge hopping distances. On the contrary, in separate NP assemblies with pristine P3HT or PCBM NPs [61], finding a continuous pathway for charge transport through either the donor or the acceptor phase is likely to result in longer and more tortuous pathways for charge hopping. Both material defects and surfactant molecules surrounding each NP act as trapping sites for charge transport. Therefore, in separate NP assemblies, the longer pathways for continuous charge hopping result in higher trap densities in these assemblies along the free carrier transporting paths. For electron trapping, the trapping rate coefficient in blend NP assemblies is lower than that in separate NP assemblies, while the electron detrapping rate coefficient in blend NP assemblies is higher than that in separate NP assemblies, implying that the electron trap energy level is shallower in the sample consisting of blend NP assemblies. For hole trapping, the trapping rate coefficient in blend NP assemblies is lower than that in separate NP assemblies, but the detrapping rate coefficients are comparable in the two samples. We find that the free charge generation rate is higher in blend NP than in separate NP assemblies, but the difference between the generation rates in the two samples is not significant (less than a factor of 2). We also find that the electron-hole pair separation distance in the bound charge pair and the geminate recombination rate

coefficient are the same in both samples of NP assemblies. Finally, we find that the ratio of the actual bimolecular recombination rate over that predicted by Langevin theory is smaller (by a factor of 2) in separate NP assemblies than that in blend NP assemblies. One of the assumptions of the Langevin theory for bimolecular charge carrier recombination is that charge carrier transport is homogeneous within the active layer. Charge transport pathways in blend NP assemblies are more uniformly distributed within the active layer than those in separate NP assemblies [61]. Consequently, the deviation of the actual bimolecular recombination rate from the prediction of Langevin theory in blend NP assemblies is expected to be smaller than that in separate NP assemblies, consistent with our finding that the coefficient C_{bi} in blend NP assemblies is closer to 1 than that in separate NP assemblies. Moreover, the larger donor/acceptor interfacial area available in blend NP assemblies, due to the existence of such interfacial regions within each NP in such assemblies, explains that the bimolecular recombination rate in blend NP assemblies is higher than that in separate NP assemblies. Overall, our analysis of the simulations of TOF experiments shows that charge transport in blend NP assemblies is characterized by higher zero-field mobilities and fewer defects acting as traps for charge carriers than those of separate NP assemblies.

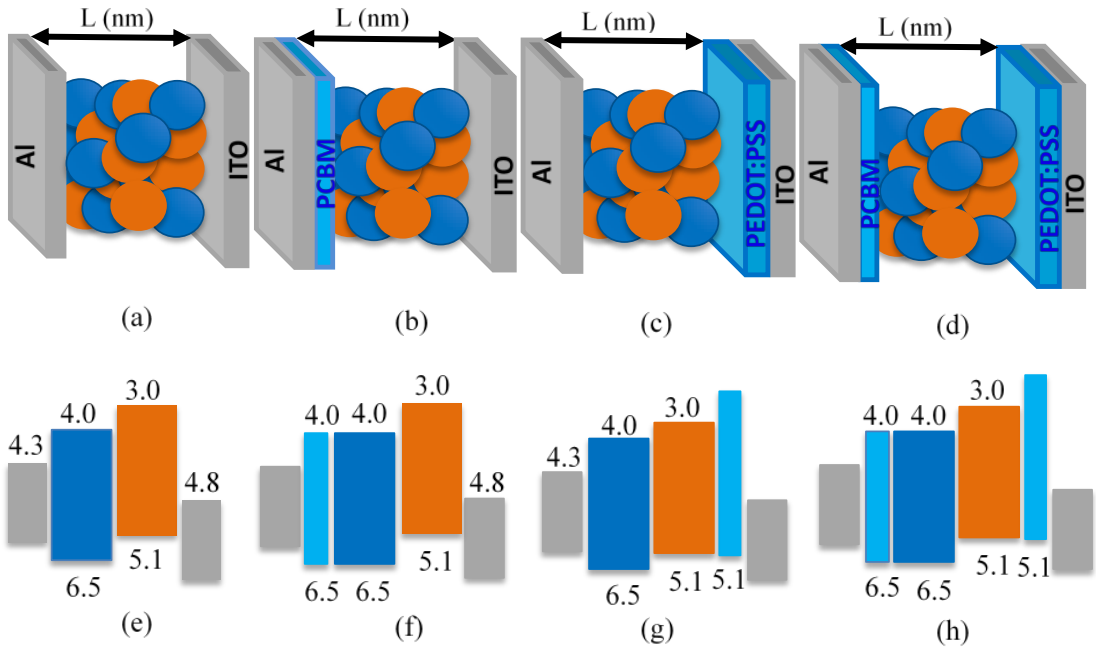

Figure 3.6. Schematic representation of structures for devices with active layers of P3HT:PCBM nanoparticle assemblies (a) with no interlayers, (b) with a PCBM interlayer next to the Al electrode, (c) with a PEDOT:PSS interlayer next to the ITO electrode, and (d) with both PCBM and PEDOT:PSS interlayers next to the respective electrodes. In all cases, separate nanoparticle assemblies are chosen as the active layer morphology. Blue and orange spheres are used to represent PCBM and P3HT nanoparticles, respectively. The energy band diagram schematics shown in (e), (f), (g), and (h) are for the devices shown in (a), (b), (c), and (d), respectively. The colors in the band diagrams are consistent with those in the device schematics with light blue and silver representing the interlayers and the electrodes, respectively, and the numbers refer to the corresponding energy levels in eV.

Before using the model predictions to reproduce the experimental J-V characteristics, we investigate how the important aspects of device structures other than the nanostructure and morphology of the active layer, namely, the existence and type of different interlayers between the active layer and the two electrodes, in the experiments affect the J-V characteristics and, thus, the device PCE. Figure 3.6 gives a schematic representation of four types of device structures with the corresponding energy band diagrams. In these schematics, we choose to use separate NP assemblies as the active

layer morphology. In Fig. 3.6(a), the active layer is sandwiched between Al and ITO electrodes without using any interlayers. This is the same device structure used in the TOF experiments. The corresponding band energies, which were used in the simulation of the TOF experiments that yielded the results of Fig. 3.5 and Table 3.4, are depicted in Fig. 3.6(e). Figure 3.6(b) shows a device where a thin PCBM buffer layer is placed between the Al cathode and the active layer. PCBM has a much lower HOMO energy level than that of P3HT and, with the PCBM layer being placed between the Al electrode and the active layer, the contact of P3HT nanoparticles with the Al surface is ruled out. Therefore, the PCBM interlayer acts as a hole blocking layer at the active layer/cathode interface. Moreover, it forms an Ohmic contact for electron extraction, as shown in Fig. 3.6(f). In the device of Fig. 3.6(c), a UV-O_3 treated PEDOT:PSS layer is placed between the ITO anode and the active layer. The PEDOT:PSS layer acts as an electron blocking layer at the active layer/anode interface due to its high LUMO level, as shown in Fig. 3.6(g). UV-O_3 treatment has been demonstrated to modify the PEDOT:PSS HOMO energy level [107,108] and form an Ohmic contact for hole extraction in this case [65]. In the device of Fig. 3.6(d), both interlayers are introduced and, hence, electron and hole blocking effects and Ohmic contacts for charge carrier extraction are all included in this device structure, as shown in Fig. 3.6(h). The device structure employed for the experimental measurements of J-V curves is the same as that of Fig. 3.6(d).

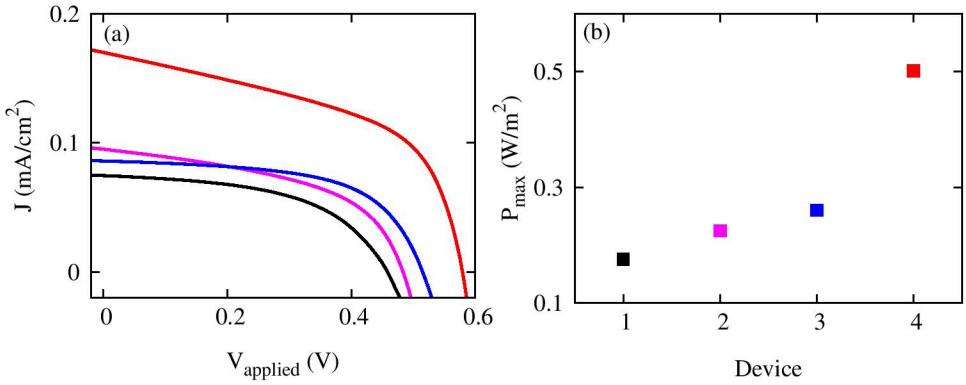

Figure 3.7. Modeling predictions of (a) J-V curves and (b) maximum power output, P_{max}, for OPV devices with active layers consisting of P3HT:PCBM nanoparticle assemblies with no interlayers [black continuous line in (a) and solid square in (b)], with a PCBM interlayer next to the Al electrode [magenta continuous line in (a) and solid square in (b)], with a PEDOT:PSS interlayer next to the ITO electrode [blue continuous line in (a) and solid square in (b)], and with PCBM and PEDOT:PSS interlayers next to the respective electrodes [red continuous line in (a) and solid square in (b)].

The major effects of the interlayers introduced in the device structure are to modify the boundary conditions for Eqs. (3.5) and (3.7) and the built-in potential V_{bi} for the device. When a selective interlayer is placed between the electrode and the active layer, the flux of the blocked charge carrier into the active layer at that interface ($x = 0$ or $x = L$) is equal to zero, i.e., $-D_n\partial n_f/\partial x - \mu_n n_f E = 0$ or $-D_p\partial p_f/\partial x + \mu_p p_f E = 0$. Depending on the position of the Ohmic contact, we modify the boundary condition as $n_f(0) = N_c$ or $p_f(L) = N_c$, where N_c is the effective density of states of both the conduction and the valence band [74]. The built-in potential V_{bi} is important in determining the open-circuit voltage V_{OC}. For the device structure of Fig. 3.6(a), which is similar to that of a metal-insulator-metal (MIM) model, V_{bi} is equal to the difference in the work function of the two metal electrodes. In the cases of Figs. 3.6(b)-3.6(d), where an Ohmic contact is formed due to the introduction of an interlayer, band bending at the Ohmic contact increases V_{bi} and is expected to result in an increase in V_{OC} [109].

In Fig. 3.7, we compare the J-V characteristics and the device maximum power output, P_{max}, for the four device structures of Figs. 3.6(a)-3.6(d). The device maximum power output is expressed as $P_{max} = V_{OC}J_{SC}FF$, where FF is the device fill factor. The active layer thickness L is set to be 200 nm and N_c is chosen to be 1×10^{23} m^{-3}. The rest of the parameters we used in the computation of the J-V curves for steady device operation are from Table 3.4 for active layers consisting of blend nanoparticle assemblies. The black, magenta, blue, and red solid lines in Fig. 3.7(a) and solid squares in Fig. 3.7(b) correspond to the J-V curves and P_{max} values for the devices with the structures of Fig. 3.6(a), 3.6(b), 3.6(c), and 3.6(d), respectively. The improvements in V_{OC} for all three devices in Figs. 3.6(b)-3.6(d) compared to that in Fig. 3.6(a) are due to the change from Schottky contacts to Ohmic contacts due to the introduction of the corresponding interlayers, which leads to an increase in V_{bi} and, thus, in V_{OC}. Charge extraction barrier lowering in conjunction with the selectivity (carrier blocking) of the interlayers also result in increases in J_{SC}, which becomes particularly significant with the use of both interlayers in the structure of Fig. 3.6(d). Moreover, it is interesting to note that the use of the interlayer in Fig. 3.6(b) results in a higher increase in J_{SC} than that of the interlayer in Fig. 3.6(c), while the use of the interlayer in Fig. 3.6(c) results in a higher increase in V_{OC} than that of the interlayer in Fig. 3.6(b). When both interlayers are introduced into the device structure, the device maximum power output is almost three times higher than that of the device with no interlayers. Although the device maximum power output is low due to the low input of free charge generation rates under a 355-nm laser pulse, the model predictions explain the important roles in the device performance

played by the functional interlayers and provide guidelines for OPV device layout design for further efficiency improvement.

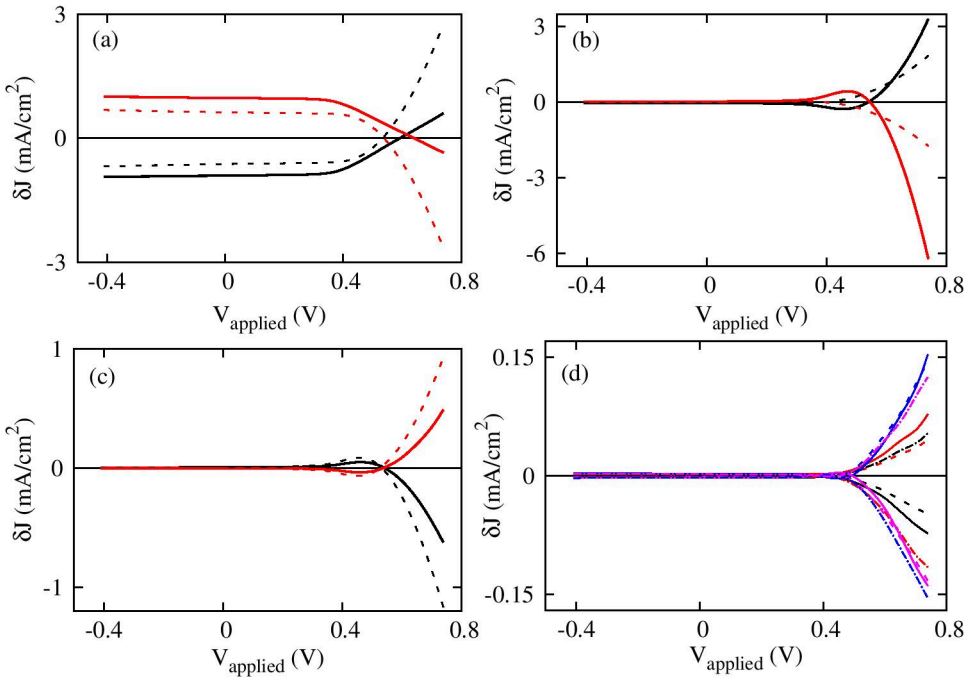

Figure 3.8. Results of sensitivity analysis through systematic parametric study for the computed J-V characteristics of OPV devices with active layers consisting of P3HT:PCBM nanoparticle assemblies with electron and hole blocking layers and Ohmic contacts. The parameters varied are (a) effective density of states N_c (red and black solid lines) and zero-field electron mobility μ_{n0} (red and black dashed lines), (b) electron-hole pair separation distance a_0 (red and black solid lines) and zero-field hole mobility μ_{p0} (red and black dashed lines), (c) geminate recombination rate coefficient k_{rec} (red and black solid lines) and bimolecular recombination prefactor C_{bi} (red and black dashed lines), and (d) electron trap density N_t (red and black solid lines) and hole trap density P_t (magenta and blue solid lines), electron trapping rate coefficient $C_{t,n}$ (red and black dashed lines) and hole trapping rate coefficient $C_{t,p}$ (magenta and blue dashed lines), and electron detrapping rate coefficient $C_{dt,n}$ (red and black dot-dashed lines) and hole detrapping rate coefficient $C_{dt,p}$ (magenta and blue dot-dashed lines). In all cases, the results shown correspond to parametric variations of +15% and -15%, respectively.

Before fitting the model predictions to the experimental J-V measurements under steady light exposure to characterize the influence of nanoparticle size and ratio in OPV device performance, we carried out a sensitivity analysis of the input model parameters

on the predicted J-V relations for a device with the same structure as that shown in Fig. 3.6(d). The objective of this sensitivity analysis is to eliminate as many fitting parameters as possible from the analysis of the measured J-V characteristics of the OPV devices examined under steady illumination; reducing the number of model parameters involved in the J-V data analysis will strengthen the physical meaning of the obtained remaining fitting parameters and provide clear interpretations of the experimental data regarding the role of nanoparticle size and ratio in the NP assemblies that constitute the devices' active layers. In this study, limiting the number of fitting parameters in the analysis of steady-state J-V data is enabled by the availability of transient photocurrent evolution data from the TOF experiments and highlights the importance of employing multiple types of experiments toward a fundamental understanding of the charge transport processes that govern OPV device performance. First, a referenced J-V curve was computed for a reference parameter set. We then varied each of the examined parameters by ±15% of its referenced value, while keeping all the other parameters at their referenced values, and computed the resultant J-V curves. The referenced photocurrent was subtracted from the new photocurrent to obtain the difference δJ. In Fig. 3.8, we plot δJ as a function of V to study the effect on the device J-V characteristics of the variation of each input parameter. It is evident from this parameter sensitivity analysis that the effects of varying the effective density of states N_c and the zero-field electron mobility μ_{n0}, shown in Fig. 3.8(a), are qualitatively different from those of varying the other model parameters that are demonstrated in Figs. 3.8(b)-3.8(d). The variations of the parameters examined in Figs. 3.8(b)-3.8(d) influence the predicted J-V relation at medium to high voltages, while varying N_c and μ_{n0} have additional effects

under reverse voltage operation and at lower to medium voltages. Increasing the effective density of states N_c and the zero-field electron mobility μ_{n0} leads to improvement (increase) in the short-circuit current density J_{SC}. However, an increase in the zero-field hole mobility μ_{p0} does not have a substantial effect on J_{SC}, as shown in Fig. 3.8(b). Increasing the electron-hole pair separation distance a_0, shown in Fig. 3.8(b), and decreasing the germinate recombination rate coefficient k_{rec} and bimolecular recombination prefactor C_{bi}, shown in Fig. 3.8(c), have similar effects. All of these parameter variations lead to an increase in photocurrent near the open-circuit voltage in the first quadrant and a decrease in photocurrent in the fourth quadrant. These trends cause an increase of the squareness (i.e., similarity to a rectangular shape) of the J-V curve and result in increases in the device's fill factor. Figure 3.8(d) shows the influence of varying the electron and hole trap densities in the active layer and the corresponding trapping and detrapping rate coefficients. The effects of varying these parameters on the resulting photocurrent are weaker by around one order of magnitude than those of varying the other parameters examined. Therefore, to reduce the complexity of fitting the model predictions to the J-V experimental data under steady illumination and to investigate the effects of nanoparticle size and ratio on the key device performance metrics, we keep the values of the electron and hole trap densities and the electron and hole trapping and detrapping rate coefficients the same as those obtained from the simulation of the TOF experiments (listed in Table 3.4) in the parameterization of our charge transport model in the rest of our analysis for both types of nanoparticle assemblies.

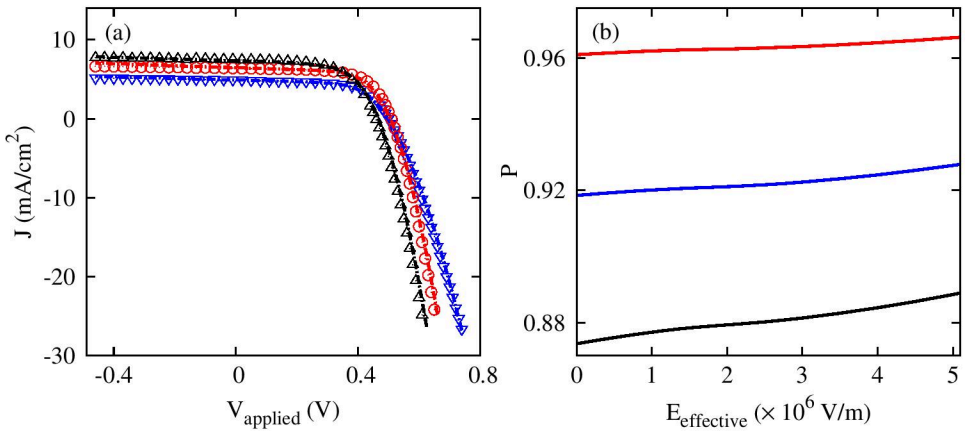

Figure 3.9. (a) Best fits of simulation predictions (solid lines) to experimental measurements (open symbols) of J-V curves for devices with active layer morphology of P3HT:PCBM blend nanoparticle assemblies with nanoparticle sizes of 70 nm (blue), 80 nm (red), and 115 nm (black). (b) Computed charge generation efficiency for the three devices in (a) with nanoparticle sizes of 70 nm (blue), 80 nm (red), and 115 nm (black).

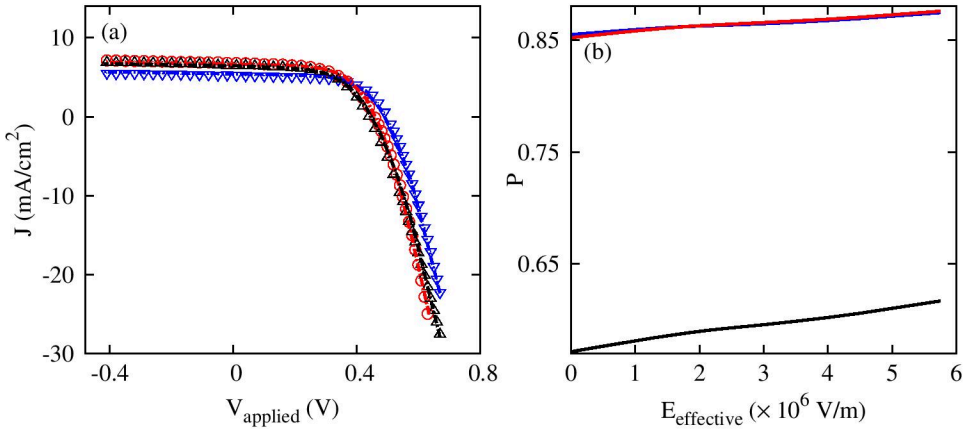

Figure 3.10. (a) Best fits of simulation predictions (solid lines) to experimental measurements (open symbols) of J-V curves for devices with active layer morphology of P3HT:PCBM separate nanoparticle assemblies with nanoparticle sizes of 70 nm (blue), 80 nm (red), and 115 nm (black). (b) Computed charge generation efficiency for the three devices in (a) with nanoparticle sizes of 70 nm (blue), 80 nm (red), and 115 nm (black).

With this model parameterization, we have fitted the model predictions to the experimental J-V curve measurements in devices with active layers consisting of blend

and separate nanoparticle assemblies. The active layer thickness is equal to 200 nm in all devices examined. Figures 3.9(a) and 3.10(a) compare simulation results with experimental data for J-V curves in devices with active layers of blend and separate nanoparticle assemblies, respectively, with P3HT:PCBM nanoparticle sizes of 70 nm, 80 nm, and 115 nm. The computed fitting parameters and device performance metrics are listed in Tables 3.5 and 3.6, respectively. In both types of NP assemblies, we observe an increase in the charge generation rate as the nanoparticle size increases. It is likely that for active layers of the same thickness, the layer with a larger nanoparticle size imposes a smaller number of energy barriers that photons have to overcome in order to reach the same depth in the layer and, therefore, results in more photons available to be absorbed and converted to electron-hole pairs at that depth. As for the electron-hole pair separation distance in blend NP assemblies, it is smallest in the sample of 70-nm nanoparticle size (i.e., the smallest NP size examined). Increasing the nanoparticle size beyond 80 nm does not have an effect on the electron-hole pair separation distance for the active layer. However, in separate NP assemblies, this electron-hole pair separation distance does not change with varying the nanoparticle size. In blend NP assemblies, both donors and acceptors are confined in the same nanoparticle. A larger nanoparticle size increases the distance between the electron and the hole in the bound charge pairs and allows for better separation of these electron-hole pairs. On the other hand, in separate NP assemblies, donors and acceptors are confined in different nanoparticles and each domain size is large enough so that the electron-hole pair separation distance is not influenced by the nanoparticle size. The effects of nanoparticle size on the effective density of states, built-in voltage, and geminate recombination rate are the same for blend

and separate nanoparticle assemblies. The effective densities of states of both the conduction and the valence bands are not affected by nanoparticle size. This is because the composition of the active layer and, thus, the energy band alignment for the device are the same at all nanoparticle sizes. Therefore, V_{bi} remains the same for all three samples in both blend and separate NP assemblies. The geminate recombination rate coefficient is higher in both types of assemblies at the highest nanoparticle size of 115 nm. For blend NP assemblies, the bimolecular recombination prefactor is lower in the sample with nanoparticle size of 80 nm, while in separate NP assemblies, this prefactor increases with the nanoparticle size. As the nanoparticle size increases, the zero-field electron mobility increases slightly in blend NP assemblies while it decreases also slightly in separate NP assemblies. However, varying nanoparticle size has a much more pronounced effect on the zero-field hole mobility. Specifically, in both types of NP assemblies, the zero-field hole mobility increases by a factor of approximately 4 when the nanoparticle size is increased from 70 nm to 115 nm. The field dependence coefficients of the electron and hole mobilities are all weak or negative in all of the samples examined due to the nature of the active layers as mentioned above.

Table 3.5. Parameters derived from fitting modeling predictions to J-V curve measurements, as well as resulting computed performance metrics, in devices with active layer morphology of P3HT:PCBM blend nanoparticle assemblies with different nanoparticle sizes.

Nanoparticle size (nm)	70	80	115
G_0 ($\times 10^{26}$ $m^{-3}s^{-1}$)	1.0	1.5	3.5
N_c ($\times 10^{24}$ m^{-3})	1.5	1.5	1.5
a_0 (nm)	1.35	1.45	1.45
k_{rec} ($\times 10^{6}$ s^{-1})	1.0	1.0	3.0
C_{bi}	0.3	0.2	0.3
μ_{n0} ($\times 10^{-7}$ $m^2V^{-1}s^{-1}$)	1.92	2.32	2.4
β_n ($\times 10^{-5}$ $(V/m)^{-1/2}$)	1.5	3.0	-8.0
μ_{p0} ($\times 10^{-8}$ $m^2V^{-1}s^{-1}$)	2.7	3.2	11
β_p ($\times 10^{-4}$ $(V/m)^{-1/2}$)	-5.0	-3.5	-2.5
V_{bi} (V)	0.74	0.74	0.74
FF (%)	63.5	66.2	57.6
PCE (%)	1.56	2.15	2.06

The corresponding device performance metrics, fill factor and power conversion efficiency, are calculated for each sample under consideration and agree well with the experimental values. In blend NP assemblies, the sample with nanoparticle size of 80 nm has the highest PCE of 2.15%, while the sample with nanoparticle size of 115 nm also has a high efficiency of over 2%. The higher free charge carrier generation rate in these two samples, as well as the longer electron-hole pair separation distance are major contributing factors to increasing the PCE of the devices with these active layers over 2%. Nevertheless, the PCE of the device with the sample of 115 nm nanoparticle size is decreased slightly because of its higher geminate recombination rate coefficient. In devices with active layers of separate NP assemblies, the PCE of the device with active

layer of 80-nm nanoparticle size also is the highest. For the other two devices, the performance is reduced due to the lower free charge generation rate in that with the active layer of 70-nm nanoparticle size and due to the higher geminate and bimolecular recombination rates in that with the active layer of 115-nm nanoparticle size.

Table 3.6. Parameters derived from fitting modeling predictions to J-V curve measurements, as well as resulting computed performance metrics, in devices with active layer morphology of P3HT:PCBM separate nanoparticle assemblies with P3HT:PCBM nanoparticle ratio of 1:1 and different nanoparticle sizes.

Nanoparticle size (nm)	70	80	115
G_0 ($\times 10^{26}$ $m^{-3}s^{-1}$)	1.5	3.0	3.5
N_c ($\times 10^{24}$ m^{-3})	1.8	1.8	1.8
a_0 (nm)	1.28	1.28	1.28
k_{rec} ($\times 10^{6}$ s^{-1})	1.0	1.0	4.0
C_{bi}	0.1	0.19	0.3
μ_{n0} ($\times 10^{-7}$ $m^2V^{-1}s^{-1}$)	1.9	1.84	1.76
β_n ($\times 10^{-4}$ $(V/m)^{-1/2}$)	-1.0	-2.0	-3.3
μ_{p0} ($\times 10^{-8}$ $m^2V^{-1}s^{-1}$)	2.5	8.0	11.0
β_p ($\times 10^{-4}$ $(V/m)^{-1/2}$)	-2.0	-1.0	-1.0
V_{bi} (V)	0.73	0.73	0.73
FF (%)	63.2	57.2	57.6
PCE (%)	1.66	1.78	1.64

In addition to reproducing the experimental J-V curves, we calculated the charge generation efficiency P for all the samples examined at T = 300 K over a wide range of the effective electric field by integrating the local charge generation probability over the active layer thickness according to the equation

$$P(T,E) = N_F \int_0^L p(x,T,E) f(a_0,x) \mathrm{d}x, \tag{3.14}$$

where $N_F = 4/(\pi^{0.5}a_0^{\ 3})$ is a normalization factor, $p(x,T,E) = k_{diss}/(k_{diss} + k_{rec})$ is the local generation probability, and $f(a_0,x) = x^2\exp(-x^2/a_0^{\ 2})$ is a distribution function of donor-acceptor separation, which takes into account the spatial disorder of conjugated polymer/fullerene photovoltaic material systems [74]. This charge generation efficiency expresses the probability of charge pairs to dissociate against decaying to their ground state. This computed probability also provides a metric of device performance. Figures 3.9(b) and 3.10(b) show the calculated P in devices with active layers of blend and separate nanoparticle assemblies, respectively, with different nanoparticle sizes. In blend NP assemblies, the charge generation efficiency is the highest in the sample with a NP size of 80 nm and the lowest in that with a NP size of 115 nm. In separate NP assemblies, this efficiency P is almost the same for the two samples with NP sizes of 70 nm and 80 nm and is the lowest in that with NP size of 115 nm. In both types of NP assemblies, Eq. (3.14) predicts the highest charge generation efficiency for the device with the highest PCE. It is evident that the mismatch in the electron and hole mobilities in these samples does not impede charge generation efficiency. In fact, due to the energetic disorder in organic photovoltaic materials, the electron and hole mobility mismatch almost does not affect the charge separation probability [110]. However, the calculated charge generation efficiency fails in predicting the second highest device PCE in blend NP assemblies with NP size of 115 nm and the similar device PCE in separate NP assemblies with NP sizes of 70 nm and 115 nm. This limitation is due to the assumption of homogeneous geminate recombination rate and the simplifications of Onsager-Braun theory in describing charge dissociation rate [82,111]. Regardless of all

of these simplifications, however, Eq. (3.14) and Onsager-Braun theory are still widely applied to explain experimental observations and to evaluate the device efficiency.

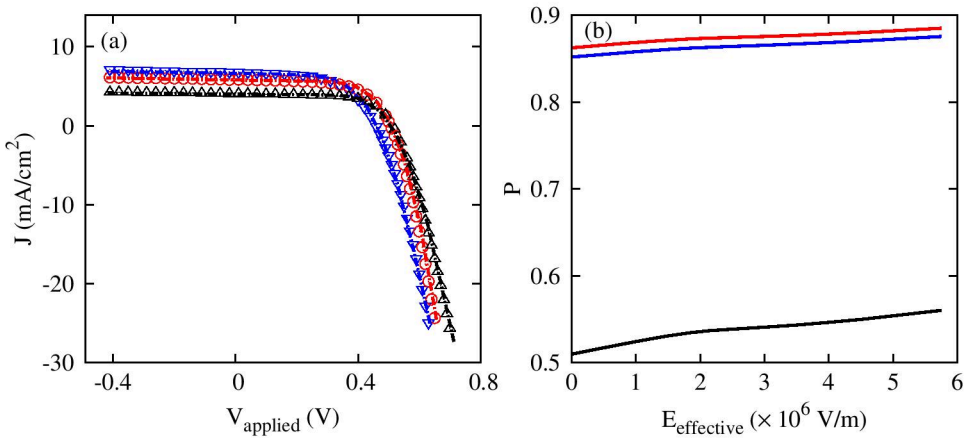

Figure 3.11. (a) Best fits of simulation predictions (solid lines) to experimental measurements (open symbols) of J-V curves for devices with active layer morphology of P3HT:PCBM separate nanoparticle assemblies with P3HT:PCBM nanoparticle ratios of 1:1 (blue), 2:1 (red), and 4:1 (black). (b) Computed charge generation efficiency for the three devices in (a) with nanoparticle ratios of 1:1 (blue), 2:1 (red), and 4:1 (black).

Finally, we studied the effect of the P3HT:PCBM nanoparticle ratio in separate nanoparticle assemblies. Figure 3.11(a) compares the simulation results with experimental J-V curves for three samples with P3HT:PCBM nanoparticle ratio of 1:1, 2:1, and 4:1, respectively. The computed fitting parameters and device performance metrics for the devices with these active layers are listed in Table 3.7. We find that the free charge carrier generation rate decreases as the percentage of P3HT nanoparticles in the assembly increases. In such assemblies, it might be expected that the imbalance of the donor and acceptor materials that decreases their interfacial contact area would reduce the initial electron-hole pair separation. It would take longer for the generated charge pairs to diffuse to the interface which, therefore, would increase their probability of decaying to their ground states. On the contrary, we find that varying the nanoparticle

ratio does not affect the electron-hole pair separation distance. We also find that the effective density of states is influenced by the active layer composition variation. It increases with increasing nanoparticle ratio and so does the built-in voltage. The geminate recombination rate coefficient is not affected by increasing the nanoparticle ratio from 1:1 to 2:1, but it increases by a factor of 4 when the nanoparticle ratio reaches a value of 4:1. Also, we find that increasing the nanoparticle ratio reduces the bimolecular recombination rate to a further extent compared to the Langevin theory prediction. This is due to the reduced interfacial area between chemically different nanoparticles, which decreases the probability for electrons and holes to approach within their recombination distance. As expected, the zero-field electron mobility decreases with increasing nanoparticle ratio, but, surprisingly, the values of zero-field hole mobility is lower in the active layers with higher P3HT content. The field dependence coefficients of the electron and hole mobilities in all samples are found to be negative. Device FFs and PCEs are computed for the devices with active layers consisting of the three samples with different nanoparticle ratios. The combination of all the effects described so far results in the highest PCE for the device with P3HT:PCBM nanoparticle ratio of 2:1. A further increase of P3HT NPs results in a significant decrease in the free charge carrier generation rate and increase in the geminate recombination rate, which ultimately causes a reduction in the device PCE. The calculated charge generation efficiencies, according to Eq. (3.14), are plotted in Fig. 3.11(b) for the three devices examined. The charge generation efficiency is the highest in the device with active layer having a nanoparticle ratio of 2:1 and lowest in that with a nanoparticle ratio of 4:1. This prediction captures

fully the effect of nanoparticle ratio on the device power conversion efficiency in such devices.

Table 3.7. Parameters derived from fitting modeling predictions to J-V curve measurements, as well as resulting computed performance metrics, in devices with active layer morphology of P3HT:PCBM separate nanoparticle assemblies with nanoparticle size of 80 nm and different P3HT:PCBM nanoparticle ratios.

Nanoparticle ratio	1:1	2:1	4:1
G_0 ($\times 10^{26}$ $m^{-3}s^{-1}$)	3.0	1.0	0.6
N_c ($\times 10^{24}$ m^{-3})	1.8	1.9	2.1
a_0 (nm)	1.28	1.28	1.28
k_{rec} ($\times 10^{6}$ s^{-1})	1.0	1.0	4.0
C_{bi}	0.19	0.08	0.08
μ_{n0} ($\times 10^{-7}$ $m^2V^{-1}s^{-1}$)	1.84	1.8	1.08
β_n ($\times 10^{-4}$ $(V/m)^{-1/2}$)	-2.0	-1.0	-2.0
μ_{p0} ($\times 10^{-8}$ $m^2V^{-1}s^{-1}$)	8.0	4.0	6.0
β_p ($\times 10^{-4}$ $(V/m)^{-1/2}$)	-1.0	-1.0	-1.0
V_{bi} (V)	0.73	0.755	0.773
FF (%)	57.2	62.4	66.3
PCE (%)	1.78	1.84	1.38

3.3.4 Optimization of Organic Photovoltaic Device Performance

To further optimize the device performance, we analyzed further the device that exhibited the best performance among those that we examined, i.e., the device with an active layer of blend nanoparticle assemblies with nanoparticle size of 80 nm, to investigate the effects of the active layer thickness on device performance. Exciton generation rate (X_0) is highly affected by the active layer thickness and can be predicted by the well-developed transfer matrix method [112]. The thicknesses of the layers for the

relevant device structure of Al/Ca/PCBM/P3HT:PCBM/PEDOT:PSS/ITO/glass under consideration are 100/15/50/L/40/110/10^6 (in nm), where L is the thickness of the active layer consisting of P3HT:PCBM blend nanoparticle assemblies ranging from 80 nm, which consists of a single layer of assembled nanoparticles, to 320 nm, which consists of 4 nanoparticle layers. The complex refractive indices of the materials Al, Ca, PEDOT:PSS, PCBM, ITO, and glass layers involved in this device structure are taken from the literature [113,114]. For the active layer of P3HT:PCBM blend nanoparticle assemblies, the extinction coefficient κ (imaginary part of the complex index of refraction) is calculated from the measured absorption coefficient α according to the relation $\alpha = 4\pi\kappa/\lambda$, where λ is the wavelength of light ranging from λ_1 = 300 nm to λ_2 = 800 nm, and the refractive index is approximated using values from Ref. 113. The average exciton generation rate is calculated according to the expression

$$X_0 = \frac{1}{L}\int_0^L \int_{\lambda_1}^{\lambda_2} \frac{\lambda}{hc} Q(x,\lambda)\,\mathrm{d}\lambda\,\mathrm{d}x, \tag{3.15}$$

where h is Planck's constant, c is the speed of light, and $Q(x, \lambda)$ is the time average of the energy dissipated per second at position x [112]. X_0 is then normalized with respect to its value at L = 200 nm. The predicted $X_{0,\text{normalized}}$ as a function of L is shown in Fig. 3.12. The average exciton generation rate first increases as the active layer thickness increases from 80 nm to 135 nm, followed by a relatively sharp decrease with L increasing from 135 nm to 225 nm, and then decreases further but less abruptly with L increasing from 225 nm to 320 nm. Overall, the exciton generation rate peaks at an active layer thickness around L = 140 nm.

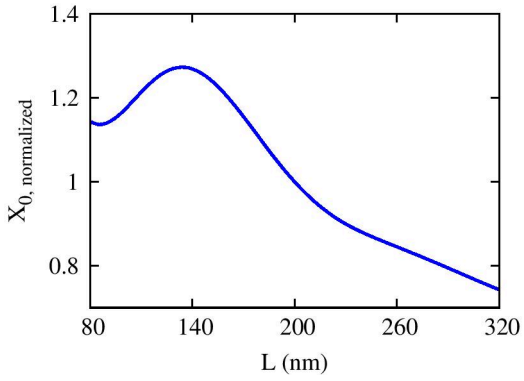

Figure 3.12. Normalized exciton generation rate in P3HT:PCBM blend nanoparticle assemblies with nanoparticle size of 80 nm as a function of the active layer thickness, L, over the range 80 nm $\leq L \leq$ 320 nm. The exciton generation rate is normalized with respect to its value at L = 200 nm.

To compute the device performance at different active layer thicknesses, we applied again our charge transport model of Eqs. (3.5)-(3.10) and varied L over the range from 80 to 320 nm. For the free charge generation rate G_0, we used the predicted normalized exciton generation rate profile in Fig. 3.12 and the fitted value of G_0 at L = 200 nm to calculate the corresponding values at the other active layer thicknesses. Furthermore, the bimolecular and geminate recombination rate coefficients are highly likely to change from the values of the corresponding fitting parameters in Table 3.5 as L varies [115,116]. For a thinner active layer, there are shorter pathways for charge transport. It is reasonable to expect lower recombination rates for thinner layers and vice versa. Dastoor et al. suggested a linear relationship between the recombination efficiency and L when blocking layers exist at both electrodes [115]. Following this linear dependence, for a qualitative exploration of active layer thickness effects on device performance, we have varied both C_{bi} and k_{rec} by ±5%, ±10%, and ±15%, respectively, of their values at L = 200 nm, when increasing (+) or decreasing (-) L from 200 nm in

increments of 30 nm. Since the internal structure of the individual nanoparticles and the composition of the active layer do not change, all the other input parameters are kept constant as L varies at the values listed in Table 3.5 for the sample of 80-nm nanoparticle size. Figure 3.13 shows the computed V_{OC}, J_{SC}, FF, and PCE for all three cases (5, 10, and 15%) of parameter variation described above. For V_{OC}, it is evident that variations of C_{bi} and k_{rec} have the strongest influence at $L \leq 140$ nm. For all parameter values examined in the recombination rate coefficients, V_{OC} decreases initially and then increases as L increases. Overall, variations of C_{bi} and k_{rec} by 15% over 30 nm of layer thickness results in the highest open-circuit voltage over the examined active layer thickness. For J_{SC}, the variations of C_{bi} and k_{rec} examined have minimal effects except for $L \geq 260$ nm, with the observed differences due to these parameter variations remaining very small even at those thicker layers. J_{SC} decreases monotonically with increasing L until $L \geq 290$ nm, beyond which J_{SC} exhibits a slight increase. The fill factor is maximized at $L = 140$ nm (where the exciton generation rate is maximized) in all cases. As for the device PCE, it exhibits a monotonic decrease with increasing active layer thickness until $L \geq 290$ nm, beyond which PCE exhibits a slight increase following the small changes in the fill factor and J_{SC} over the same range of L. Overall, a thinner active layer enables a higher device efficiency in the device structure of choice. For device fabrication purposes, although the device with only one layer of assembled nanoparticles as the active layer has the highest predicted PCE, it may suffer from problems of film uniformity or full interfacial area coverage. Consequently, based on this study, we propose a device fabrication strategy with an active layer thickness of ~140 nm, which consists of about two layers of assembled nanoparticles, is likely to provide a full

coverage of the interlayer interfacial area, and has the highest exciton generation rate, an optimal fill factor, and the potential for achieving an improved device power conversion efficiency.

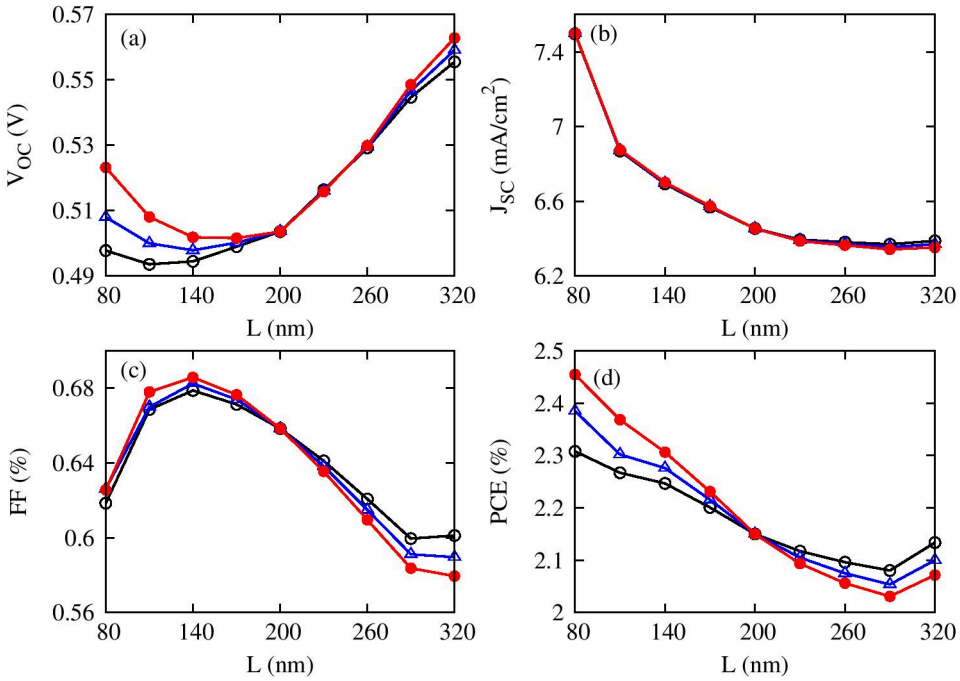

Figure 3.13. Computational predictions of (a) open-circuit voltage, V_{OC}, (b) short-circuit current density, J_{SC}, (c) fill factor, FF, and (d) power conversion efficiency, PCE, for devices with active layer morphology of P3HT:PCBM blend nanoparticle assemblies with nanoparticle size of 80 nm as a function of the active layer thickness, L, over the range 80 nm $\leq L \leq$ 320 nm. Black open circles, blue open triangles, and red solid circles denote the above quantities for devices with both the geminate and bimolecular recombination rate coefficients varied by ±5%, ±10%, and ±15%, respectively, of their values at L = 200 nm, per 30 nm of active layer thickness in the simulations.

3.4 Summary and Conclusions

In summary, a numerical simulation study of hole transport in P3HT films of different nanostructures was carried out based on a drift-diffusion-reaction model that accounts for hole trapping and detrapping kinetics. Our simulations reproduced experimental data for photocurrent transients and determined material and kinetic

properties that govern hole transport in the P3HT films. We found the hole transport properties of P3HT nanoparticle assemblies without excess surfactant to be comparable with those of drop cast P3HT thin films and elucidated the role of excess surfactant in hole trapping. The charge carrier trapping and detrapping kinetics emphasized in our study have important implications for the design of OPV active layers, since space charge formation mediated by such trapping and detrapping can decrease internal electric fields and, therefore, promote bimolecular recombination and passivate charge separation. Our analysis demonstrates quantitatively the potential of using organic nanoparticles in developing active layers for OPV devices; this has been shown most clearly by the high zero-field mobility and the low net hole trapping rate of P3HT nanoparticle assemblies with the excess surfactant molecules removed, quantities that were found to be comparable with those of pristine P3HT thin films. The use of polymeric nanoparticle assemblies in the fabrication of OPV active layers introduces important control parameters, such as nanoparticle size and internal aggregate structure, to tune band structure and optimize charge transport efficiency.

Based on a properly formulated and carefully parameterized deterministic charge transport model, numerical simulation of electron and hole transport was carried out in OPV devices with active layers of blend and separate P3HT:PCBM self-assembled nanospheres. The charge transport model is similar to those developed for describing electron and hole transport in bulk heterojunction solar cells but includes proper modifications in the description of charge generation and bimolecular recombination rates in the active layer. Our simulations reproduced transient photocurrents measured in time-of-flight experiments, which was used to parameterize material defect (trap)

densities, as well as charge trapping and detrapping kinetics, in active layers consisting of both blend and separate nanoparticle assemblies. By fitting the model predictions to the experimental data of steady-state J-V curves in OPV devices with active layers of P3HT:PCBM nanoparticle assemblies, we also quantified nanoparticle size effects in both types of active layer samples and nanoparticle ratio effects in active layers of separate nanoparticle assemblies. The electrical and optical simulation results provide valuable insights into tuning the active layer nanostructure and thickness toward achieving the maximum device power conversion efficiency. Our analysis on the effects of interlayers placed between the active layer and the electrodes emphasizes the importance of proper band energy design and charge selectivity for effective charge extraction. The findings of our modeling study support a device fabrication strategy with a sufficiently thin active layer to optimize charge transport efficiency and improve device power conversion efficiency over the range of the experimental processing and device operation conditions examined. This approach has the potential to further optimize device performance by optimally designing proper interlayer thicknesses in conjunction with the active layer thickness through combined optical and electrical modeling.

CHAPTER 4

CHARGE TRANSPORT IN PHOTOVOLTAIC DEVICES BASED ON HYBRID PEROVSKITE PLANAR HETEROJUNCTIONS

4.1 Introduction

Organometallic halide perovskites have emerged as promising materials for next-generation solar cells. High power conversion efficiency can be achieved due to several key properties of hybrid perovskites, including their large absorption coefficient, direct band gap, high intrinsic carrier density on the order of 10^9 cm^{-3}, and high and balanced charge mobilities over the range of 1-10 $cm^2/(Vs)$ [117-120]. Mesoporous structures and planar heterojunctions have been commonly adopted for fabricating hybrid perovskite photovoltaic devices. Although both types of structures enable a high PCE of ~15%, devices with the mesoporous scaffold require a complex nanostructure design and a high fabrication temperature for sintering, especially when mesoporous TiO_2 is involved in dye sensitized solar cells [23,121,122]. On the other hand, planar heterojunctions are rather simple to prepare based on fabrication processes that employ simple solution methods.

Hybrid perovskite materials have ambipolar charge transport properties. The conventional wisdom for charge transport in perovskites is that electron and hole transport are spatially separated within the crystalline domain, leading to a bimolecular recombination rate that is at least four orders of magnitude lower than that predicted by Langevin theory [117]. Planar heterojunctions without a hole transporting layer (HTL) have been fabricated and investigated. The highest PCE that has been achieved in such

devices is around 11%, which is much lower than those achieved in devices with a HTL [123,124]. In fact, using both a HTL and an electron transporting layer (ETL) is required in order to form energy band alignments with the hybrid perovskite and the electrode for promoting charge carrier extraction and further reducing the bimolecular recombination rate by reducing the accumulation of charges at the perovskite/electrode interfaces. In this chapter, photovoltaic devices based on hybrid perovskite planar heterojunctions are investigated. The layered structure of these devices is cathode/ETL/perovskite/HTL/anode with planar interface morphologies.

The deterministic charge transport models developed in Chapter 3 for OPV devices are extended here for hybrid perovskite solar cells with planar heterojunctions. Although this type of charge transport modeling has been applied widely to study the function of both inorganic and organic photovoltaic devices, it has not yet been used extensively and systematically to study charge transport and to optimize the performance of photovoltaic devices based on hybrid perovskite planar heterojunctions. In recent theoretical studies using device-scale simulation, bimolecular recombination was identified to have a dominant effect on the device's open-circuit voltage [125]. A simulator based on charge transport modeling in inorganic semiconductors has been applied to study interface defect densities, perovskite absorber thickness, and the effects on interfacial recombination of the band offsets of perovskite absorber/charge transport layers [126,127]. In this chapter, using device simulation based on the extended deterministic charge transport models, experimental J-V curves are reproduced to examine the effects of incorporating MWCNTs in the perovskite active layer. The effects on the device performance of charge carrier mobilities in each layer, majority doping in

the ETL and the HTL, as well as electronic band offsets in the layered device are analyzed and discussed.

Specifically, our models have been used to study the function of hybrid perovskite solar cells based on planar heterojunctions that have been fabricated with both HTL and ETL using a sequential deposition technique as reported in Ref. 128. In brief, in this fabrication method, PbI_2 in N,N-dimethylformamide (DMF) is spin coated on a PEDOT:PSS-coated ITO substrate. Mixed counterions of methylammonium iodide and formamidinium iodide are dissolved in isopropanol. The solution is then spin coated on top of the PbI_2 films, followed by the spin coating of a thin layer of PCBM. Finally, Ca and Al are deposited sequentially on top of the PCBM layer. MWCNTs are incorporated into the perovskite active layer at three different concentrations (by wt. to PbI_2): 0%, 0.005%, and 0.01%. The experimental J-V curves are reproduced by the model predictions, which provide quantitative explanations for the effects on perovskite photovoltaic device performance of incorporating MWCNTs in the hybrid perovskite active layer.

4.2 Charge Transport Model Description

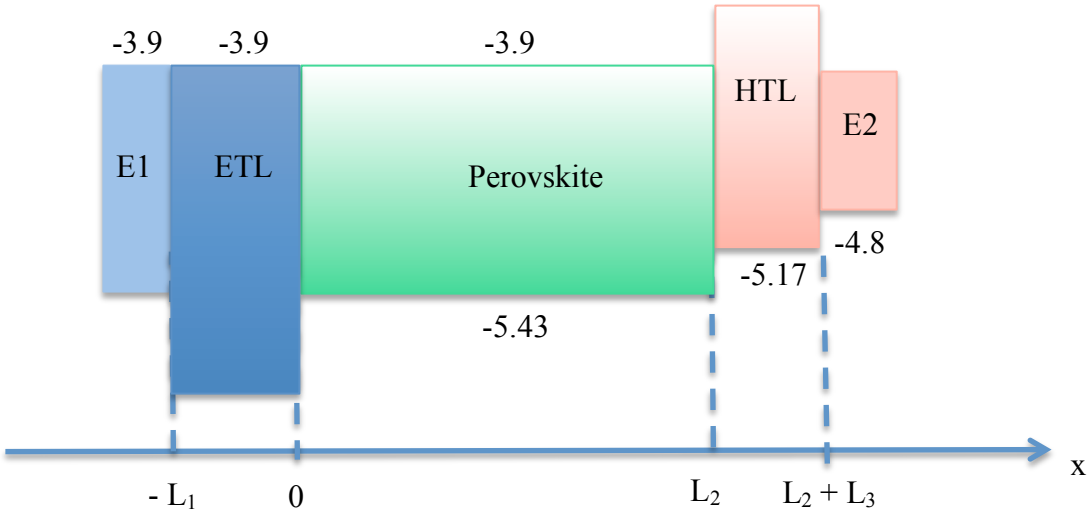

Figure 4.1. Schematic depiction of band alignments (electronic band energy levels in eV along the device in the direction perpendicular to the electrodes, E1 and E2) for a device based on hybrid perovskite planar heterojunctions. The numbers refer to the corresponding energy levels in eV.

The band energy alignments of the Ca/Al cathode (E1), PCBM (ETL), perovskite, PEDOT:PSS (HTL), and ITO (E2) layers in the fabricated devices are shown in Fig. 4.1, with L_1 = 60 nm, L_2 = 300 nm, and L_3 = 40 nm being the thicknesses of the PCBM, perovskite, and PEDOT:PSS layers, respectively. The values of the electronic band energies used for computing the device's J-V curves in steady-state charge transport simulations are listed in Fig. 4.1. The steady-state charge transport models are governed by Eqs. (4.1)-(4.7) given below.

In the PCBM layer, the governing equations for electron transport are

$$\frac{d}{dx}\left(D_n\frac{dn}{dx}+\mu_n nE\right)=0 \tag{4.1}$$

and

$$\frac{d^2U}{dx^2} = \frac{e(n - \rho_n)}{\varepsilon_0 \varepsilon_r}. \tag{4.2}$$

In the perovskite layer, the governing equations for electron and hole transport are

$$\frac{d}{dx}\left(D_n \frac{dn}{dx} + \mu_n nE\right) - C_{bi}\gamma\left(np - n_i^2\right) + G_0 = 0, \tag{4.3}$$

$$\frac{d}{dx}\left(D_p \frac{dp}{dx} - \mu_p pE\right) - C_{bi}\gamma\left(np - n_i^2\right) + G_0 = 0, \tag{4.4}$$

and

$$\frac{d^2U}{dx^2} = -\frac{e(p - n + N_t)}{\varepsilon_0 \varepsilon_r}. \tag{4.5}$$

Finally, in the PEDOT:PSS layer, the governing equations for hole transport are

$$\frac{d}{dx}\left(D_p \frac{dp}{dx} - \mu_p pE\right) = 0 \tag{4.6}$$

and

$$\frac{d^2U}{dx^2} = -\frac{e(p - \rho_p)}{\varepsilon_0 \varepsilon_r}. \tag{4.7}$$

In each layer, the continuity equation(s) for the electron density (n) and/or hole density (p) is/are coupled self-consistently with Poisson's equation for the electrostatic potential (U) in the layer. In the PCBM and PEDOT:PSS layers (i.e., the acceptor and donor materials of the ETL and HTL, respectively), only a single type of charge carrier transport is considered, while both electron and hole transport are accounted for in the

perovskite layer due to its ambipolar charge transport nature. In Eqs. (4.1)-(4.7), e, k_B, T, and ε_0 denote the elementary charge, Boltzmann's constant, temperature, and vacuum permittivity, respectively, and ε_r denotes the relative permittivity of the corresponding material; for the perovskite material used, ε_r is set to be 70 [129]. For PCBM and PEDOT:PSS, ε_r = 3.5 is chosen, as a typical value for organic semiconductor materials. The diffusion coefficient D_i (i = n, p referring to electrons and holes, respectively) is related to the respective charge carrier mobility μ_i by the Einstein relation, $D_i = \mu_i k_B T/e$. E is the magnitude of the electric field, which is given locally by the gradient of the electrostatic potential, and n_i is the intrinsic charge density of the perovskite material. Exciton generation in the perovskite material is of Wannier type [130]. In Eqs. (4.3) and (4.4), G_0 is the free electron and hole generation rate and is assumed to be uniform in the perovskite layer. The bimolecular recombination rate constant γ follows Langevin theory [92], where $\gamma = e(\mu_n+\mu_p)/(\varepsilon_0\varepsilon_r)$. This expression for γ is found to give values that are orders of magnitude higher than those required to reproduce the experimental measurements [117,131,132] which is accounted for by using a prefactor, C_{bi}, in the kinetic expression for the Langevin recombination rate, Eqs. (4.3) and (4.4). It should be pointed out that at the acceptor/perovskite and perovskite/donor interfaces, the surface recombination rate is considered explicitly. The ratio of the surface recombination rate at the acceptor/perovskite and perovskite/donor interface over that in the bulk of the perovskite layer is denoted by C_L and C_R, respectively. N_t in Eq. (4.5) denotes the ionized p-type defect density in the perovskite layer. Finally, in Eqs. (4.2) and (4.7), ρ_n and ρ_p denote electron doping density in ETL and hole doping density in HTL, respectively. In the experiments of Ref. 128 that we want to reproduce with our

modeling, ETL and HTL are not intentionally doped, and, therefore, ρ_n and ρ_p are equal to zero in these cases.

The boundary conditions that the governing transport equations, Eqs. (4.1)-(4.7), have to satisfy are consistent with those of Ref. 133. In summary, an Ohmic boundary condition is applied at the cathode/ETL interface. At the ETL/perovskite interface, there is a discontinuity in the electron density and a continuity condition is satisfied for the photocurrent density. The electrostatic potential at the cathode/ETL interface is fixed by the applied voltage in the experiment. At the ETL/perovskite interface, continuity conditions are satisfied for both the electrostatic potential and the electric displacement. An analogous set of boundary conditions can be expressed at the perovskite/HTL and HTL/anode interfaces. The boundary-value problems for n, p, and U are solved using the open–source software Chebfun [134].

4.3 Results and Discussion

4.3.1 Effects of Incorporating MWCNTs in Hybrid Perovskite Active Layer

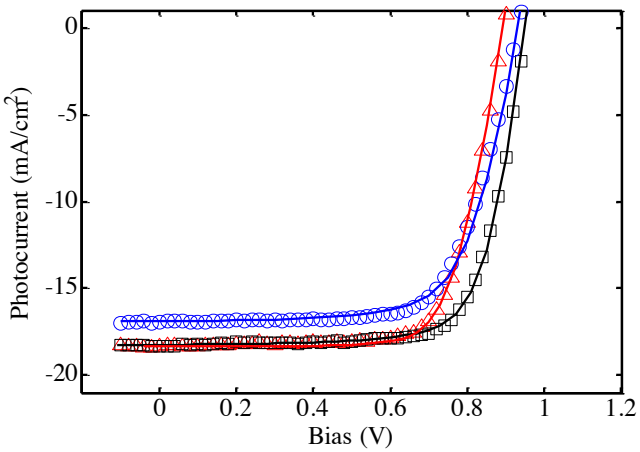

Figure 4.2. Best fits of the experimental data (open symbols) using the simulation predictions (continuous lines) according to the model of Eqs. (4.1)-(4.7) for the steady-state J-V curves in perovskite photovoltaic devices with MWCNT concentrations (by wt. to PbI_2) of 0% (red), 0.005% (black), and 0.01% (blue) under steady exposure to light.

Figure 4.2 shows the fitting of the simulation predictions according to the model of Eqs. (4.1)-(4.7) to the experimentally measured J-V curves at steady state of light exposure for perovskite samples with MWCNTs in the active layer at concentrations (by wt. to PbI_2) of 0%, 0.005%, and 0.01%. The derived fitting parameters are summarized in Table 4.1. In the experiments of Ref. 128, the photocurrent saturates gradually with decreasing applied bias. This saturation photocurrent under reverse bias is approximated by eL_2G_0 [135], where drift current dominates diffusion current. G_0 is estimated to be 3.8×10^{27} $m^{-3}s^{-1}$ for MWCNTs at concentrations of 0 and 0.005 wt% and 3.6×10^{27} $m^{-3}s^{-1}$ at a MWCNT concentration of 0.01 wt%. The slight decrease in charge generation can be caused by the indirect interfacial contact between the MWCNTs and the perovskite [136].

The intrinsic carrier density n_i in the perovskite layer is given an upper bound equal to the corresponding value in silicon (~10^{16} m^{-3}) [137] and should be on the same order of magnitude (~10^{15} m^{-3}) as that measured in experiments [119]. It is determined to be 5.0×10^{15} m^{-3} by the fitting procedures that we employed. When incorporating p-type conducting MWCNTs in the perovskite layer, the electron and hole mobilities in the PCBM and PEDOT:PSS layers are not affected and the electron mobility in the perovskite layer also remains the same. However, hole mobility is increased by a factor of four with MWCNTs in the perovskite layer at a concentration of 0.01 wt%. At the high end of the MWCNT concentration examined in this study, a continuous pathway for hole extraction is formed. The bulk recombination rate coefficient C_{bi} is reduced by almost one order of magnitude when MWCNTs at a concentration of 0.005 wt% are incorporated into the perovskite layer. Nevertheless, a further increase in the MWCNT concentration does not lead to decrease of the bulk recombination rate coefficient. The ratio of the surface recombination rate to that in the bulk of the active layer, C_R, at the perovskite/PEDOT:PSS interface shows a similar trend but with a less abrupt decrease, while at the PCBM/perovskite interface, the corresponding ratio, C_L, remains unchanged. The significant reduction in the bulk recombination rate in conjunction with a decrease in the surface recombination rate at the perovskite/PEDOT:PSS interface causes an increase in the device's open-circuit voltage V_{OC} and results in improvement of the fill factor and the power conversion efficiency. Even though further reduction occurs when incorporating MWCNTs into the active layer at a higher concentration, the mismatch between the electron and hole mobilities prevents a further improvement in the overall device performance by decreasing the V_{OC}. Moreover, the ionized p-type defect density

N_t in the perovskite layer increases slowly with further incorporation of MWCNTs into the layer, which is an unfavorable effect for the optimization of the device performance.

Table 4.1. List of parameters derived from fitting the simulation predictions according to the model, Eqs. (4.1)-(4.7), to the experimental data of steady-state J-V curves under steady light exposure for perovskite photovoltaic devices containing MWCNTs in the active layer at different concentrations.

MWCNT concentration (by wt. to PbI_2)	0%	0.005%	0.01%
G_0 ($\times 10^{27}$ $m^{-3}s^{-1}$)	3.8	3.8	3.6
$\mu_{n,ETL}$ ($\times 10^{-8}$ $m^2/(Vs)$)	2.4	2.4	2.4
$\mu_{p,HTL}$ ($\times 10^{-8}$ $m^2/(Vs)$)	2.4	2.4	2.4
$\mu_{n,perovskite}$ ($\times 10^{-4}$ $m^2/(Vs)$)	1.0	1.0	1.0
$\mu_{p,perovskite}$ ($\times 10^{-4}$ $m^2/(Vs)$)	1.0	1.0	4.0
C_L	1.0	1.0	1.0
C_R	1.0	0.5	0.3
C_{bi} ($\times 10^{-7}$)	7.0	0.9	0.9
N_t ($\times 10^{23}$ m^{-3})	5.5	8.3	9.4

4.3.2 Sensitivity Analysis for Charge Mobilities in Hybrid Perovskite Layer

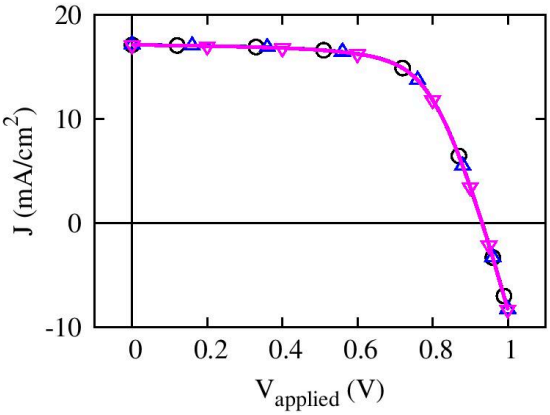

Figure 4.3. Computed J-V curves for values of the ratio of $\mu_{n,perovskite}/\mu_{p,perovskite}$ = 1 (black continuous line with open circles), 4 (blue continuous line with open triangles), and 9 (magenta continuous line with open inverse triangles).

In Chapter 4.3.1, we saw that the mismatch between electron and hole mobilities leads to a decrease in V_{OC} for the device with MWCNTs at the concentration of 0.01 wt%. Here, this charge carrier mobility mismatch effect is investigated further. The mobility ratio of $\mu_{n,perovskite}/\mu_{p,perovskite}$ is varied and J-V curves are computed for this parameter value set at 1, 4, and 9, respectively. All the other input parameters are kept the same as those for the device with MWCNTs at the concentration of 0.01 wt% in Table 4.1. Furthermore, the sum $\mu_{n,perovskite} + \mu_{p,perovskite}$ is kept constant at 5×10^{-4} m^2/(Vs) to maintain the same bimolecular recombination rate. The computed J-V curves are shown in Fig. 4.3. It is evident from these results that variations in the ratio $\mu_{n,perovskite}/\mu_{p,perovskite}$ do not affect device performance. The ratio $\mu_{p,perovskite}/\mu_{n,perovskite}$ also is examined as a parameter in the same way and the steady-state J-V curves are found to not change with this parameter's variation either. Since ($\mu_{n,perovskite} + \mu_{p,perovskite}$) is kept

constant, the bimolecular recombination rate coefficient $C_{bi}(\mu_{n,perovskite} + \mu_{p,perovskite})$ remains the same. As a result, the device's V_{OC} is not affected by the mismatch in the electron and hole mobilities in the hybrid perovskite layer under the condition of a constant bimolecular recombination rate.

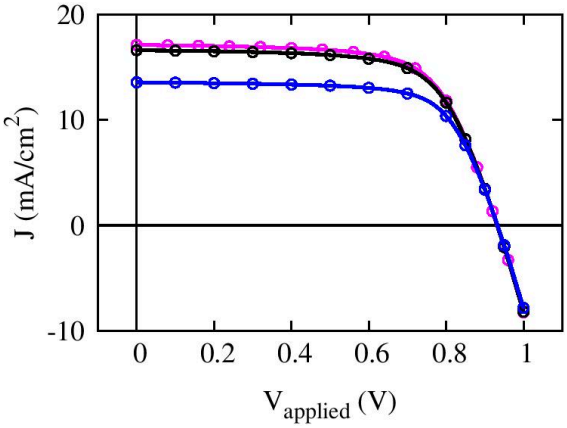

Figure 4.4. Computed J-V curves for $C_{bi} = 9\times10^{-9}$ and $\mu_{n,perovskite} + \mu_{p,perovskite} = 5\times10^{-3}$ m^2/(Vs) (magenta continuous line with open circles), $C_{bi} = 9\times10^{-6}$ and $\mu_{n,perovskite} + \mu_{p,perovskite} = 5\times10^{-6}$ m^2/(Vs) (black continuous line with open circles), and $C_{bi} = 9\times10^{-5}$ and $\mu_{n,perovskite} + \mu_{p,perovskite} = 5\times10^{-7}$ m^2/(Vs) (blue continuous line with open circles).

Furthermore, $C_{bi}(\mu_{n,perovskite} + \mu_{p,perovskite})$ is kept constant while C_{bi} and $(\mu_{n,perovskite} + \mu_{p,perovskite})$ are varied inversely proportional to each other. The computed J-V curves are shown in Fig. 4.4. When C_{bi} and $(\mu_{n,perovskite} + \mu_{p,perovskite})$ are varied within three orders of magnitude, i.e., over the range from $C_{bi} = 9\times10^{-9}$ and $(\mu_{n,perovskite} + \mu_{p,perovskite}) = 5\times10^{-3}$ m^2/(Vs) to $C_{bi} = 9\times10^{-6}$ and $(\mu_{n,perovskite} + \mu_{p,perovskite}) = 5\times10^{-6}$ m^2/(Vs), respectively, the J-V curves remain almost unaffected. When C_{bi} is increased further to 9×10^{-5} and $(\mu_{n,perovskite} + \mu_{p,perovskite})$ is decreased further to 5×10^{-7} m^2/(Vs), the short-circuit current density J_{SC} decreases substantially without affecting the value of V_{OC}. However, the low and high limits of charge carrier mobilities in organometallic halide perovskite are on the orders of 1×10^{-4} m^2/(Vs) and 10^{-3} m^2/(Vs), respectively [117,138].

Therefore, with a constant bimolecular recombination rate, the effects of varying electron and hole mobilities in the perovskite active layer on the overall performance of the hybrid perovskite device are very limited, even when these carrier mobilities in the perovskite active layer are mismatched.

4.3.3 Effects of Electronic Band Offsets on the Sensitivity Analysis for Charge Mobility and Majority Doping in Electron and Hole Transporting Layers

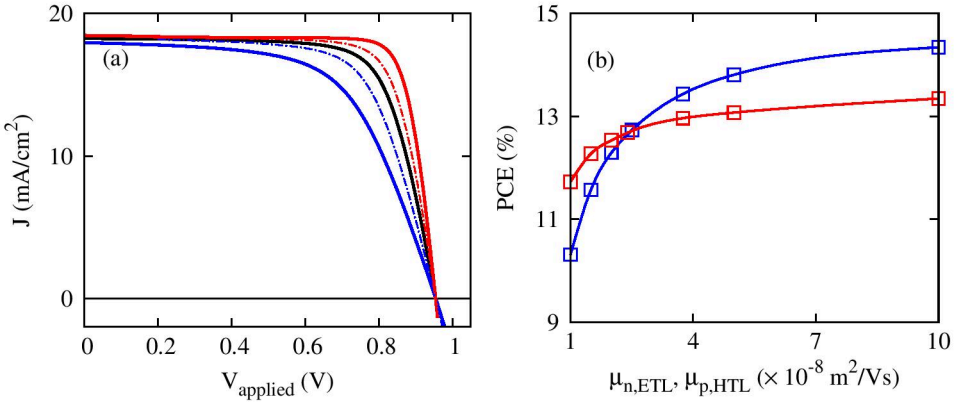

Figure 4.5. (a) Computed J-V curves for $\mu_{n,ETL} = \mu_{p,HTL} = 2.4\times10^{-8}$ m^2/(Vs) as the reference case (black continuous line), for $\mu_{n,ETL} = 1\times10^{-8}$ and 1×10^{-7} m^2/(Vs) (blue and red continuous lines, respectively), and for $\mu_{p,HTL} = 1\times10^{-8}$ and 1×10^{-7} m^2/(Vs) (blue and red dot-dashed lines, respectively). (b) Computed PCE as $\mu_{n,ETL}$ (blue line with open squares) or $\mu_{p,HTL}$ (red line with open squares) only is varied, respectively, over the range from 1.0×10^{-8} to 1.0×10^{-7} m^2/(Vs). The electronic band energy levels in the device correspond to those of Figure 4.1.

For the current material choices, charge mobilities in the hybrid perovskite active layer are about four orders of magnitude higher than the electron mobility in the ETL, consisting of fullerene derivatives, and the hole mobility in the HTL, consisting of organic semiconducting polymers. The carrier mobilities in the two transporting layers

typically range from 1×10^{-8} to 1×10^{-7} $m^2/(Vs)$, depending on the degree of material crystallinity that can be varied by using different processing conditions. The effects on the device efficiency are studied by varying the carrier mobilities, $\mu_{n,ETL}$ and $\mu_{p,HTL}$, over this range. All the other input parameters are kept the same as those for the perovskite active layer with incorporation of MWCNTs at the concentration of 0.005 wt% in Table 4.1. The computed J-V curves and device PCE are shown in Figs. 4.5(a) and 4.5(b), respectively. By comparing the results of Fig. 4.5 with those of Figs. 4.3 and 4.4, it is evident that varying $\mu_{n,ETL}$ and $\mu_{p,HTL}$ have much more significant effects on the device performance than varying the carrier mobilities in the hybrid perovskite active layer. A decrease or an increase in either $\mu_{n,ETL}$ or $\mu_{p,HTL}$ results in a reduction or an improvement, respectively, in the device's fill factor FF without changing the values of J_{SC} or V_{OC}. Moreover, when either $\mu_{n,ETL}$ or $\mu_{p,HTL}$ are varied from 1×10^{-8} to 1×10^{-7} $m^2/(Vs)$, the device PCE changes significantly, namely, from 10.3% to 14.3% for $\mu_{n,ETL}$ variation over this range and (less significantly) from 11.7% to 13.3% for $\mu_{p,HTL}$ variation over this range. We conclude from these results that the device PCE is more sensitive in variations of $\mu_{n,ETL}$ than variations of $\mu_{p,HTL}$.

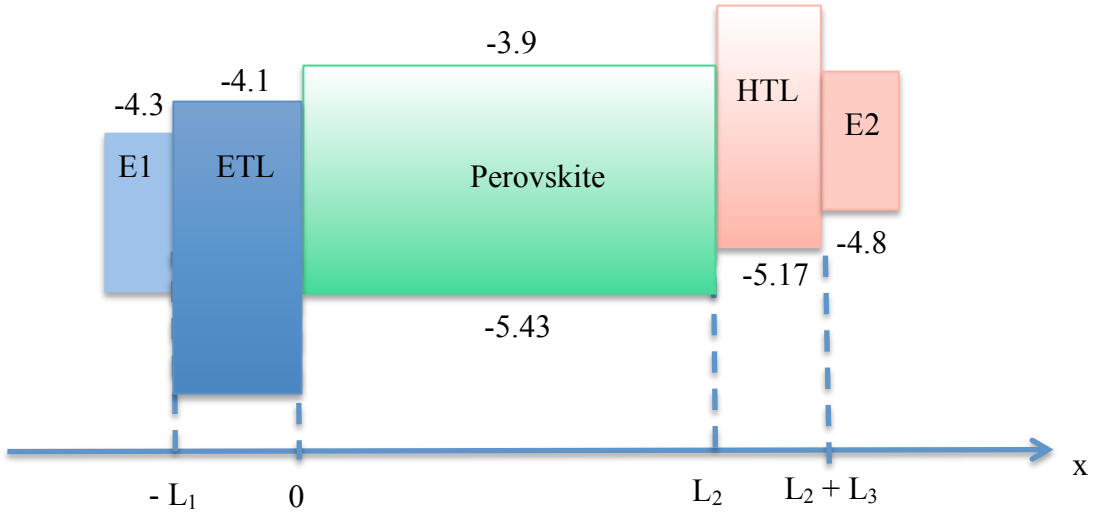

Figure 4.6. Schematic depiction of electronic band realignments for the device of Figure 4.1 based on hybrid perovskite planar heterojunctions. The numbers refer to the corresponding energy levels in eV.

The different sensitivities in variations in $\mu_{n,ETL}$ and $\mu_{p,HTL}$ of the device performance raise a question on the importance of the role that variations in the band offsets at the cathode/ETL/perovksite and the perovskite/HTL/anode interfaces may play in determining the effects of charge carrier mobilities in the ETL and HTL. As shown in Fig. 4.1, distinct electronic band alignments are formed at the two sets of junctions. The cathode work function, LUMO level of ETL, and conduction band edge of the hybrid perovskite layer are well matched. On the other side, however, a staggered band alignment is formed for the valence band edge of the hybrid perovskite layer, the HOMO level of HTL, and the anode work function. To study the effects of varying $\mu_{n,ETL}$ and $\mu_{p,HTL}$ with symmetric electronic band offsets at both sets of junctions, the band energy levels are redesigned for the cathode and ETL, as shown in Fig. 4.6. For this redesigned arrangement $\mu_{n,ETL}$ and $\mu_{p,HTL}$ are varied again over the range of $[1\times10^{-8}, 1\times10^{-7}]$ $m^2/(Vs)$ and the resulting computed J-V curves and device PCEs are shown in Fig. 4.7. Even with

symmetric band offsets at the two sets of junctions, the device PCE remains more sensitive toward variations in $\mu_{n,ETL}$. However, the resulting variation in the device's PCE occurs within a narrower range compared to the computed PCE in Fig. 4.5(b) corresponding to the electronic band alignments of Fig. 4.1, from 12.6% to 14.5% and from 13.2% to 14.2% for $\mu_{n,ETL}$ variation and for $\mu_{p,HTL}$ variation, respectively, over the considered mobility range.

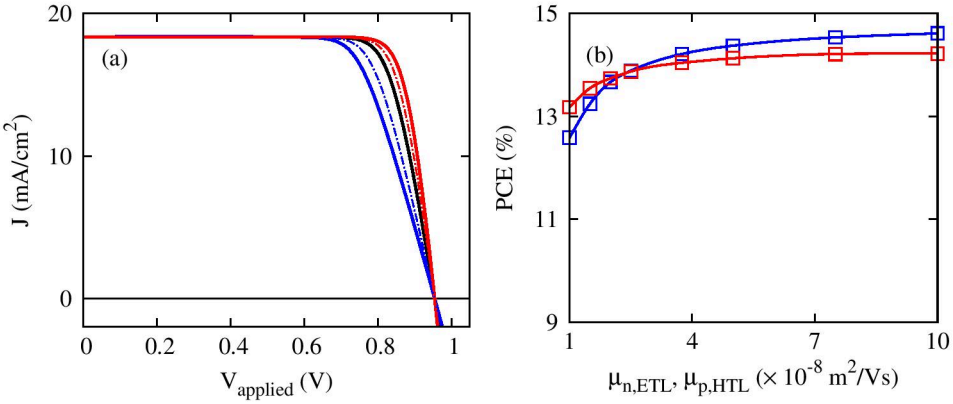

Figure 4.7. (a) Computed J-V curves for $\mu_{n,ETL} = \mu_{p,HTL} = 2.4\times10^{-8}$ m^2/(Vs) as the reference case (black continuous line), for $\mu_{n,ETL} = 1\times10^{-8}$ and 1×10^{-7} m^2/(Vs) (blue and red continuous lines, respectively), and for $\mu_{p,HTL} = 1\times10^{-8}$ and 1×10^{-7} m^2/(Vs) (blue and red dot-dashed lines, respectively). (b) Computed PCE as $\mu_{n,ETL}$ (blue line with open squares) or $\mu_{p,HTL}$ (red line with open squares) only is varied, respectively, from 1.0×10^{-8} to 1.0×10^{-7} m^2/(Vs). The electronic band energy levels in the device correspond to those shown in Figure 4.6.

Majority carrier doping in Spiro-OMeTAD, which is commonly used as the HTL material in hybrid perovskite solar cells, has been demonstrated to enhance the device efficiency [139]. Here, the effects of majority doping in both the ETL and HTL materials, i.e., doping the ETL material with n-type dopants and the HTL material with p-type dopants, are examined. The computed J-V curves and the resulting device PCE are shown in Figs. 4.8(a) and 4.8(b), respectively, for a device with band alignment

corresponding to that in Fig. 4.1 and in Figs. 4.9(a) and 4.9(b), respectively, for a device with band alignment corresponding to that in Fig. 4.6. Similar to the effects of increasing carrier mobilities in the ETL and HTL materials, increasing the majority dopant density improves the device's FF without changing J_{SC} and V_{OC}. For the device with the band alignment arrangement of Fig. 4.1, electron doping in ETL increases PCE by ~2%, namely, from 12.7% to 14.6%, over the examined dopant density range from 0 to $\rho_0 = 5.5\times10^{23}$ m^{-3}. The device's PCE increases abruptly when ρ_n increases from 0 to $0.1\rho_0$. It continues to increase with a dopant desnity increase up to $\rho_n = 0.5\ \rho_0$ and remains practically the same with further doping. On the contrary, hole doping in the HTL material results in only an increase by 0.3% in the device's PCE, namely, from 12.7% to 13.0%, with most of the increase happening as ρ_p increases between $\rho_p = 0$ and $\rho_p = 0.1\rho_0$. In contrast to this response to doping, however, when the device has staggered band offsets as that shown in Fig. 4.6, the increase in PCE resulting from electron doping is reduced to 1%, namely, from 13.8% to 14.8%, while from hole doping is increased to 0.5%, namely, from 13.8% to 14.3%.

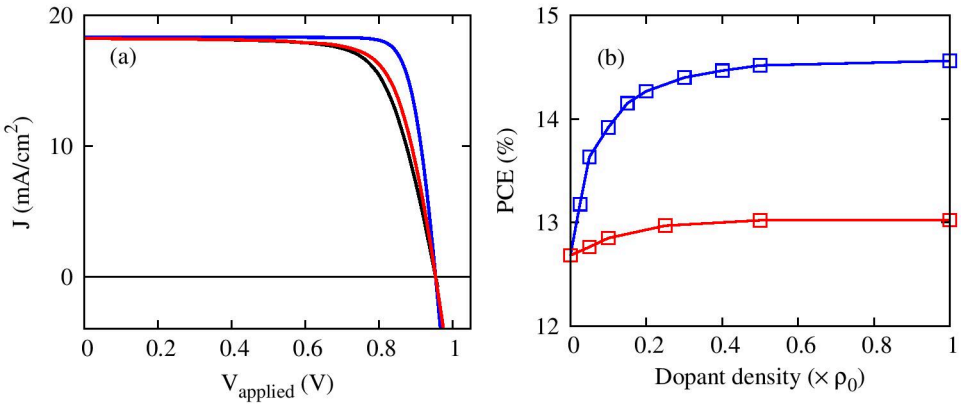

Figure 4.8. (a) Computed J-V curves in the absence of dopants (black continuous line) and for dopant density $\rho_n = \rho_0$ (blue continuous line) and $\rho_p = \rho_0$ (red continuous line), where $\rho_0 = 5.5\times10^{23}$ m^{-3}. (b) Computed PCE as the dopant density ρ_n (blue line with open squares) and ρ_p (red line with open squares), respectively, is varied over the range from 0 to ρ_0. The electronic band energy levels in the device correspond to those of Figure 4.1.

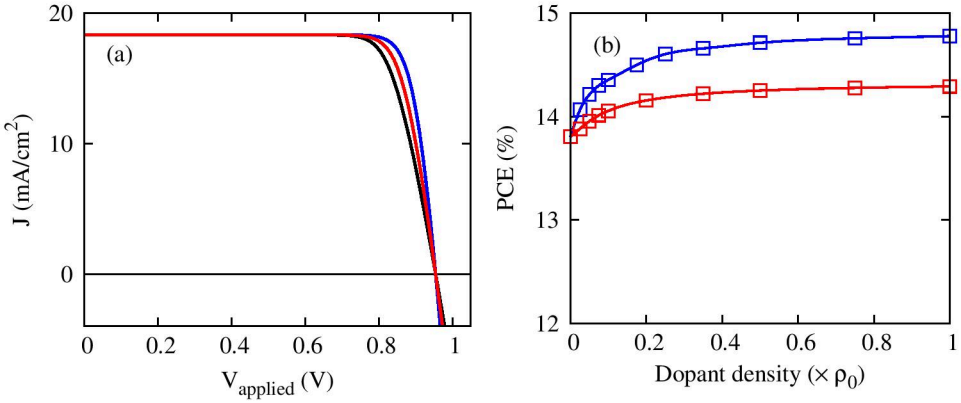

Figure 4.9. (a) Computed J-V curves in the absence of dopants (black continuous line) and for dopant density $\rho_n = \rho_0$ (blue continuous line) and $\rho_p = \rho_0$ (red continuous line), where $\rho_0 = 5.5 \times 10^{23}$ m^{-3}. (b) Computed PCE as the dopant density ρ_n (blue line with open squares) and ρ_p (red line with open squares), respectively, is varied over the range from 0 to ρ_0. The electronic band energy levels in the device correspond to those of Figure 4.6.

4.4 Summary and Conclusions

Based on deterministic charge transport models, numerical simulations of electron and hole transport have been carried out in photovoltaic devices based on organometallic halide perovskite planar heterojunctions. By fitting the model predictions to experimental data of steady-state J-V curves under steady illumination, it was demonstrated that the overall device performance is improved by effectively incorporating MWCNTs into the perovskite layer due to the reduction of the bulk recombination rate and the resultant increase in the open-circuit voltage. As the MWCNT concentration in the active layer increases, the ionized p-type defect density increases, leading to a decrease in the fill factor. Therefore, an optimal concentration of MWCNTs has been found to exist for maximizing the device efficiency. Moreover, variations in the mismatch between electron and hole mobilities and in the magnitude of these two carrier mobilities over the typical range for hybrid perovskite materials are found to have a negligible effect on the device performance if the bimolecular recombination rate in the active layer is kept constant. Band offsets at the cathode/ETL/perovskite and perovskite/HTL/anode interfaces play a significant role in determining the effects on the device PCE of the carrier mobilities and the majority doping in the ETL and HTL materials. Therefore, the model predictions provide very helpful guidelines toward optimal design of photovoltaic devices based on hybrid perovskite active layers in order to maximize their performance.

CHAPTER 5

SUMMARY, CONCLUSIONS, AND FUTURE WORK

5.1 Summary and Conclusions

This thesis presented a systematic theoretical study of atomic species transport in ternary semiconductor quantum dots and of charge carrier transport in photovoltaic active layers of organic semiconducting materials and organometallic halide perovskites. The analysis of species transport in ternary quantum dots was based on a continuum-scale model of atomic transport in spherical nanocrystals which takes into account the drift due to the thermodynamic driving force for atomic species surface segregation as a result of the elastic interaction between the atomic constituent species and the nanocrystal surface. The analysis of charge transport was based on deterministic charge transport models describing the evolution of the density fields of free and trapped charge carriers and of charge pairs, coupled self-consistently with Poisson's equation for the electric field in each active layer.

In Chapter 2, the interdiffusion kinetics was analyzed of group-VI species in $ZnSe_{1-x}S_x$ and $ZnSe_{1-x}Te_x$ ternary quantum dots (TQDs) and of group-III species in $In_xGa_{1-x}As$ TQDs. The modeling results were used to interpret the evolution of species near-surface concentration during thermal annealing according to XPS measurements and predict the equilibrium species distribution as a function of TQD size and composition. A systematic parametric analysis generated a database of transport properties for atomic transport in the above TQDs. The findings of the analysis resulted in a proposal for an efficient one-step TQD synthesis method followed by thermal annealing to promote self-

assembly of the thermodynamically stable configuration of these semiconductor nanocrystals that guarantee optimal optoelectronic function in devices based on these TQDs.

Chapter 3 focused on charge transport in organic photovoltaic active layers of self-assembled nanospheres. Fitting the modeling predictions to experimental data of transient photocurrents and steady-state photocurrent density-voltage relations was used to examine the propensity of the active layer material to generate charge and form defects, determine charge carrier transport properties such as zero-field electron and hole mobilities and their Poole-Frenkel field dependence, analyze the kinetics of charge trapping and detrapping processes, and investigate charge pair dissociation as well as bimolecular and geminate recombination. The modeling results were used to demonstrate quantitatively that charge transport efficiencies in P3HT centrifuged nanoparticle assemblies are comparable with those in P3HT drop cast thin films, which provides the required performance evidence for designing OPV devices with active layers of self-assembled nanospheres. The modeling results also were used to analyze the effects on device performance of nanoparticle size in blend and separate P3HT:PCBM nanoparticle assemblies and of the nanoparticle number ratio in separate P3HT:PCBM nanoparticle assemblies. The analysis of the effects on photovoltaic device performance of interlayers placed between the active layer and the electrodes emphasized the importance of proper electronic band energy design and charge selectivity for effective charge extraction. Moreover, optical modeling based on the transfer matrix method was used to maximize charge generation rate by properly tuning the active layer thickness. The electrical and optical simulation results have provided valuable insights into

controlling the active layer nanostructure and thickness toward achieving the maximum device power conversion efficiency.

The deterministic charge transport models developed in Chapter 3 were modified and extended for the analysis of photovoltaic devices based on hybrid perovskite planar heterojunctions, which was presented in Chapter 4. Specifically, in Chapter 4, the effects on bulk bimolecular recombination, interface recombination, and p-type ionized defect density were investigated upon incorporating multi-walled carbon nanotubes into the hybrid perovskite layer. The analysis of the effects of charge carrier mobilities and majority doping in the electron and hole transporting layers emphasized the importance of tuning the ETL and HTL properties toward improving the device's power conversion efficiency. The analysis also revealed that electronic band alignments at the cathode/ETL/perovskite and perovskite/HTL/anode junctions determine the effects on the device PCEs of the charge carrier mobilities and the majority doping in the ETL and HTL materials. The modeling predictions have provided valuable insights into the function of hybrid perovskite solar cells with planar heterojunctions, as well as guidelines toward the optimal design of such devices.

5.2 Future Work

From the various possible future research directions that can be pursued based on the research findings presented in this thesis, we choose to focus here on immediate future directions on charge transport analysis toward device performance optimization of perovskite-based solar cells due to the timeliness and significance of this research topic.

5.2.1 Effects of Electronic Band Offsets on Charge Carrier Mobilities and Majority Doping in Electron and Hole Transporting Layers

In Chapter 4, two types of electronic band offsets were investigated for their effects on the sensitivity analysis of charge mobilities and majority doping in ETL and HTL. Other electronic band alignments in addition to those examined in Chapter 4 also are possible in perovskite-based photovoltaic devices. The device of Fig. 5.1, is characterized by staggered band offsets at the cathode/ETL/perovskite junctions and well-aligned energy bands at the perovskite/HTL/anode junctions. In Fig. 5.2, both sets of junctions exhibit well-aligned electronic band energy levels. It is worth investigating the effects of these two types of band alignments on the sensitivity of the device's PCE with variation of charge mobilities and majority doping in ETL and HTL. For photovoltaic devices with the band offsets of Fig. 5.1, the results may be comparable to those with the band alignment of Fig. 4.1. However, for devices with the band offsets of Fig. 5.2, the device PCE may be highly sensitive with respect to variations in charge mobilities and majority doping in ETL and HTL. Such systematic sensitivity analyses for the band offsets of Figs. 5.1 and 5.2 will shed light toward optimal materials design with respect to photovoltaic performance.

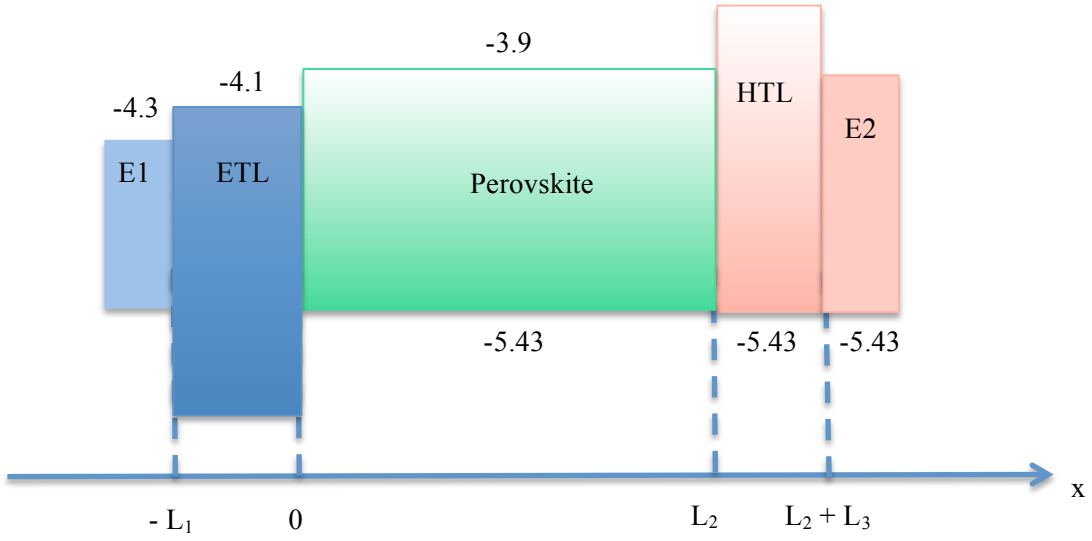

Figure 5.1. Schematic depiction of electronic band realignments for the device of Figure 4.1 based on hybrid perovskite planar heterojunctions. The numbers refer to the corresponding energy levels in eV.

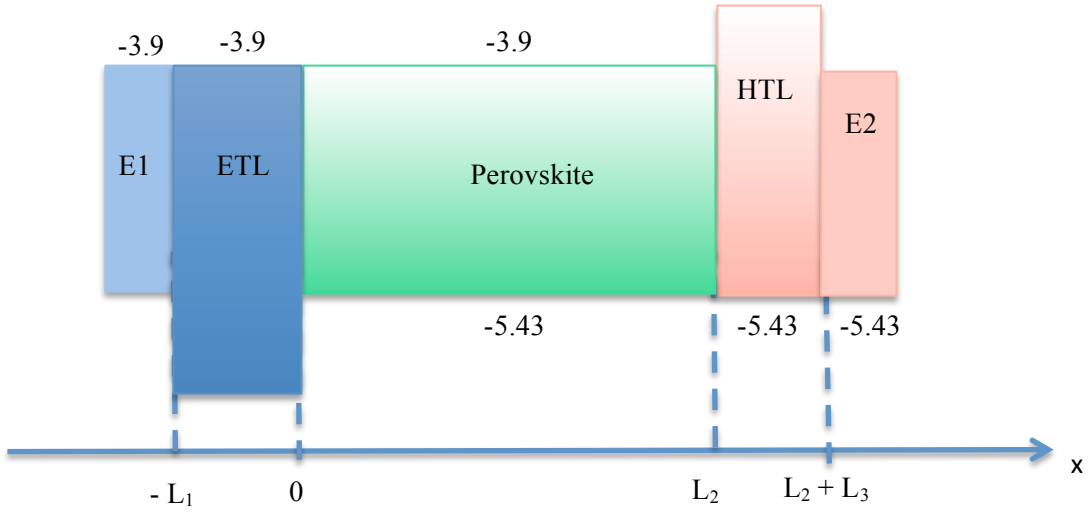

Figure 5.2. Schematic depiction of electronic band realignments for the device of Figure 4.1 based on hybrid perovskite planar heterojunctions. The numbers refer to the corresponding energy levels in eV.

5.2.2 Effects of Band Offsets on the Device's Open-Circuit Voltage

The charge transport models employed in Chapter 4 predict no effects on V_{OC} when the corresponding electronic band offsets are redesigned from those in the device of Fig. 4.1 to those of the device of Fig. 4.6. However, it was discussed in Chapter 3 that the band offsets of active layers in OPV devices determine the built-in voltage V_{bi}, which modifies the device's open-circuit voltage, V_{OC}. For OPV devices without any interlayers, V_{bi} is equal to the difference in the work function of the two metal electrodes, which is the same as the metal-insulator-metal (MIM) model prediction. For OPV devices with interlayers, V_{bi} is equal to the difference in the HOMO and LUMO levels of the corresponding interlayers. For photovoltaic devices based on hybrid perovskite planar heterojunctions, it is not clear how V_{bi} is determined and if V_{bi} or the interface recombination, as discussed in Ref. 126, is the decisive factor for determining V_{OC}. A thorough understanding of the relation between band offsets and V_{OC} is extremely important. With such an understanding established, this study will be continued further for designing the device layout for further improvement of the device's PCE in hybrid perovskite solar cells.

5.2.3 Optimization of Device Performance in Hybrid Perovskite Solar Cells by Controlling the Active Layer Thicknesses

Device parameters discussed in Chapter 4 affected V_{OC} and the device's fill factor, FF, but not the short-circuit current density, J_{SC}. To further increase the device's PCE, it is necessary to improve the extracted photocurrent. The charge generation rate is directly related to the steady-state photocurrent. In Chapter 3, optical modeling based on the

transfer matrix method was employed to predict the charge generation rate with respect to the active layer thickness. Following a similar approach, the charge generation rate will be investigated as a function of the thicknesses of ETL, hybrid perovskite layer, and HTL. The thickness of the absorber, i.e., of the hybrid perovskite layer, is expected to ave the highest impact on the charge generation rate. In a future study, optical and electronic charge transport modeling will be combined to investigate the effects of ETL, hybrid perovskite layer, and HTL thicknesses on the device performance. The findings of this study will be used to design photovoltaic devices based on hybrid perovskite planar heterojunctions with the maximum device power conversion efficiency.

BIBLIOGRAPHY

[1] Hines, M. A.; Guyot-Sionnest, P. Synthesis and Characterization of Strongly Luminescing ZnS-Capped CdSe Nanocrystals. *J. Phys. Chem.* **1996**, *100*, 468–471.

[2] Dabbousi, B. O.; Rodriguez-Viejo, J.; Mikulec, F. V.; Heine, J. R.; Mattoussi, H.; Ober, R.; Jensen, K. F.; Bawendi, M. G. (CdSe)ZnS Core-Shell Quantum Dots: Synthesis and Characterization of a Size Series of Highly Luminescent Nanocrystallites. *J. Phys. Chem. B* **1997**, *101*, 9463–9675.

[3] Peng, X. G.; Schlamp, M. C.; Kadavanich, A. V.; Alivisatos, A. P. Epitaxial Growth of Highly Luminescent CdSe/CdS Core/Shell Nanocrystals with Photostability and Electronic Accessibility. *J. Am. Chem. Soc.* **1997**, *119*, 7019–7029.

[4] Kim, S.; Fisher, B.; Eisler, H. J.; Bawendi, M. Type-II Quantum Dots: CdTe/CdSe (Core/Shell) and CdSe/ZnTe (Core/Shell) Heterostructures. *J. Am. Chem. Soc.* **2003**, *125*, 11466–11467.

[5] Talapin, D. V.; Mekis, I.; Gotzinger, S.; Kornowski, A.; Benson, O.; Weller, H. CdSe/CdS/ZnS and CdSe/ZnSe/ZnS Core-Shell-Shell Nanocrystals. *J. Phys. Chem.* B **2004**, *108*, 18826–18831.

[6] Reiss, P. ZnSe Based Colloidal Nanocrystals: Synthesis, Shape Control, Core/Shell, Alloy and Doped Systems. *New J. Chem.* **2007**, *31*, 1843–1852.

[7] Reiss, P.; Protière, M.; Li, L. Core/Shell Semiconductor Nanocrystals. *Small* **2009**, *5*, 154–168.

[8] Smith, A. M.; Mohs, A. M.; Nie, S. Tuning the Optical and Electronic Properties of Colloidal Nanocrystals by Lattice Strain. *Nat. Nanotechnol.* **2009**, *4*, 1748–3387.

[9] Wang, X.; Ren, X.; Kahen, K.; Hahn, M. A.; Rajeswaran, M.; Maccagnano-Zacher, S.; Silcox, J.; Cragg, G. E.; Efros, A. L.; Krauss, T. D. Non-Blinking Semiconductor Nanocrystals. *Nature* **2009**, *459*, 686–689.

[10] Pandey, S. C.; Maroudas, D. Equilibrium Compositional Distribution in Freestanding Ternary Semiconductor Quantum Dots: The Case of $In_xGa_{1-x}As$. *J. Chem. Phys.* **2011**, *135*, 234701.

[11] Pandey, S. C.; Mountziaris, T. J.; Venkataraman, D.; Maroudas, D. Formation of Core/Shell-like $ZnSe_{1-x}Te_x$ Nanocrystals due to Equilibrium Surface Segregation. *Appl. Phys. Lett.* **2010**, *96*, 201910.

[12] Pandey, S. C.; Sfyris, G. I.; Maroudas, D. Theory of Surface Segregation in Ternary Semiconductor Quantum Dots. *Appl. Phys. Lett.* **2011**, *98*, 091907.

[13] Pandey, S. C.; Wang, J.; Mountziaris, T. J.; Maroudas, D. Thermodynamic Instability of ZnSe/ZnS Core/Shell Quantum Dots. *J. Appl. Phys.* **2012**, *111*, 113526.

[14] Krebs, F. C. All Solution Roll-to-Roll Processed Polymer Solar Cells Free from Indium-Tin-Oxide and Vacuum Coating Steps. *Org. Electron.* **2009**, *10*, 761–768.

[15] Krebs F. C.; Norrman, K. Using Light-Induced Thermocleavage in a Roll-to-Roll Process for Polymer Solar Cells. *ACS Appl. Mater. Interfaces* **2010**, *2*, 877–887.

[16] Liu, Y.; Chen, C.; Hong, Z.; Gao, J.; Yang, Y.; Zhou, H.; Dou, L.; Li, G.; Yang, Y. Solution-Processed Small-Molecule Solar Cells: Breaking the 10% Power Conversion Efficiency. *Sci. Rep.* **2013**, *3*, 3356.

[17] Nagarjuna G.; Venkataraman, D. Strategies for Controlling the Active Layer Morphologies in OPVs. *J. Poly. Sci. B* **2012**, *50*, 1045–1056.

[18] Venkataraman, D.; Yurt, S.; Venkatraman, B. H.; Gavvalapalli, N. Role of Molecular Architecture in Organic Photovoltaic Cells. *J. Phys. Chem. Lett.* **2010**, *1*, 947–958.

[19] Nicho, M. E.; García-Escobar, C. H.; Arenas, M. C.; Alruzar-Coello, P.; Cruz-Silva, R.; Güizado-Rodríguez, M. Influence of P3HT Concentration on Morphological, Optical and Electrical Properties of P3HT/PS and P3HT/PMMA Binary Blends. *Mater. Sci. Eng. B* **2011**, *176*, 1393–1400.

[20] Park, N. G. Perovskite Solar Cells: An Emerging Photovoltaic Technology. *Mater. Today* **2015**, *18*, 65–72.

[21] Kojima, A.; Teshima, K.; Shirai, Y.; Miyasaka, T. Organometal Halide Perovskites as Visible-Light Sensitizers for Photovoltaic Cells. *J. Am. Chem. Soc.* **2009**, *131*, 6050–6051.

[22] Green, M. A.; Ho-Baillie A.; Snaith, H. J. The Emergence of Perovskite Solar Cells. *Nat. Photon.* **2014**, *8*, 506–514.

[23] Im, J. H.; Lee, C. R.; Lee, J. W.; Park, S. W.; Park, N. G. 6.5% Efficient Perovskite Quantum-Dot-Sensitized Solar Cell. *Nanoscale* **2011**, *3*, 4088–4093.

[24] Luo, S.; Daoud, W. A. Recent Progress in Organic-Inorganic Halide Perovskite Solar Cells: Mechanisms and Material Design. *J. Mater. Chem. A* **2015**, *3* 8992–9010.

[25] Park, N. G. Organometal Perovskite Light Absorbers toward a 20% Efficiency Low-Cost Solid-State Mesoscopic Solar Cell. *J. Phys. Chem. Lett.* **2013**, *4*, 2423–2429.

[26] Sha, W. E. I.; Ren, X.; Chen, L.; Choy, W. C. H. The Efficiency Limit of $CH_3NH_3PbI_3$ Perovskite Solar Cells. *Appl. Phys. Lett.* **2015**, *106*, 221104.

[27] Lomascolo, M.; Creti, A.; Leo, G.; Vasanelli, L.; Manna, L. Exciton Relaxation Processes in Colloidal Core/Shell ZnSe/ZnS Nanocrystals. *Appl. Phys. Lett.* **2003**, *82*, 418.

[28] Pandey, S. C.; Mountziaris, T. J.; Maroudas, D. Compositional Effects on the Electronic Structure of $ZnSe_{1-x}S_x$ Ternary Quantum Dots. *Appl. Phys. Lett.* **2011**, *99*, 101902.

[29] Pandey, S. C.; Maroudas, D. Effects of Composition and Compositional Distribution on the Electronic Structure of $ZnSe_{1-x}Te_x$ Ternary Quantum Dots. *J. Appl. Phys.* **2011**, *110*, 123509.

[30] Deen, W. M. *Analysis of Transport Phenomena*, 1st ed. Oxford: Oxford University Press, **1998**.

[31] Cottrell, A. H.; Jaswon M. A. Distribution of Solute Atoms Round a Slow Dislocation. *Proc. R. Soc. Lond Series A.* **1949**, *199*, 104–114.

[32] Bacon, D. J. Mechanical Interaction of a Point Defect with a Surface Layer. *Phys. Stat. Sol. B*. **1972**, *50*, 607–617.

[33] Michel, B. Influence of Solid Surfaces on the Interaction Energy of Point Defects. *Phys. Stat. Sol. B.* **1977**, *81*, 87–90.

[34] Maradudin, A. A; Wallis R. F. Elastic Interactions of Point Defects in a Semi-Infinite Medium. *Surf. Sci.* **1980**, *91*, 423–439.

[35] Fang, Z.; Li, Y.; Zhang, H.; Zhong, X.; Zhu, L. Facile Synthesis of Highly Luminescent UV-Blue-Emitting ZnSe/ZnS Core/Shell Nanocrystals in Aqueous Media. *J. Phys. Chem. C* **2009**, *113*, 14145–14150.

[36] Finlayson, B. A. *Nonlinear Analysis in Chemical Engineering,* McGraw-Hill, New York, **1980**.

[37] Gilbert, B.; Huang, F.; Zhang, H.; Waychunas, G. A.; Banfield, J. F. Nanoparticles: Strained and Stiff. *Science* **2004**, *305*, 651–654.

[38] Asami, S.; Ebina, A.; Takahashi, T. Growth of ZnS_xSe_{1-x} Layers on ZnS and ZnSe Substrates by a Solid-State-Diffusion Technique. *Jpn. J. Appl. Phys. 1* **1978**, *17*, 779–785.

[39] Dutt, M. B.; Sharma, B. L. *3 Diffusion in Compound Semiconductors*, Beke, D. L. Ed. SpringerMaterials-The Landolt-Bornstein Database, **1998**.

[40] Strassburg, M.; Kuttler, M.; Pohl, U. W.; Bimberg, D. Diffusion of Cd, Mg, and S in ZnSe-based Quantum Well Structures. *Thin Solid Films* **1998**, *336*, 208–212.

[41] Meijer, E. J.; de Leeuw, D. M.; Setayesh, S.; van Veenendaal, E.; Huisman, B. H.; Blom, P. W. M.; Hummelen, J. C.; Scherf, U.; Klapwijk, T. M. Solution-Processed Ambipolar Organic Field-Effect Transistors and Inverters. *Nat. Mater.* **2003**, *2*, 678–682.

[42] Burroughes, J. H.; Bradley, D. D. C.; Brown, A. R.; Marks, R. N.; Mackay, K.; Friend, R. H.; Burns, P. L.; Holmes, A. B. Light-Emitting Diodes Based on Conjugated Polymers. *Nature* **1990**, *347*, 539–541.

[43] Cheng, Y. J.; Yang, S. H.; Hsu, C. S. Synthesis of Conjugated Polymers for Organic Solar Cell Applications. *Chem. Rev.* **2009**, *109*, 5868–5923.

[44] Gunes, S.; Neugebauer, H.; Sariciftci, N. S. Conjugated Polymer-Based Organic Solar Cells. *Chem. Rev*. **2007**, *107*, 1324–1338.

[45] Brabec, C. J. Organic Photovoltaics: Technology and Market. *Sol. Energy Mater. Solar Cells* **2004**, *83*, 273–292.

[46] Shaheen, S. E.; Radspinner, R.; Peyghambarian, N.; Jabbour, G. E. Fabrication of Bulk Heterojunction Plastic Solar Cells by Screen Printing. *Appl. Phys. Lett.* **2001**, *79*, 2996–2998.

[47] Brabec, C. J.; Durrant, J. R. Solution-Processed Organic Solar Cells. *MRS Bull.* **2008**, *33*, 670–675.

[48] Li, K.; Li, Z.; Feng, K.; Xu, X.; Wang, L.; Peng, Q. Development of Large Band-Gap Conjugated Copolymers for Efficient Regular Single and Tandem Organic Solar Cells. *J. Am. Chem. Soc.* **2013**, *135*, 13549–13557.

[49] Scharber, M. C.; Muhlbacher, D.; Koppe, M.; Denk, P.; Waldauf, C.; Heeger, A. J.; Brabec, C. J. Design Rules for Donors in Bulk-Heterojunction Solar Cells-Towards 10% Energy-Conversion Efficiency. *Adv. Mater.* **2006**, *18*, 789–794.

[50] You, J.; Dou, L.; Yoshimura, K.; Kato, T.; Ohya, K.; Moriarty, T.; Emery, K.; Chen, C. C.; Gao, J.; Li, G. et al. A Polymer Tandem Solar Cell with 10.6% Power Conversion Efficiency. *Nat. Commun.* **2013**, *4*, 1446.

[51] Seo, J. H.; Kim, D. H.; Kwon, S. H.; Song, M.; Choi, M. S.; Ryu, S. Y.; Lee, H. W.; Park, Y. C.; Kwon, J. D.; Nam, K. S. et al. High Efficiency Inorganic/Organic Hybrid Tandem Solar Cells. *Adv. Mater.* **2012**, *24*, 4523–4527.

[52] Gunes, S.; Sariciftci, N. S. Hybrid Solar Cells. *Inorg. Chim. Acta* **2008**, *361*, 581–588.

[53] Knecht, U.; Woitowitz, H. J. Human Toxicokinetics of Inhaled Monochlorobenzene: Latest Experimental Findings Regarding Re-evaluation of the Biological Tolerance Value. *Int. Arch. Occup. Environ. Health* **2000**, *73*, 543–554.

[54] Ruder, A. M. Potential Health Effects of Occupational Chlorinated Solvent Exposure. *Ann. N. Y. Acad. Sci.* **2006**, *1076*, 207–227.

[55] Kerger, B. D.; Roberts, S. M.; James, R. C. Comparison of Human and Mouse Liver Microsomal Metabolism of Bromobenzene and Chlorobenzene to 2- and 4-halophenols. *Drug Metab. Dispos.* **1988**, *16*, 672–677.

[56] Stapleton, A.; Vaughan, B.; Xue, B.; Sesa, E.; Burke, K.; Zhou, X.; Bryant, G.; Werzer, O.; Nelson, A.; Kilcoyne, A. L. D. et al. A Multilayered Approach to Polyfluorene Water-Based Organic Photovoltaics. *Sol. Energy Mater. Sol. Cells* **2012**, *102*, 114–124.

[57] Kietzke, T.; Neher, D.; Landfester, K.; Montenegro, R.; Guntner, R.; Scherf, U. Novel Approaches to Polymer Blends Based on Polymer Nanoparticles. *Nat. Mater.* **2003**, *2*, 408–412.

[58] Zhou, X.; Belcher, W; Dastoor, P. Solar Paint: From Synthesis to Printing. *Polymers* **2014**, *6*, 2832–2844.

[59] Yamamoto, N. A. D.; Payne, M. E.; Koehler, M; Facchetti, A.; Roman, L. S.; Arias, A. C. Charge Transport Model for Photovoltaic Devices Based on Printed Polymer: Fullerene Nanoparticles. *Sol. Energy Mater. Sol. Cells* **2015,** *141*, 171–177.

[60] Dam, H. F.; Holmes, N. P.; Andersen, T. R.; Larsen-Olsen, T. T.; Barr, M.; Kilcoyne, A. L. D.; Zhou, X.; Dastoor, P. C.; Krebs, F. C.; Belcher, W. J. The Effect of Mesomorphology upon the Performance of Nanoparticulate Organic Photovoltaic Devices. *Sol. Energy Mater. Sol. Cells* **2015,** *138*, 102–108.

[61] Gehan, T. S.; Bag, M.; Renna, L. A.; Shen, X.; Algaier, D. D.; Lahti, P. M.; Russell, T. P.; Venkataraman, D. Multiscale Active Layer Morphologies for Organic Photovoltaics Through Self-Assembly of Nanospheres. *Nano Letters* **2014**, *14*, 5238–5243.

[62] Bag, M.; Gehan, T. S.; Algaier, D. D.; Liu, F.; Nagarjuna, G.; Lahti, P. M.; Russell, T. P.; Venkataraman, D. Efficient Charge Transport in Assemblies of Surfactant-Stabilized Semiconducting Nanoparticles. *Adv. Mater.* **2013**, *25*, 6411–6415.

[63] Kietzke, T.; Neher, D.; Kumke, M.; Montenegro, R.; Landfester, K.; Scherf, U. A Nanoparticle Approach to Control the Phase Separation in Polyfluorene Photovoltaic Devices. *Macromolecules* **2004**, *37*, 4882–4890.

[64] Gartner, S.; Christmann, M.; Sankaran, S.; Rohm, H.; Prinz, E. M.; Penth, F.; Putz, A.; Tureli, A. E.; Penth, B.; Baumstummler, B. et al. Eco-Friendly Fabrication of 4% Efficient Organic Solar Cells from Surfactant-Free P3HT:ICBA Nanoparticle Dispersions. *Adv. Mater.* **2014**, *26*, 6653–6657.

[65] Bag, M.; Gehan, T. S.; Renna, L. A.; Algaier, D. D.; Lahti, P. M.; Venkataraman, D. Fabrication Conditions for Efficient Organic Photovoltaic Cells from Aqueous Dispersions of Nanoparticles. *RSC Adv.* **2014**, *4*, 45325–45331.

[66] Kanai, Y.; Grossman, J. C. Role of Semiconducting and Metallic Tubes in P3HT/Carbon-Nanotube Photovoltaic Heterojunctions: Density Functional Theory Calculations. *Nano Letters* **2008**, *8*, 908–912.

[67] Marchiori, C.; Koehler, M. Dipole Assisted Exciton Dissociation at Conjugated Polymer/Fullerene Photovoltaic Interfaces: A Molecular Study Using Density Functional Theory Calculations. *Synth. Met.* **2010**, *160*, 643–650.

[68] Flores, F.; Ortega, J.; Vazquez, H. Modelling Energy Level Alignment at Organic Interfaces and Density Functional Theory. *Phys. Chem. Chem. Phys.* **2009**, *11*, 8658–8675.

[69] Huang, D. M.; Faller, R.; Do, K.; Moule, A. J. Coarse-Grained Computer Simulations of Polymer/Fullerene Bulk Heterojunctions for Organic Photovoltaic Applications. *J. Chem. Theory Comput.* **2010**, *6*, 526–537.

[70] Watkins, P. K.; Walker, A. B.; Verschoor, G. L. B. Dynamical Monte Carlo Modelling of Organic Solar Cells: The Dependence of Internal Quantum Efficiency on Morphology. *Nano Letters* **2005**, *5*, 1814–1818.

[71] Peumans, P.; Uchida, S.; Forrest, S. R. Efficient Bulk Heterojunction Photovoltaic Cells Using Small-Molecular-Weight Organic Thin Films. *Nature* **2003**, *425*, 158–162.

[72] Lyons, B. P.; Clarke, N; Groves, C. The Relative Importance of Domain Size, Domain Purity and Domain Interfaces to the Performance of Bulk-Heterojunction Organic Photovoltaics. *Energy Environ. Sci.* **2012**, *5*, 7657–7663.

[73] He, D.; Ekere, N. N. Effect of Particle Size Ratio on the Conducting Percolation Threshold of Granular Conductive-Insulating Composites. *J. Phys. D: Appl. Phys.* **2004**, *37*, 1848–1852.

[74] Koster, L. J. A.; Smits, E. C. P.; Mihailetchi, V. D.; Blom, P. W. M. Device Model for the Operation of Polymer/Fullerene Bulk Heterojunction Solar Cells. *Phys. Rev. B* **2005**, *72*, 085205.

[75] Barker, J. A.; Ramsdale, C. M.; Greenham, N. C. Modeling the Current-Voltage Characteristics of Bilayer Polymer Photovoltaic Devices. *Phys. Rev. B* **2003**, *67*, 075205.

[76] Han, X.; Bag, M.; Gehan, T. S.; Venkataraman, D; Maroudas, D. Analysis of Hole Transport in Thin Films and Nanoparticle Assemblies of Poly(3-hexylthiophene). *Chem. Phys. Lett.* **2014**, *610-611*, 273–277.

[77] Fong, H. H.; Papadimitratos, A.; Malliaras, G. G. Non-Dispersive Hole Transport in a Polyflyorene Copolymer with a Mobility of 0.01 $cm^2V^{-1}s^{-1}$. *Appl. Phys. Lett.* **2006**, *89*, 172116.

[78] Scott, J. C.; Malliaras, G. G. Charge Injection and Recombination at the Metal-Organic Interface. *Chem. Phys. Lett.* **1999**, *299*, 115–119.

[79] Seki, H. A Study of the Initial Photocurrent Due to Pulsed Light Absorbed in Finite Thickness. *J. Appl. Phys.* **1972**, *43*, 1144–1150.

[80] Hwang, I.; McNeill, C. R.; Greenham, N. C. Drift-Diffusion Modeling of Photocurrent Transients in Bulk Heterojunction Solar Cells. *J. Appl. Phys.* **2009**, *106*, 094506.

[81] van der Holst, J. J. M. *Three-Dimensional Modeling of Charge Transport, Injection and Recombination in Organic Light-Emitting Diodes*, Eindhoven University of Technology, **2010**.

[82] Hausermann, R; Knapp, E.; Moos, M.; Reinke, N. A.; Flatz, T.; Ruhstaller, B. Coupled Optoelectronic Simulation of Organic Bulk-Heterojunction Solar Cells: Parameter Extraction and Sensitivity Analysis. *J. Appl. Phys.* **2009**, *106*, 104507.

[83] Arkhipov, V. I.; Heremans, P.; Emelianova, E. V.; Adriaenssens, G. J. Space-Charge-Limited Currents in Materials with Gaussian Energy Distributions of Localized States. *Appl. Phys. Lett.* **2001**, *79*, 4154–4156.

[84] Arkhipov, V. I.; Vannikov, A. V.; Mingaleev, G. S.; Popova, Y. A.; Rudenko, A. I.; Saenko, V. S.; Tyutnev, A. P. Transient Photocurrent due to Step-Function Excitation in Disordered Materials-Computer Simulation and Analytical Treatment. *J. Phys. D: Appl. Phys.* **1984**, *17*, 1469–1475.

[85] Grancini, G.; Maiuri, M.; Fazzi, D.; Petrozza, A.; Egelhaaf, H.-J.; Brida, D.; Cerullo, G.; Lanzani, G. Hot Exciton Dissociation in Polymer Solar Cells. *Nat. Mater.* **2013**, *12*, 29–33.

[86] Lee, J; Vandewal, K.; Yost, S. R.; Bahlke, M. E.; Goris, L.; Baldo, M. A.; Manca, J. V.; Voorhis, T. V. Charge Transfer State Versus Hot Exciton Dissociation in Polymer−Fullerene Blended Solar Cells. *J. Am. Chem. Soc.* **2010**, *132*, 11878–11880.

[87] Grancini, G.; Polli, D.; Fazzi, D.; Cabanillas-Gonzalez, J.; Cerullo, G.;Lanzani, G. Transient Absorption Imaging of P3HT:PCBM Photovoltaic Blend: Evidence For Interfacial Charge Transfer State. *J. Phys. Chem. Lett.* **2011**, *2*, 1099–1105.

[88] McMahon, D. P.; Cheung, D. L.; Troisi, A. Why Holes and Electrons Separate So Well in Polymer/Fullerene Photovoltaic Cells. *J. Phys. Chem. Lett.* **2011**, *2*, 2737–2741.

[89] Howard, I. A.; Mauer, R.; Meister, M.; Laquai, F. Effect of Morphology on Ultrafast Free Carrier Generation in Polythiophene:Fullerene Organic Solar Cells. *J. Am. Chem. Soc.* **2010**, *132*, 14866–14876.

[90] Hwang, I. W.; Soci, C.; Moses, D.; Zhu, Z.; Waller, D.; Gaudiana, R.; Brabec, C.; Heeger, A. Ultrafast Electron Transfer and Decay Dynamics in a Small Band Gap Bulk Heterojunction Material. *Adv. Mater.* **2007**, *19*, 2307–2312.

[91] Gregg, B. A.; Hanna, M. C. Comparing Organic to Inorganic Photovoltaic Cells: Theory, Experiment, and Simulation *J. Appl. Phys.* **2003**, 93, 3605–3614.

[92] Langevin, P. Recombinaison et Mobilites des Ions Dans les Gaz. *Ann. Chim. Phys*. **1903**, *28*, 433–530.

[93] Lakhwani, G.; Rao, A.; Friend, R. H. Bimolecular Recombination in Organic Photovoltaics. *Annu. Rev. Phys. Chem.* **2014**, *65*, 557–581.

[94] Juska, G.; Arlauskas, K.; Stuchlik, J.; Osterbacka, R. Non-Langevin Bimolecular Recombination in Low-Mobility Materials. *J. Non-Cryst. Solids* **2006**, *352*, 1167–1171.

[95] Deibel, C.; Baumann, A.; Dyakonov, V. Polaron Recombination in Pristine and Annealed Bulk Heterojunction Solar Cells. *Appl. Phys. Lett.* **2008**, *93*, 163303.

[96] Onsager, L. Initial Recombination of Ions. *Phys. Rev*. **1938**, *54*, 554–557.

[97] Onsager, L. Deviations from Ohm's Law in Weak Electrolytes. *J. Chem. Phys.* **1934**, *2*, 599–615.

[98] Braun, C. L. Electric Feld Assisted Dissociation of Charge Transfer States as a Mechanism of Photocarrier Production. *J. Chem. Phys.* **1984**, *80*, 4157–4161.

[99] Scher, H. Anomalous Transit-Time Dispersion in Amorphous Solids. *Phys. Rev. B* **1975**, *12* 2455–2477.

[100] Staudigel, J.; Stossel, M.; Steuber, F.; Simmerer, J. A Quantitative Numerical Model of Multilayer Vapor-Deposited Organic Light Emitting Diodes. *J. Appl. Phys.* **1999**, *86*, 3895–3910.

[101] Guo, J.; Ohkita, H.; Benten, H.; Ito, S. Near-IR Femtosecond Transient Absorption Spectroscopy of Ultrafast Polaron and Triplet Exciton Formation in Polythiophene Films with Different Regioregularities *J. Am. Chem. Soc.* **2009**, *131*, 16869–80.

[102] Pasveer, W. F.; Cottaar, J.; Tanase, C.; Coehoorn, R.; Bobbert, P. A.; Blom, P. W. M.; de Leeuw, D. M.; Michels, M. A. Unified Description of Charge-Carrier Mobilities in Disordered Semiconducting Polymers. *J. Phys. Rev. Lett.* **2005**, *94*, 206601.

[103] Mozer, A. J.; Sariciftci, N. S. Negative Electric Feld Dependence of Charge Carrier Drift Mobility in Conjugated, Semiconducting Polymers. *Chem. Phys. Lett.* **2004**, *389*, 438–442.

[104] Gill, W. D. Drift Mobilities in Amorphous Charge-Transfer Complexes of Trinitrofluorenone and Poly-n-vinylcarbazole. *J. Appl. Phys.* **1972**, *43*, 5033–5040.

[105] Kim, J. Y.; Kotov, N. A. Charge Transport Dilemma of Solution-Processed Nanomaterials. *Chem. Mater.* **2014**, *26*, 134–152.

[106] Bässler, H. Charge Transport in Disordered Organic Photoconductors a Monte Carlo Simulation Study. *Phys. Stat. Sol. B* **1993**, 175, 15–56.

[107] Nagata, T.; Oh, S.; Chikyow, T.; Wakayama, Y. Effect of UV-Ozone Treatment on Electrical Properties of PEDOT:PSS Film. *Org. Electron.* **2011**, *12*, 279–284.

[108] Helander, M. G.; Wang, Z. B.; Greiner, M. T.; Liu, Z. W.; Lian, K.; Lu, Z. H. The Effect of UV Ozone Treatment on Poly(3,4-ethylenedioxythiophene):Poly(styrenesulfonate). *Appl. Phys. Lett.* **2009**, *95*, 173302.

[109] Chen, L. M.; Xu, Z.; Hong, Z.; Yang, Y. Interface Investigation and Engineering - Achieving High Performance Polymer Photovoltaic Devices. *J. Mater. Chem.* **2010,** *20*, 2575–2598.

[110] Wojcik, M.; Michalak, P.; Tachiya, M. Effects of Energetic Disorder and Mobility Anisotropy on Geminate Electron-Hole Recombination in the Presence of a Donor-Acceptor Heterojunction. *Bull. Korean Chem. Soc.* **2012**, *33*, 795–802.

[111] Wojcik, M.; Tachiya, M. Accuracies of the Empirical Theories of the Escape Probability Based on Eigen Model and Braun Model Compared with the Exact Extension of Onsager Theory. *J. Chem. Phys.* **2009**, *130*, 104107.

[112] Pettersson, L. A. A.; Roman, L. S.; Inganas, O. Modeling Photocurrent Action Spectra of Photovoltaic Devices Based on Organic Thin Films. *J. Appl. Phys.* **1999**, *86*, 487–496.

[113] Nam, Y. M.; Huh, J.; Jo, W. H. Optimization of Thickness and Morphology of Active Layer for High Performance of Bulk-Heterojunction Organic Solar Cells. *Sol. Energy Mater. Sol. Cells* **2010**, *94*, 1118–1124.

[114] Burkhard, G. F.; Hoke, E. T.; McGehee, M. D. Accounting for Interference, Scattering, and Electrode Absorption to Make Accurate Internal Quantum Efficiency Measurements in Organic and Other Thin Solar Cells. *Adv. Mater.* **2010**, *22*, 3293–3297.

[115] Feron, K.; Fell, C. J.; Rozanski, L. J.; Gong, B. B.; Nicolaidis, N.; Belcher, W. J.; Zhou, X.; Sesa, E.; King, B. V.; Dastoor, P. C. Towards the Development of a Virtual Organic Solar Cell: An Experimental and Dynamic Monte Carlo Study of the Role of Charge Blocking Layers and Active Layer Thickness. *Appl. Phys. Lett.* **2012**, *101*, 193306.

[116] Street, R. A.; Schoendorf, M.; Roy, A.; Lee, J. H. Interface State Recombination in Organic Solar Cells. *Phys. Rev. B.: Condens. Matter Mater. Phys.* **2010**, *81*, 205307.

[117] Wehrenfennig, C.; Eperon, G. E.; Johnston, M. B.; Snaith, H. J.; Herz, L. M. High Charge Carrier Mobilities and Lifetimes in Organolead Trihalide Perovskites. *Adv. Matter*. **2014**, *26*, 1584–1589.

[118] Stranks, S. D.; Eperon, G. E.; Grancini, G.; Menelaou, C.; Alcocer, M. J. P.; Leijtens, T.; Herz, L. M.; Petrozza, A.; Snaith, H. J. Electron-Hole Diffusion Lengths Exceeding 1 Micrometer in an Organometal Trihalide Perovskite Absorber. *Science* **2013,** *342*, 341–344.

[119] Stoumpos, C. C.; Malliakas, C. D.; Kanatzidis, M. G. Semiconducting Tin and Lead Iodide Perovskites with Organic Cations: Phase Transitions, High Mobilities, and Near-Infrared Photoluminescent Properties. *Inorg. Chem.* **2013**, *52*, 9019–9038.

[120] Wang, Y.; Zhang, Y.; Zhang, P.; Zhang, W. High Intrinsic Carrier Mobility and Photon Absorption in the Perovskite $CH_3NH_3PbI_3$. *Phys. Chem. Chem. Phys.* **2015**, *17*, 11516–11520.

[121] You, J.; Hong, Z.; Yang, Y.; Chen, Q.; Cai, M.; Song, T. B.; Chen, C. C.; Lu, S.; Liu, Y.; Zhou, H.; Yang Y. Low-Temperature Solution-Processed Perovskite Solar Cells with High Efficiency and Flexibility. *ACS Nano* **2014**, *8*, 1674–1680.

[122] Lee, M. M.; Teuscher, J.; Miyasaka, T.; Murakami, T. N; Snaith, H. J. Efficient Hybrid Solar Cells Based on Meso-Superstructured Organometal Halide Perovskites. *Science* **2012**, *338*, 643–647.

[123] Laban W. A.; Etgar, L. Depleted Hole Conductor-Free Lead Halide Iodide Heterojunction Solar Cells. *Energy Environ. Sci*., **2013**, *6*, 3249–3253.

[124] Aharon, S.; Gamliel, S.; Cohen B. E.; Etgar, L. Depletion Region Effect of Highly Efficient Hole Conductor Free $CH_3NH_3PbI_3$ Perovskite Solar Cells. *Phys. Chem. Chem. Phys.*, **2014**, *16*, 10512–10518.

[125] Yang, W.; Yao, Y.; Wu, C. Q. Origin of the High Open Circuit Voltage in Planar Heterojunction Perovskite Solar Cells: Role of the Reduced Bimolecular Recombination. *J. Appl. Phys.* **2015**, *117*, 095502.

[126] Minemoto T.; Murata. M. Theoretical Analysis on Effect of Band Offsets in Perovskite Solar Cells. *Sol. Energy Mater. Sol. Cells* **2015**, *133*, 8–14.

[127] Minemoto, T.; Murata, M. Device Modeling of Perovskite Solar Cells Based on Structural Similarity with Thin Film Inorganic Semiconductor Solar Cells. *J. Appl. Phys.* **2014**, *116*, 054505.

[128] Bag, M; Renna, L. A.; Jeong, S. P.; Han, X; Maroudas, D; and Venkataraman, D. Facile Fabrication of Carbon Nanotube/Perovskite Composite Nanomaterials for Reduced Charge Recombination in Photovoltaic Devices. Submitted to *J. Phys. Chem. Lett.* **2015**.

[129] Lin, Q.; Armin, A.; Nagiri, R. C. R.; Burn, P. L.; Meredith, P. Electro-Optics of Perovskite Solar Cells. *Nat. Photon.* **2015**, *9*, 106–112.

[130] Hirasawa, M; Ishihara, T.; Goto, T.; Uchida, K.; Miura, N. Magnetoabsorption of the Lowest Exciton in Perovskite-Type Compound $(CH_3NH_3)PbI_3$. *Physica B: Condens. Matter* **1994**, *201*, 427–430.

[131] Savenije, T. J.; Ponseca, C. S.; Jr. Kunneman, L.; Abdellah, M.; Zheng, K.; Tian, Y.; Zhu, Q.; Canton. S. E.; Scheblykin, I. G.; Pullerits, T.; Yartsev, A.; Sundstrom, V. Thermally Activated Exciton Dissociation and Recombination Control the Carrier Dynamics in Organometal Halide Perovskite. *J. Phys. Chem. Lett.*, **2014**, *5*, 2189–2194.

[132] Oga, H.; Saeki, A.; Ogomi, Y.; Hayase, S.; Seki, S. Improved Understanding of the Electronic and Energetic Landscapes of Perovskite Solar Cells: High Local Charge Carrier Mobility, Reduced Recombination, and Extremely Shallow Traps. *J. Am. Chem. Soc.*, **2014**, *136*, 13818–13825.

[133] Foster, J. M.; Snaith, H. J.; Leijtens, T.; Richardson, G. A Model for the Operation of Perovskite Based Hybrid Solar Cells: Formulation, Analysis, and Comparison to Experiment. *SIAM J. Appl. Math.* **2014**, *74*, 1935–1966.

[134] Driscoll, T. A.; Hale, N.; Trefethen, L. N. editors, *Chebfun Guide*, Pafnuty Publications, Oxford, **2014**.

[135] Sokel R.; Hughes, R. C. Numerical Analysis of Transient Photoconductivity in Insulators. *J. Appl. Phys*. **1982**, *53*, 7414–7424.

[136] Li, Z.; Kulkarni, S. A.; Boix, P. P.; Shi, E.; Cao, A.; Fu, K.; Batabyal, S. K.; Zhang, J.; Xiong, Q.; Wong, L. H.; Mathews, N.; Mhaisalkar, S. G. Laminated Carbon Nanotube Networks for Metal Electrode-Free Efficient Perovskite Solar Cells. *ACS Nano*, **2014**, *8*, 6797–6804.

[137] Sze S. M.; Kwok K. Ng, *Physics of Semiconductor Devices*, 3rd Ed., Wiley-Interscience, New York, **2006**.

[138] Ponseca, C. S.; Savenije, T. J.; Abdellah, M.; Zheng, K.; Yartsev, A.; Pascher, T.; Harlang, T.;. Chabera, P; Pullerits, T.; Stepanov, A.; Wolf, J. P.; Sundstrom, V. Organometal Halide Perovskite Solar Cell Materials Rationalized: Ultrafast Charge Generation, High and Microsecond-Long Balanced Mobilities, and Slow Recombination. *J. Am. Chem. Soc.* **2014**, *136*, 5189–5192.

[139] N. J. Jeon, H. G. Lee, Y. C. Kim, J. Seo, J. H. Noh, J. Lee and S. I. Seok, *o*-Methoxy Substituents in Spiro-OMeTAD for Efficient Inorganic–Organic Hybrid Perovskite Solar Cells. *J. Am. Chem. Soc.*, **2014**, *136*, 7837–7840.